Faculty of Mathematics and Physics
Charles University, Prague

Detection of high-energy muons in cosmic ray showers

Petr Trávníček

Doctoral thesis

Prague, July 2004

Prohlašuji, že jsem disertační práci vypracoval samostatně s použitím uvedené literatury. Souhlasím se zapůjčováním práce.

V Praze, 12. 7. 2004 Petr Trávníček

Detection of high-energy muons in cosmic ray showers

Petr Trávníček

Institute of Physics,
Academy of Sciences of the Czech Republic

supervisor: Jan Řídký, CSc. - FZÚ AV ČR

Abstract

The DELPHI detector located at LEP accelerator has been used to measure multi-muon bundles originated from cosmic ray interactions. Two subdetectors - Hadron Calorimeter and Time Projection Chamber, are used for this purpose. The 1999 and 2000 data are analyzed over wide range of muon multiplicities. The muon multiplicity distribution is compared with prediction of Monte-Carlo simulation based on CORSIKA/QGSJET. The Monte-Carlo does not describe the large multiplicity part of data. Even the extreme assumption on the cosmic ray composition (pure iron nuclei) hardly predicts number of high multiplicity events comparable with the data. The impact of QGSJET internal parameters onto the result is also studied.

Acknowledgements

First of all I would like to thank Jan Řídký, supervisor of this thesis, for countless discussions, enormous help during my doctoral studies and continuous support. Without him this work would be completely impossible. It was Jan Řídký who initiated this analysis in the DELPHI collaboration. With his Prague colleagues Václav Vrba and Jiří Chudoba he wrote computer code used in the thesis to reconstruct cosmic ray events.

I would like to thank Ralph Engel and Jörg Hörandel for discussions and suggestions concerning my work. I thank Jörg Hörandel for sending me the model of hadron-hadron interactions with changed internal parameters.

I am very grateful to Jiří Mašík for all his help with technical problems concerning computers, storage disks, etc. Although he was busy with his own physics analysis, he was ready to help me almost anytime.

This thesis would have never happened without the impressive work of the DELPHI collaboration. I would like especially thank Pablo Tortosa, Giovanni Valenti, Konstantin Belous and Philippe Charpentier for their support, discussions and their work related to the DELPHI cosmic events.

I would like to thank Dalibor Nosek for his comments on the manuscript and interesting discussions.

My thanks go to Martina Boháčová for suggestions concerning historical part of the thesis and Michael Prouza for his help with astronomical problems related to the work. It was pleasure to discuss with my colleague Radomír Šmída.

I have received excellent support from the Center for Particle Physics - a joint project of the Institute of Physics, Academy of Sciences and the Faculty of Mathematics and Physics, Charles University.

This work was supported by the Ministry of Education of the Czech Republic within the projects LN00A006 and LA134.

I thank my family and my friends.

Contents

1 Introduction

The presented thesis describes the analysis of cosmic multi-muon bundles detected by DELPHI[1] experiment at CERN. This detector situated at LEP[2] collider 100 m underground allowed simultaneous detection of the e^+e^- interactions and the measurements of cosmic ray muons penetrating deep under the Earth surface.

In the years 1996 − 1997 DELHI hadron calorimeter (HCAL) was upgraded. The installation of cathode readout improved granularity of this device to such extent that it acquired properties of a simple tracking detector with large volume. Interesting events with many almost parallel tracks were immediately observed. It was clear that they consisted of muons produced in cosmic ray showers.

In the year 1998 cosmic ray trigger was tested to improve quality of observed events. Running in parasitic mode to usual e^+e^- data taking we collected during the years 1999 and 2000 cosmic ray events equivalent to 1.6 10^6 s of live time. Even though the detector capabilities are limited and the amount of data is just a fraction of what is collected at dedicated cosmic ray experiments, some conclusions can be drawn about the models used to describe interactions of particles in the cosmic ray shower.

Signals from cathode readout of hadron calorimeter and partly data from time projection chamber (TPC) are used to reconstruct these events. Muon multiplicity distributions are estimated. The aim of the work is to compare the measured distributions with the predictions of Monte Carlo simulations of cosmic ray showers.

Simulations with CORSIKA program [1] (model used to describe the evolution of cosmic ray showers in the atmosphere) are performed. QGSJET model [2] is used to simulate high energy interactions of hadrons during the shower development. Passage of muons through the rock above DELPHI as well as detector response are simulated in details. The impact of modification of QGSJET parameters on the multiplicity distributions is also checked.

It was found that the simulations hardly predict comparable number of medium and high multiplicity events with respect to the data, even if only the very heavy (iron) cosmic primaries are assumed. It is likely that the problems originate in the interaction model which underestimates production of muons. The results with modified parameters of QGSJET somewhat improves consistency of the simulation with the data.

Results of this thesis were reported at several conferences and published

[1]DEtector with Lepton Photon and Hadron Identification
[2]Large Electron Positron collider

in conference proceedings, e.g.: "Very High Energy Cosmic Ray Interactions", Geneva 2002, [3] (preliminary report), "International Conference of High Energy Physics", Amsterdam 2002 [4] (joint presentation of DELPHI and L3+C) and "Epiphany Conference on Astroparticle Physics", Krakow 2004, [5].

- **Chapter 2 - Cosmic rays**
  This chapter provides introduction into the field of astroparticle and cosmic ray physics. After some historical remarks, the energy spectra and cosmic ray composition are presented. Basic facts about physics of atmospheric showers and various experimental techniques of their detection are reviewed. The importance of computer simulations of particle processes during the shower development is discussed.

- **Chapter 3 - Detection of cosmic muon bundles at DELPHI**
  It gives some basic information about the detector design. Sub-detectors used to detect comic rays are described in more details. The trigger as well as reconstruction of the multi-muon bundles are outlined.

- **Chapter 4 - Delphi data**
  In this chapter, it is explained how we select the data samples. It shows the measured multiplicity spectra from HCAL and TPC. The distribution of sidereal time for detected events is studied in order to check possible signatures of point sources. The sky plot of selected events is presented.

- **Chapter 5 - Simulation.**
  This chapter describes the chain of simulation programs used in the analysis: CORSIKA $\rightarrow$ rock simulation $\rightarrow$ detector response. Various aspects of the analysis are discussed: choice of the simulation area, stability of reconstruction, etc. Finally the predicted multiplicity distributions are shown with two different types of primary cosmic particles (proton and iron nuclei). The distributions are given separately in different contributing intervals of the primary energy.

- **Chapter 6 - Results**
  The simulated distributions are compared to the data. The aspect of hadron-hadron interaction models is further studied and the model with modified interaction parameters is tested. The results are given also in case of this modification. Sources of various errors are described and their impact on the final result is investigated. Finally the consistency of the simulations with the data is discussed and the conclusions are drawn.

- **Chapter 7 - Conclusions**
  It provides brief recapitulation of the studied problematics.

2 Cosmic Rays

2.1 Brief history of cosmic rays and particle physics

History of cosmic rays was preceded by discovery in the field of particle and nuclear physics. It starts with the finding of “cathode” rays by W. Crookes in 1879. It was lately shown by J. J. Thompson that they consist of particles with the mass/charge ratio much less than that of the hydrogen atom. Measuring the charge of cathode rays it was established, that the mass of the first elementary particle has to be about 1/1000 of the mass of the hydrogen atom. The history continued in 1895 by Röntgen’s discovery of X-rays emitted from the Crookes tube. About ten years later C. G. Barkla found the evidence of X-rays polarization, consequently it was possible to associate X-rays with the electromagnetic radiation. In 1896 H. Becquerel discovered the natural radioactivity by observing that his photographic plates darken when exposed to uranium. Systematic works of E. Rutherford established that there are at least two components of radiation, α and β that differ by their penetrative power. It was quickly shown that the β radiation consists of Crookes electrons, while the today picture of α radioactivity (the helium nuclei) was adjusted only ten years later. In 1900 P. Villard added γ rays to the list of known radiation types.

The existence of cosmic rays as the extraterrestrial radioactivity was first suggested by C.T.R. Wilson [6] in 1900. At that time it was observed that electroscopes discharge even when kept away from radioactive sources. E. Rutherford argued that the slow discharge can be still caused by the natural radiation from the rock or contamination of vessels. The idea of the extraterrestrial radiation was dropped for about ten following years.

In order to check the level of natural radiation T. Wulf measured the ionization power at the foot and at the top of the Eiffel Tower. It was expected that even the most penetrating radiation - γ rays would decrease to negligible level at the top of the Tower, 330 m above the Earth surface. To Wulf’s big surprise the ionization intensity at the top was reduced only by a factor of two when compared to measurements on the ground level. The idea of measuring the ionization intensity above the Earth surface continued with balloon experiments performed by A. Gockel during 1910 and 1911. He found that the radiation did not decrease with altitude, however his results were not fully conclusive due to various experimental problems.

The year 1912 is usually considered as the year of discovery of cosmic rays.

V.F. Hess [7] and later W. Kolhörster [8] performed dedicated balloon flights in order to explore the behavior of ionization power with the increasing altitude. The Kolhösters flights reached the impressive 9 km height. It was Hess, who observed for the first time the ionization increase[1] with increasing altitudes and quickly explained his results "**... by the assumption that a radiation of very high penetrating power enters the atmosphere from above, and still produces in the lower layers a part of the ionization observed ...**" (V. Hess 1912).

Thus the existence of extraterrestrial radiation was established. Later in 1925 R.A. Millikan introduced the term "cosmic rays", which is still used in our days. The cosmic rays were believed to consist of γ-radiation, however experimental results of Clay, Compton and Jonson [10], in 1930's showed that part of the cosmic rays could be deflected in the Earth magnetic field and thus they had to consist of charged particles, too.

Starting from 1929 when D. V. Skobelstyn recorded his first cloud chamber pictures, the cosmic rays studies became the excellent tool for exploring the world of elementary particles. Skobelstyn found, that some of the observed tracks hardly bent in a magnetic field, and misinterpreted them as the Compton electrons produced from ultra energetic gamma rays. With our current knowledge he was the first one who observed muons. Skobelstyn's works were followed by Anderson's major discovery of positron in 1930 [11]. The discovery helped to put the Dirac's theory of relativistic quantum mechanic on solid experimental basis. This theory interprets the negative energy solutions of Dirac equation as anti-particles. Thus it was concluded, that the observed positron is the anti-particle to the electron. Later the concept of electromagnetic cascades was developed, and the history moved towards the discovery of the Extensive Air Showers (EAS) by Schmeiser, Bothe, Kölhorster and Auger [12, 13, 14].

Anderson also observed the same effect as Skobelstyn, i.e. tracks that were bent in magnetic field much less than electrons. In 1939 Anderson and S. Nedermayer were able to estimate the mass of the particles and announce the discovery of "mesotron" with mass about 200 times the electron mass. In today's terms these particles are called muons - μ. However, at the time of mesotron discovery the experiment coincided with the Yukawa's theory of strong force. In this theory Yukawa estimated the mass of strong force mediators to be about 250 times of the electron mass, i.e. close to the value measured by Anderson. Consequently it was natural to interpret mesotrns as Yukawa particles. In fact, particles proposed by Yukawa are pions - $\pi^{\pm}$, π^0 and not muons, but the pion was discovered only in 1947.

[1] The ionization increase at high altitudes was observed for the first time in the balloon called "Bohemia" which started its fly in the Czech town Ústí nad Labem, [7, 9].

After the World War II, the history of particle physics foundation continued again with cosmic rays studies. G. Rochester and C. Butler observed in their cloud chamber so called "V" tracks and interpreted them as the decay of yet unknown particles. Later these "V" tracks became to be known as "strange" particles. They were produced in strong interactions, but because of their long life time, it was expected, that they decay via weak interaction, hence origin of the word "strange". Today the observed particles are known as $K^{\pm}$, K^0 and they have mass about half of mass of the proton. However, one particle observed at that time - Λ has mass larger than the mass of the proton.

History continued with the development of emulsion chambers by C.F. Powell. This new device improved the position resolution to unprecedented accuracy. The first experimental result of major importance obtained by emulsion chambers was the pion discovery. Next particles discovered in cosmic rays were Ξ^-, Σ^+ in 1952 and 1953, respectively. The year 1953 is the year, when the accelerator experiments started to play the most important role in the particle physics research. Accelerator beams, contrary to cosmic rays, have of course the important advantage of known initial conditions. However, cosmic rays continued to be of great interest especially in the field of the neutrino physics. Nowadays cosmic rays of ultra-high energies again enter the stage of the most important physical and cosmological issues as will be briefly discussed in the next section.

It should be said for completeness, that many more particles had been observed during 1950s and 1960s by the accelerator experiments. The nice and comprehensive review of major experimental discoveries at that time can be found in [15].

By introducing the quark model, the large number of observed hadrons was reduced to only 6 quarks grouped together with elementary leptons into 3 generations of fundamental particles, see Tab 2.1. All natural materials occurring at the Earth are composed from fundamental objects of the first generation. In fact, the c and b hadrons were observed during 1970s [16, 17, 18] and the t quark was discovered only in 1995 [20, 19]. The discovery of electron neutrinos by Reines and Cowan is dated to 1953 and in 1962 Lederman, Schwartz and Steinberger showed that there are actually two neutrino types: electron (ν_e) and muon neutrino (ν_μ). The τ lepton enters the scene in 1975 when it was discovered by M. Perl from MARK I collaboration [21]. The existence of the last neutrino specie (ν_τ) was experimentally demonstrated only in 2001 by DONUT collaboration [22].

Recently neutrino physics became vivid field, where particle and cosmic ray physics meet together to answer important questions such as: Are neutrinos massive particles? Do they oscillate? The pioneering experiment was mounted and instrumented in 1968 in Homestake Mine by R. Davis [23]. He was able to detect electron neutrinos originated in the Sun. Surprisingly the observed rate was about 1/3 of what was expected from the solar model. The deficit of

fermion's generations				
generation	1	2	3	Q/e
quarks	u (up) d (down)	c (charm) s (strange)	t (top) b (bottom)	+2/3 -1/3
leptons	e ν_e	μ ν_μ	τ ν_τ	-1 0

intermediate bosons	
electroweak interaction	strong interaction
$\gamma,\ W^{\pm},\ Z^0$	g

Table 2.1: Three generation of elementary fermions and the list of intermediate bosons representing different interactions described by the Standard Model.

solar neutrinos was later observed also by other experiments. The most probable consequence and the leading interpretation of this observation is that the electron neutrinos partially oscillate into muon and/or tau neutrinos during their path from the Sun to the Earth. The oscillation could be understood only if neutrino mass eigenstates differ from eigenstates of weak interaction. In these terms the oscillation hypothesis directly requires massive neutrinos.

The Sudbury Neutrino Observatory (SNO), which is the most recent solar neutrino detector, provides a unique measurement of solar neutrino flux in three detection channels. Two of these channels ($\nu_e + d \rightarrow p + p + e^-$ and $\nu_x + e^- \rightarrow \nu_x + e^-$) are sensitive mainly to electron neutrinos, while the third channel ($\nu_x + d \rightarrow p + n + \nu_x$) is equally sensitive to all neutrino species. This allows the experimentalists to study neutrino oscillations without the assumption of the solar model validity. Their results, [24], are in perfect agreement with the oscillation hypothesis. Moreover they agree with the solar theory because the total rate in all neutrino flavors is the same as the prediction of the standard solar model.

The large amount of electron and muon neutrinos is produced also in the atmosphere as a by-product of cosmic ray interactions. These neutrinos are extensively studied and the rate of neutrino species is compared with the theoretical models. Results again suggest the oscillation hypothesis. Furthermore SuperKamiokande results [25] show oscillation pattern in the angular dependence of the muon neutrino flux.

Interactions between elementary particles were described in the framework of the gauge field theory called the "Standard Model". This model provides unification of electromagnetic and weak force by introducing four electroweak mediators

γ, $W^{\pm}$, Z^0 as well as it describes the strong force via the gluon exchange in the so-called Quantum ChromoDynamics (QCD). The existence of all intermediate bosons listed in Tab. 2.1 has been confirmed experimentally. The so-called Higs boson is the only remaining undiscovered ingredient of Standard Model. This particle is supposed to be responsible for endowing mass to the other particles.

Although the Standard Model is well confirmed theory in many aspects, it is in fact an effective tool to describe particle interactions up to energy scale of the order of $\sim TeV$. It is believed that at higher energies new phenomena will appear. One possible theory dealing with this new physics is the theory of supersymmetry (SUSY). Each fundamental particle is connected to its superpartner via this new type of symmetry, fermions to bosons and boosns to fermions. Consequently, many new, yet undiscovered particles are introduced. Certain SUSY models conserve so called "super-charge". In practice it means that decays of super-particles have to produce another super-particle. Consequently the lightest super-particle should be stable in these models.

This Lightest Supersymmetric Particle (LSP) is according to many cosmologists a suitable candidate for dark matter in the Universe. This is again the field where particle physics could be studied by cosmic ray experiments. Cold dark matter (such as LSP) can scatter and thus decelerate in dense regions in the Universe and it can be gravitationally captured by massive objects such as stars or planets. Detectors like e.g. Amanda [26], Antares [27] or Nestor [28] have the ability to search for LSP anihilations to neutrinos in the Earth or Sun centers.

2.2 Cosmic ray energy spectrum and composition

Cosmic rays are bombarding the Earth surface with rather high frequency ($\sim 1\ m^{-2}s^{-1}$ with $E > 10\ GeV$). Their energies extend over more than 12 magnitudes as shown in Fig. 2.1. The flux of cosmic particles is steeply falling with increasing energy. While the cosmic primaries can be observed directly by balloon or satellite experiments up to the energy of about $10^{14}\ eV$, for studying higher energies the large surface or underground detector arrays are needed in order to accumulate enough statistics in reasonable time scale. However, these detector devices do not measure primary particles themselves but they register products of cosmic ray shower evolving in the atmosphere.

The energy spectrum of cosmic rays can be approximately described by single power-law dependency up to the energy of about $10^{15}\ eV$. Between $10^{15}\ eV$ and $10^{18.5}\ eV$ the spectrum is steeper, as better seen from Fig. 2.2. Another change in the slope is observed at the energy of about $10^{18.5}\ eV$. These sudden changes of spectral index at $10^{15}\ eV$ and $10^{18.5}\ eV$ are called the "knee" and the "ankle"

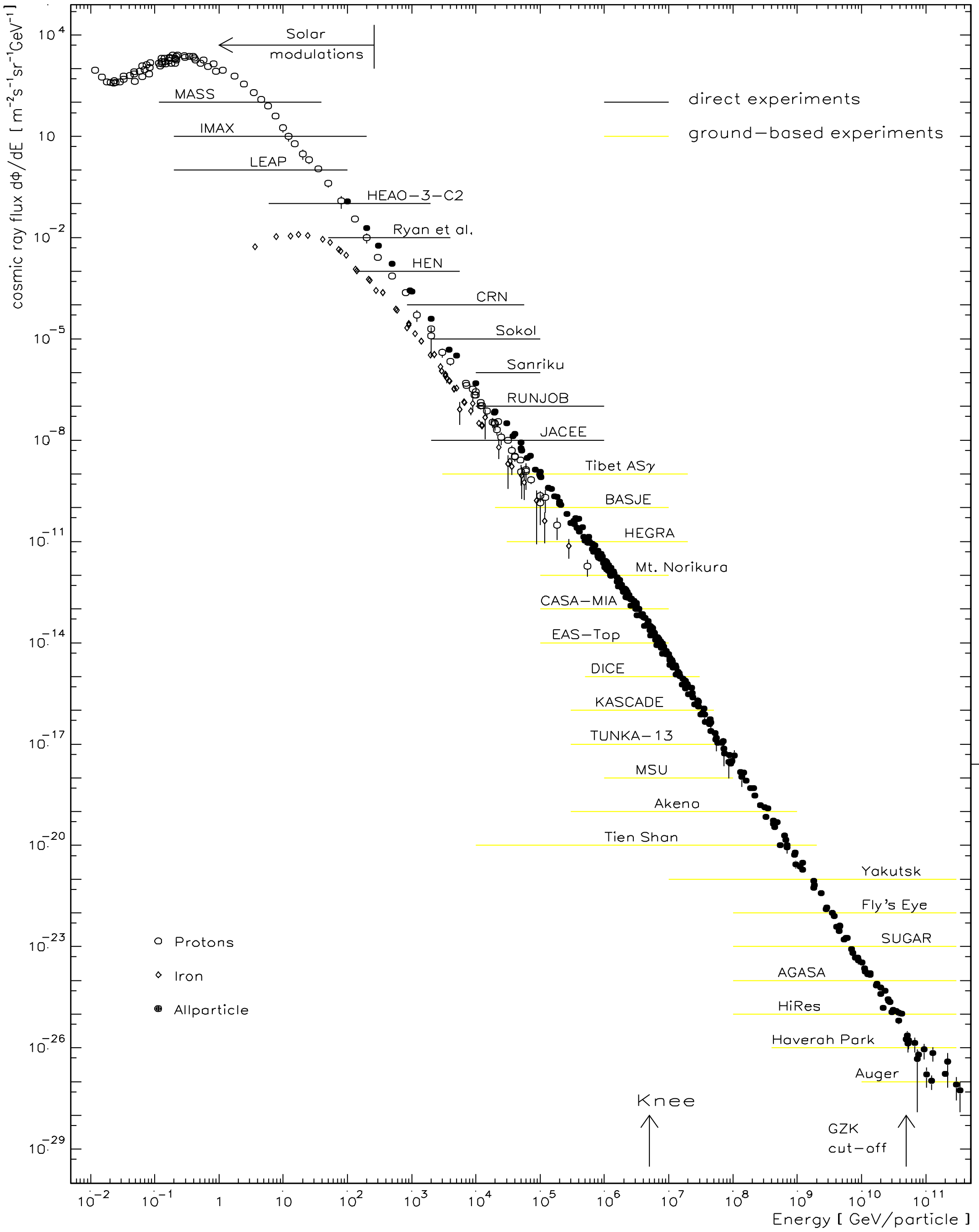

Figure 2.1: The energy spectrum of cosmic rays with energy ranges accessible by various experiments. Picture is taken from [29], where the experiments are referred to.

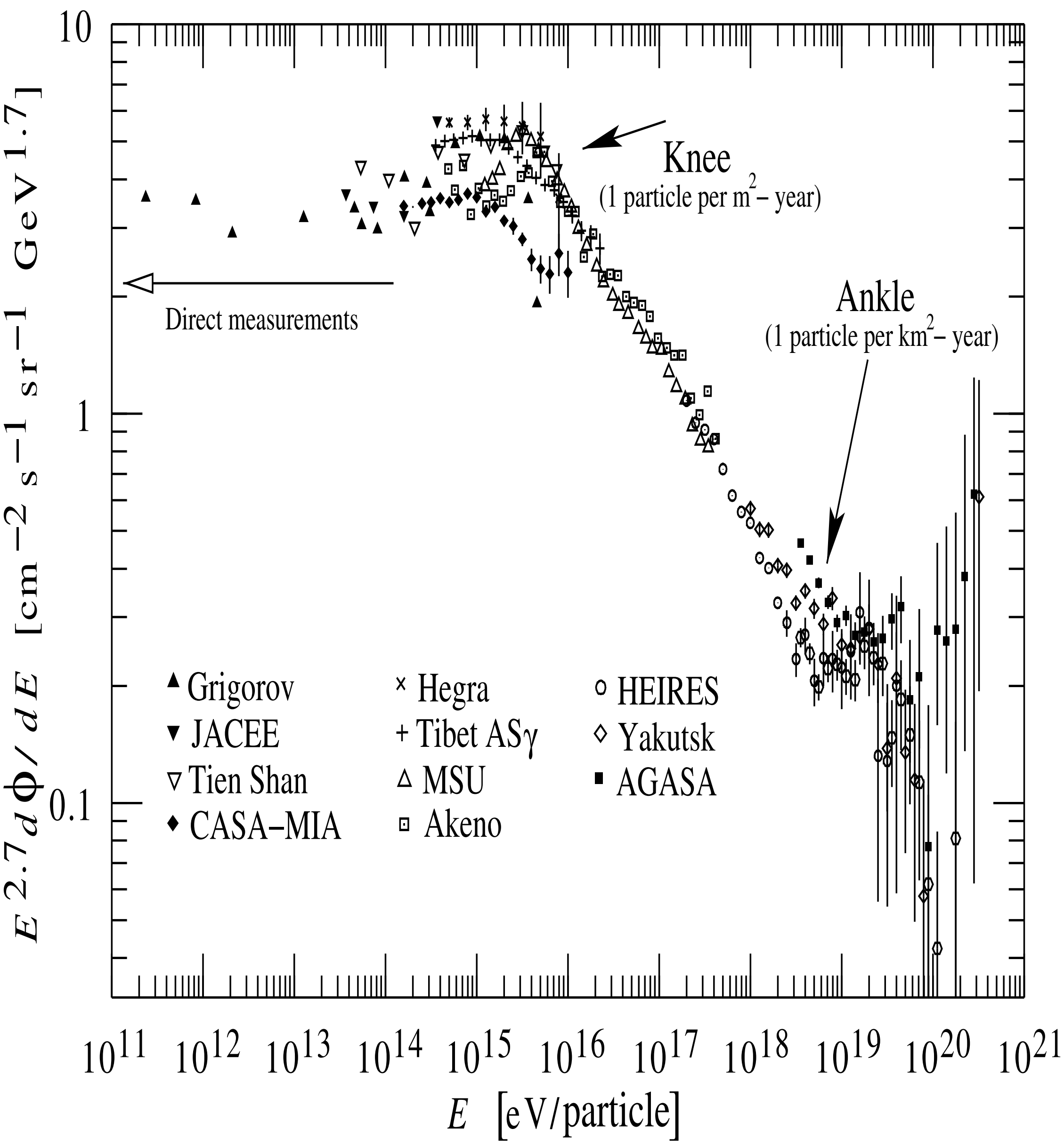

Figure 2.2: The all-particle spectrum of cosmic rays. The picture is the modified version of that from [30] available also at `www.pdg.lbl.gov/2002/fig9_02.eps`. The energy spectrum dN/dE is multiplied by $E^{2.7}$ (E in GeV) in order to emphasize the change of the power-law indices at certain energies, i.e. the presence of the "knee" and the "ankle". The JACEE data are taken from [31], Grigorov [32], Thien Shan [33], MSU [34], Tibet [35], Akeno [36], HEGRA [37], CASA-MIA [38], HIRES [39] and AGASA [40].

respectively.

The electromagnetic component of primary cosmic rays (i.e. photons and electrons) is believed to be negligible above 1 GeV when compared to the hadronic cosmic ray flux. The spectrum below about 10 GeV, i.e. the part not shown in the Fig. 2.2, is strongly affected by solar modulation. The plasma wind emitted from the Sun has intrinsic magnetic field, which deflects the low energy cosmic rays. The intensity of the solar wind varies in about 11 year cycle affecting the observed cosmic ray flux by a factor of 2 at 1 GeV and by about 10% at 10 GeV. The cosmic rays at these low energies are mostly protons. The relative abundances at 2 GeV are: $p(\sim 95.2\%)$, $He(\sim 4.5\%)$ and CNO nuclei $(\sim 0.3\%)$.

The cosmic rays with energies below the knee are believed to be most likely produced by the diffusive shock acceleration and by supernova explosions within our Galaxy. However, no exact source has been localized so far. Some general remarks about particle acceleration are provided in Sec. 2.3. For detailed discussion of the cosmic ray accelerators the interested reader is refereed to [41].

The knee appears as the kink of the spectral curve, characterized by a steepening of the spectrum from $E^{\sim-2.75}$ to $E^{\sim-3.1}$. Several explanations of the knee existence have been suggested. There are three perhaps most developed scenarios.

- A change of the propagation of galactic cosmic rays, corresponding to a more rapid particle escape from the Galaxy [42].
- A change of the acceleration mechanism is directly responsible for the knee. It is argued that the maximal energy of acceleration in supernova shock fronts corresponds to the knee energy, e.g. [43].
- Presence of only one or few sources (supernovae) nearby the Earth. The consequences of this assumption to the cosmic ray spectrum are developed in [44].

In the first scenario the rigidity cut-off due to the galactic magnetic field is involved:

$$p_{max} = ZeBL, \tag{2.1}$$

where p_{max} is the maximum momentum of particles to circulate inside the Galaxy, Ze is the particle charge, B is the mean magnetic field inside the Galaxy and L is the characteristic galactic size. For momenta above p_{max} a rapid particle escape out of the Galaxy is expected. In fact, for different cosmic ray nuclei, there are different rigidity cut-offs depending on the particle charge. The larger the charge Ze, the greater the maximal momentum p_{max}. The increased abundance of heavier nuclei is thus expected at energies above the first rigidity cut-off (i.e. above cut-off for the lightest component - p).

The composition studies at the knee are of the large interest, however, no definite conclusion has been drawn yet. Some results are even contradictory. The estimation of the cosmic ray composition suffers from large systematic errors mainly due to the uncertainty in Monte Carlo models describing the nucleus-nucleus interactions during the air shower development. The detailed discussion of this problem is provided in [46]. Fig. 2.3 demonstrates current status of the problem. The selected composition results clearly differ between experiments.

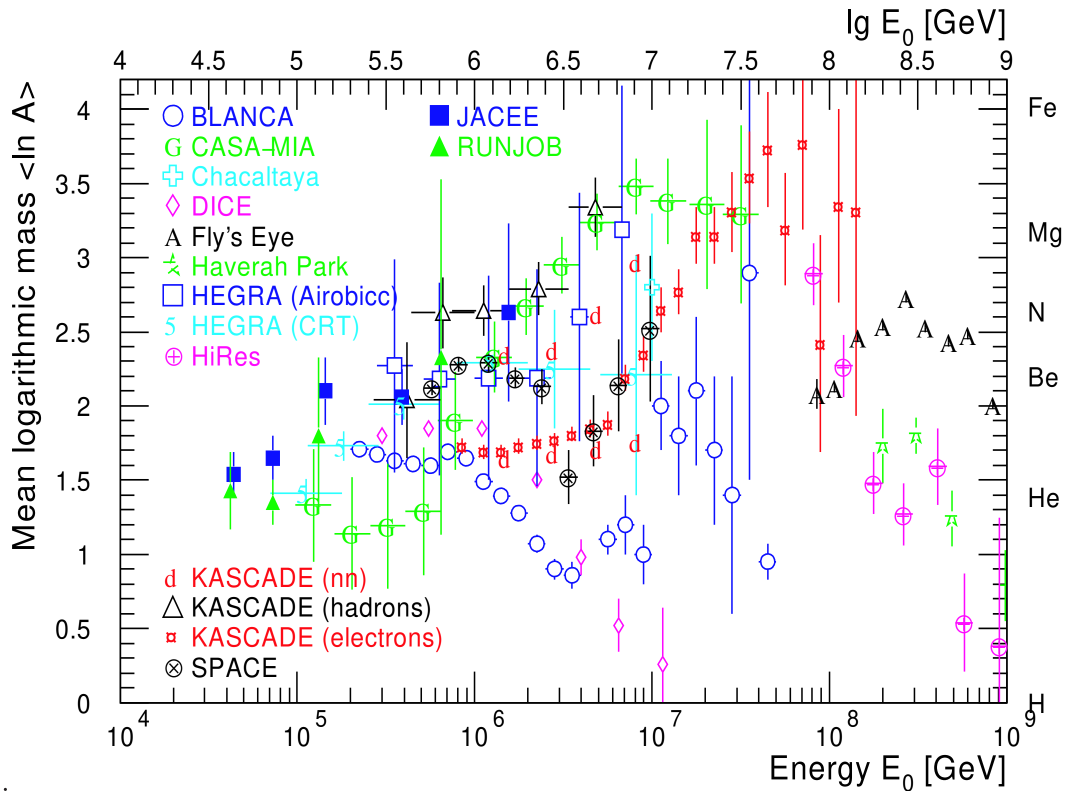

Figure 2.3: Mean logarithm of the primary particle mass as a function of the energy for selected cosmic ray experiments, compilation from [45].

The ankle at about 10^{18} eV is characterized by the hardening of the energy spectrum. In the framework of the previous ideas, the confinement of cosmic particles within our Galaxy is expected to end even for the heaviest nuclei. The cosmic rays at these energies are thus believed to be of extra-galactic origin.

Recently, Ultra High Energy (UHE) cosmic rays ($E > 10^{20}$ eV) have become the topic of the highest importance. Soon after the discovery of 2.7 K black body relict radiation, it was pointed out by Greisen [47], Zatsepin and Kuzmin [48], that very high energy protons react with the relict microwave photons

$$p \ + \ \gamma_{2.7\ K} \rightarrow \Delta^{+} \rightarrow p \ + \ \pi^{0} \quad (\ n + \pi^{+} \ ). \tag{2.2}$$

The reaction threshold is about 6 10^{19} eV. The process (2.2) is often called photo-disintegration. Below the threshold energy the proton attenuation length is 1000 Mpc, while above the threshold it is reduced only to 20 Mpc. Similar effect appears also for heavier nuclei.

If the UHE sources are extra-galactic, the distance between the source and the Earth is much higher than 20 Mpc. Thus the primary particle has to pass several subsequent interactions of the type (2.2) until it reaches the Earth. In each of these interactions the energy of the incident particle is reduced, and the process stops when the resulting energy drops bellow the threshold of photo-disintegration. The effect is demonstrated in Fig. 2.4 where mean proton energy is plotted as a function of propagation distance. An endpoint of the cosmic ray spectrum is thus expected around 10^{20} eV. This end of the cosmic ray spectrum is often called the GZK cut-off. Recent measurements by AGASA experiment observed significant number of events above the GZK cut-off. If this observation is confirmed, it would have important consequences. Several proposals have been already suggested:

- bottom up scenario: the sources are close (in the astronomical sense) to the Earth,
  - e.g. nearby active galactic nuclei
  - nearby gamma ray bursts
  - jets of large radio galaxies, etc.
- top down scenario: decays of unknown exotic and very heavy particles, decay of topological defects, etc.

If the bottom up scenario is correct, other theoretical problems occur. No current astrophysical theory can explain particle acceleration to such high energies. If, however, the top down scenario is the right one, the physics beyond the Standard Model is needed to explain decays of unknown heavy particles.

However, recent measurements from the HiRes experiment, in contrast to AGASA, are in agreement with expectation of the GZK cut-off. Experiments of new generation are planed or already under construction (EUSO and AUGER respectively). So hopefully the near future will shed more light onto this exciting field of UHE cosmic rays.

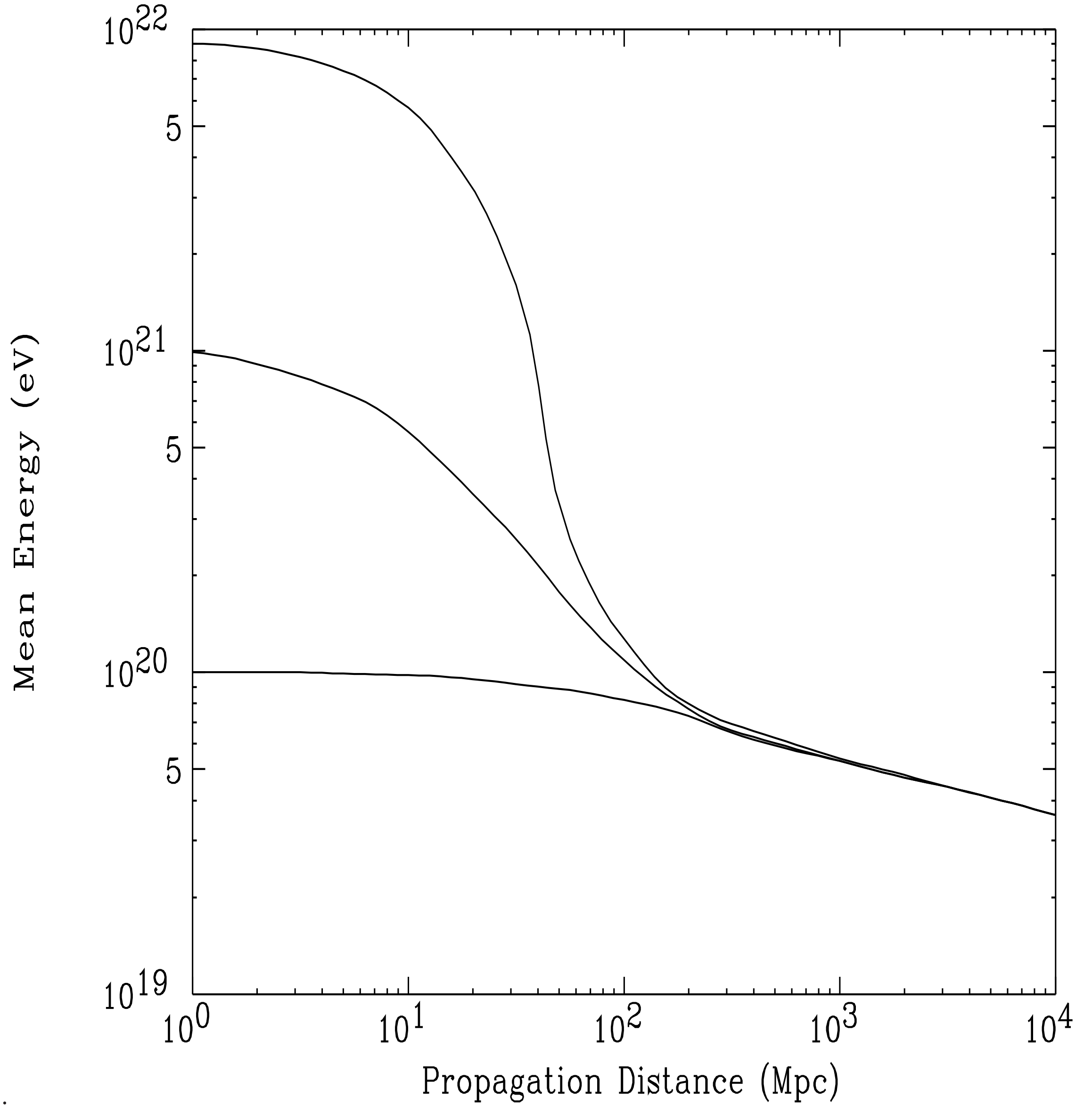

.

Figure 2.4: Mean energy of protons as a function of propagation distance in case of 3 proton primary energies $10^{22},\ 10^{21},\ 10^{20}\ eV$. For reference see [49].

2.3 Particle acceleration

Charged particles can accelerate directly in electric field (direct acceleration) or they can gain energy via random scattering in magnetized plasma (Fermi statistical acceleration).

In case of direct acceleration the electric field can be induced by time changing magnetic field. This could be realized by rotation of some accretion disk or magnetic neutron star. Direct acceleration cannot reproduce observed power law spectrum. Consequently, it probably does not significantly contribute to the total spectrum of cosmic rays. However, no definite conclusions are drawn yet and this mechanism is still intensively studied.

In 1949 Fermi suggested statistical mechanism "according to which cosmic rays are accelerated in interstellar space of the galaxy by collisions against moving magnetic fields" [50]. Schematic picture of Fermi idea is shown in Fig. 2.5. Charged particle can either gain or lose energy in the scattering, however, it could be shown (e.g. [51]) that on average there is net energy gain $< \Delta E >$:

$$< \Delta E > \sim E \frac{4}{3} \beta^2 \ , \tag{2.3}$$

where E is the initial energy of particle and β is the plasma velocity with respect to speed of light.

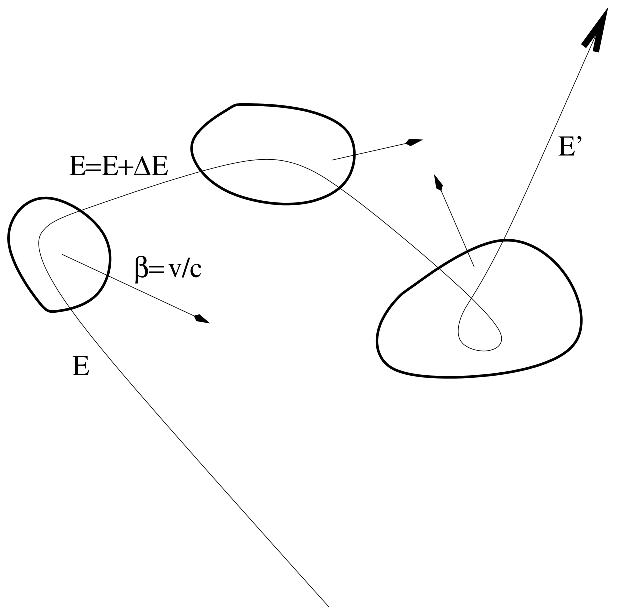

Figure 2.5: Fermi original idea: charged particle scatters inside the cloud of magnetized plasma

It is assumed, that the scatterings inside the cloud are caused by magnetic field only and therefore they are elastic. Scatterings on magnetic field play similar role as diffusion of ink droplets inside glass of water. In the rest frame of moving gas, the entering particles randomize momenta inside the cloud volume with equal probability to escape in any direction. Going back to the laboratory frame, the "average" motion of particle becomes to coincide with the gas motion. While some particles can be decelerated, on "average" the particles are boosted (accelerated).

Fermi mechanism predicts differential power law spectrum

$$N(E_0 < E < E_0 + dE) \sim E^{-\alpha} \ .$$

However, parameter α turned out to be much larger than what is measured. Moreover, there is another argument, why this type of acceleration cannot reproduce measured rate of cosmic rays. Cloud velocity β appears in second power in Eq. 2.3. While β is essentially small in case of interstellar plasma clouds, the acceleration is too inefficient.

Because of factor β^2, Fermi original idea is often called second order Fermi acceleration.

First order Fermi acceleration

It was shown (e.g. [52]) that the Fermi idea can be modified in order to describe more powerful acceleration which takes place in supernovae shocks.

Ejected material from supernova propagates to the interstellar medium with rather high velocity of the order of 10^4 $km\ s^{-1}$. This is 4 orders of magnitude higher than the sound speed in interstellar medium. The strong wave propagates with velocity $-\vec{u}_1$ and the shocked gas flows away from the shock front with velocity $\vec{u}_2$. The situation is demonstrated in Fig. 2.6.

The significant advantage of this modified mechanism is that the plane geometry ensures the energy gain in any incoming and out-coming direction. It furthermore improves dependency of the average energy gain $< \Delta E >$ on the gas velocity $\beta = (u_1 - u_2)/c$:

$$< \Delta E > \sim E \frac{4}{3} \beta \ . \tag{2.4}$$

Factor β appears in Eq. 2.4 only in first power. Consequently the mechanism is much more efficient.

When combined with model of cosmic ray propagation, it could be shown that the first order Fermi mechanism predicts power law spectrum. Contrary to Fermi original scheme, the power law index α is now consistent with observations $\alpha \sim 2.7$.

The acceleration in supernova remnants is limited only to energies smaller than $\sim 10^{15}$ eV. Above this energy the magnetic field is just not able to confine

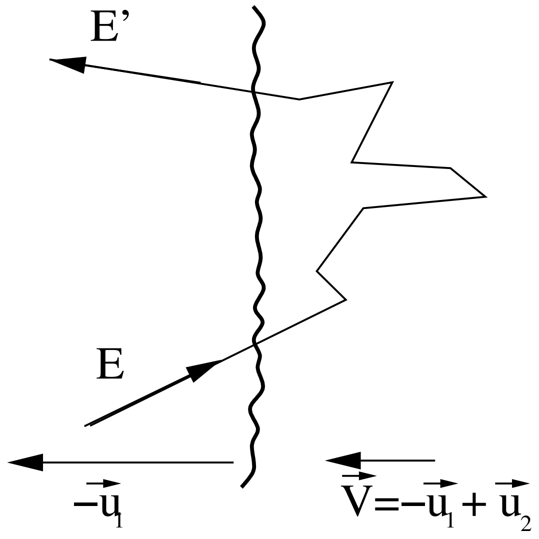

Figure 2.6: Plane shock front accelerates the cosmic ray particle.

particles within the acceleration volume for sufficiently large time. This energy roughly coincides with the knee in cosmic ray spectrum. Consequently it is a possible explanation of the spectrum steepening at the knee. More energetic particles have to be produced by different sources outside our Galaxy (like active galactic nuclei, lobes in radio galaxies, etc.).

Hillas condition

Independently on the acceleration mechanism, simple argument can be used in order to express upper bound of energy which can be reached in acceleration process. Suppose a region of acceleration with characteristic dimension R and magnetic field B. The idea is that charged particle can be accelerated inside such region up to the energy, where the Larmour radius r_g reaches critical value $R/2$, i.e. $2r_g < R$. Taking into account characteristic velocity β of scattering centers this condition leads to Hillas inequality [53]:

$$B[\mu G]R[pc] > 2\frac{E[10^{15}eV]}{Z\beta} \ . \tag{2.5}$$

The formula can be expressed in terms of so called Hillas plot which is given in Fig. 2.7. It shows a simple idea that to accelerate charged particles to high energies either large magnetic fields or large sources of acceleration are necessary. Various candidates of cosmic accelerators are placed in the plot: neutron stars, white dwarfs (both are representants of direct acceleration), supernova remnants (SNR), active galactic nuclei (AGN), lobes of radio galaxies, colliding galaxies, etc. The higher the up-right position of the spot in the plot, the higher energies can be reached in the corresponding candidate source.

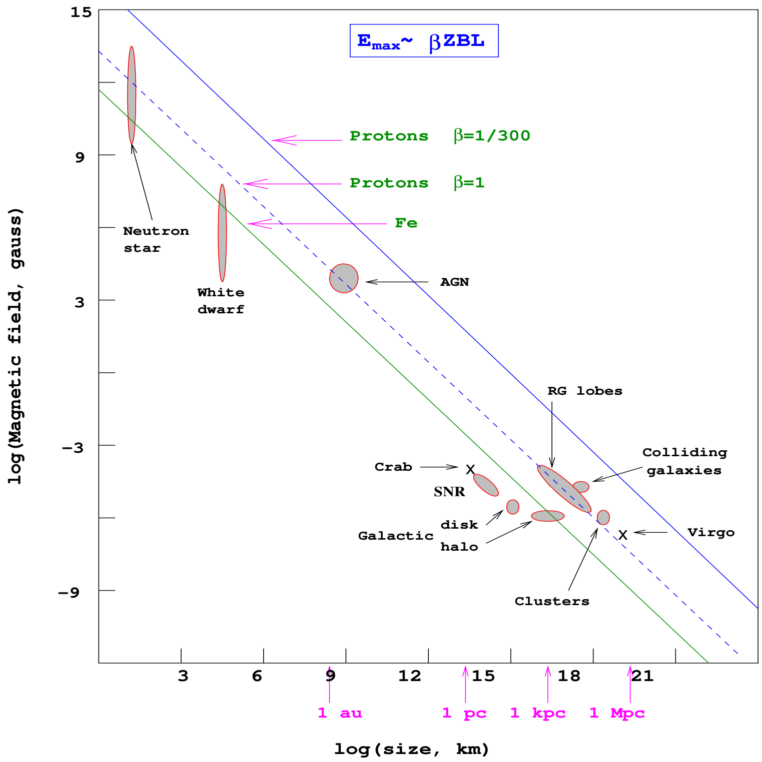

Figure 2.7: The Hillas diagram. Magnetic field strengths and characteristic dimensions are plotted for various candidate sources of accelerated particles. Only objects above the diagonal lines can accelerate particles to 10^{20} eV. Lines are given for two primaries (proton, iron) and for different velocities β of magnetic scattering centers. The meanings of abbreviations are given in the text. Picture comes from [54].

2.4 Atmospheric showers

If the high energy particle enters the upper atmosphere, it interacts with an air nucleus and generates the atmospheric shower, Fig. 2.8. The process creates number of secondaries moving almost at the same direction as the impinging particle. Each of these secondary particles can interact again with the air nucleus and unstable particles can also decay. The process repeatedly continues until the energy of generated secondaries drops below the threshold for particle production. If the particle energy is less than certain threshold, the energy only continuously decreases by radiative processes such as the ionization. Consequently, some of the particles can even stop in the atmosphere transforming all their energy into the ionization electrons. Thus, each shower has certain atmospheric depth where the number of particles reaches its maximum. Three components, hadronic, muonic and electromagnetic, are created in each shower.

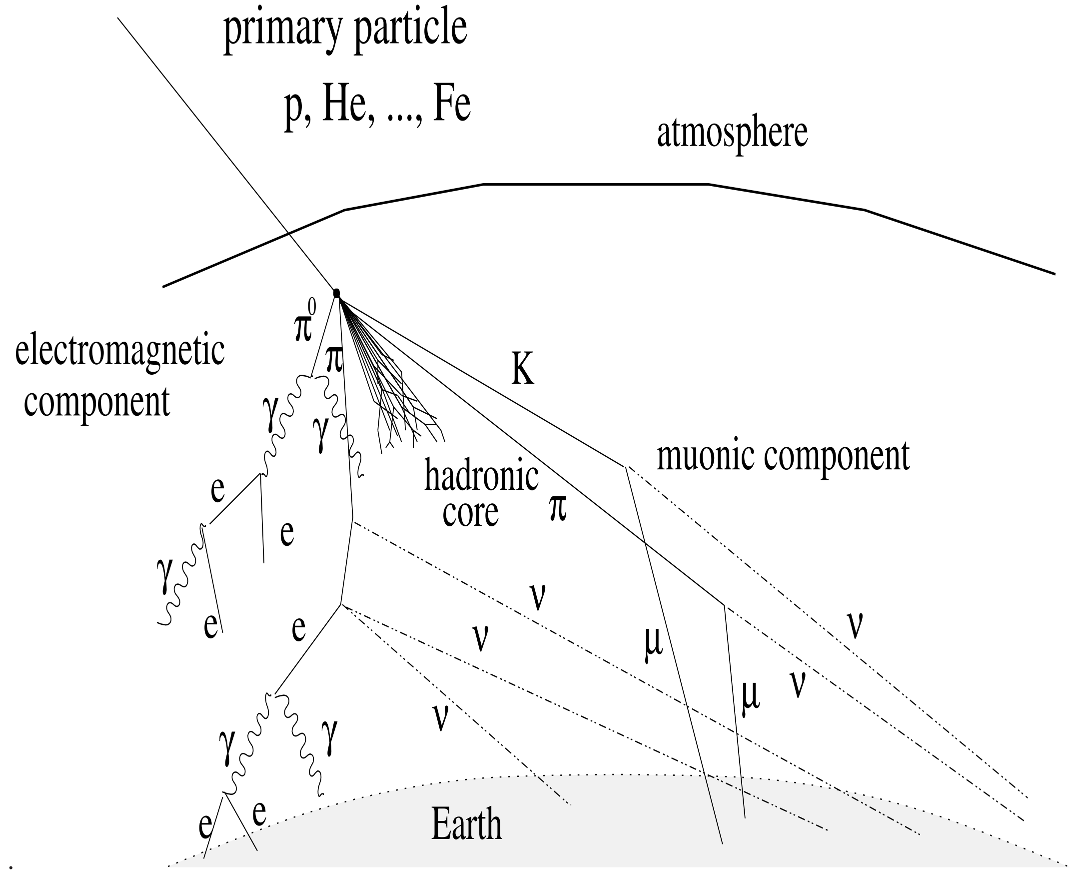

Figure 2.8: Schematic view of an air shower with separated hadronic, muonic and electromagnetic component.

The lateral extension of the shower is increasing function of the atmospheric depth[2]. This is mainly due to Coulomb scattering of the electromagnetic component. In addition, however to smaller extent, the opening angles of secondary particles (as seen from the Earth reference frame) increase as the energy of interacting particles decreases.

In the case of a hadronic primary, the strong interactions are involved in collisions with the air nuclei. The generated hadronic component creates the core

[2]The atmospheric depth is decreasing function of the altitude, i.e. the zero atmospheric depth corresponds to the most distant point of the atmosphere from the Earth surface (see Sec. 2.6.6)

of the shower. The decays of mesons from the hadronic core create leptons, which then form the muonic and electromagnetic component.

The **hadronic component** consists of protons, neutrons, other baryons and mesons, which are produced by the strong interaction of the incoming primary particle and by further interactions. Produced hadrons can either re-interact with another air nucleus or decay. In the case of interaction, a new sub-shower is initiated at energies high enough. For lower energies of interacting hadron, the disintegration of target nucleus occurs without creation of further hadron sub-shower. At even smaller energies, the air nucleus can only excite and later emit low energy γ ray. The muonic and electromagnetic component originate from hadron decays into leptons .

If the primary particle energy is about 10^{14} eV or higher, the **electromagnetic part** of the shower reaches the Earth surface and can be easily detected. The main processes relevant for development and formation of the electromagnetic shower are Compton scattering, bremsstrahlung and pair production. The electromagnetic part has practically no penetrating power and thus cannot be detected below the Earth surface.

The most penetrating part of the shower is the **muonic component**. Muons are created mainly in $\pi^{\pm}$ or $K^{\pm}$ decays from the hadronic component. During their passage through the atmosphere muons loose their energy primarily by ionization, i.e. further muon interactions with the air nuclei do not play any important role. The life time of muons is increased by the time dilatation, consequently muons reach the ground and penetrate below the Earth surface as deep as their energy allows[3]. Muons can be also produced by decays of charmed and beauty particles. Since the charm mesons have very short lifetime, muons originating from such decays are called "*prompt*" muons.

The charged particles with velocity larger than the velocity of light in the atmosphere produce **Čerenkov light**. The Čerenkov photons are emitted in the cone with the opening angle $cos(\Theta) = 1/n\beta$, where β is the particle velocity and n the refractive index of the atmosphere.

To complete the list of important components and aspects of the cosmic ray shower, the presence of **fluoresce light** has to be mentioned. It is caused mostly by excitation of N_2 molecules in the air by charged particles from the shower. As a result, the ultraviolet scintillation light is subsequently emitted, contrary to the Čerenkov light, isotropically into all directions.

In fact, the primary particle can be also high energy γ. Then, hadronic and muonic components in the shower are suppressed, because processes like $\gamma + nucleus \rightarrow hadrons$ (i.e. photo-production) are less favorable than e^+e^- pair production or bremsstrahlung. In addition, the $\mu^+\mu^-$ pair production is

[3]Typical muon energy loss in the rock is about 2 GeV/m.

suppressed (when compared to e^+e^- pair production) by a factor about $3\ 10^{-3}$. Consequently, in the case of primary γ, the shower is dominated by the electromagnetic part. These significant differences between hadronic and photon shower allow to distinguish them.

2.5 Air shower detectors

Depending on the measured component of the air shower, the cosmic ray detectors can be divided into several types - extensive air shower arrays on surface, Čerenkov, fluorescence telescopes and underground muon detectors,.

2.5.1 Extensive Air shower arrays

Surface arrays consist typically of large number of small detectors ($1 - 10\ m^2$). These subdetectors are often scintilators equipped with photomultipliers. Part of the array can consist of muon detectors (shielded scintilators can be the simplest realization). Comparing the arrival times in distant detectors the shower direction can be estimated. The total number of particles in the shower on the surface is usually calculated on the event by event basis by fitting the particle densities to the lateral distribution function[4]. The number of particles is correlated with the primary particle energy.

AGASA experiment in Japan which covers area of about 100 km^2 has been so far the world largest array. Recently AUGER project in Argentina has surpassed this record extension. The AUGER experiment will be finally operated with rather impressive detection area of about 3000 km^2.

2.5.2 Čerenkov telescopes

Typical Čerenkov telescope includes parabolic reflectors to collect light, phototubes in the focal plane, and precise electronics to measure photoelectrons. These devices are widely used in γ astronomy in TeV range, because they efficiently allow experimentalists to distinguish between primary protons and gammas. The key point is the different shower profile of γ and p induced showers. On the other hand, the small opening angle makes these devices less efficient for detection of high energy cosmic rays. The HEGRA Imaging Cerenkov Telescope is a nice example of this measurement technique.

[4]The lateral distribution functions have been established by Nishimura and Kramata and later parameterized by Greisen. The Greisen parameterization is known as the NKG formula [55].

2.5.3 Fluorescence telescopes

Fluorescence telescopes also consist of focusing mirrors and photodetectors in the focal plane. Contrary to Čerenkov light, the fluorescence photons are emitted isotropically. Since the air is an inefficient scintilator, the usage of the fluorescence telescopes is limited only to showers with energies exceeding 10^{18} eV. HiRes in the USA or AUGER constructed in Argentina are good examples of the fluorescence method. In addition to the fluorescence measurement the Auger experiment will provide surface array data as well. Combining two independent experimental techniques (for the first time) the cross-calibration will be possible. The significant disadvantage of fluorescence detectors is the fact, that they can operate only during moon-less nights.

2.5.4 Underground muon detectors

Underground muon detectors vary much more than the surface arrays, because they were usually built for different purposes. For example MACRO experiment in Italy has been built for searches of monopoles, or FREJUS in France for the proton decay studies. The LEP detectors were successful e^+e^- collider experiments, allowing simultaneous detection of cosmic events as a by-product.

Sensitive detector can be muon chamber, photodetector to collect Čerenkov light from (water) radiator, or (in the case of cosmic studies by LEP detectors) Time Projection Chamber (TPC) or the hadron calorimeter.

The significant characteristic of an underground detector is the amount of overburden under which the apparatus is situated. This parameter determines the minimal energy of the muon on the Earth surface so that it can reach the underground detector. This minimal energy varies from several tens of GeV (LEP experiments) to the TeV range (MACRO). The underground location determines also the observed muon rate as seen from Fig. 2.9.

The events appear in the detector as single or multi-muon events. A spectacular multi-muon event as seen by Koral-Gold field, [57], is displayed in Fig. 2.10. This experiment is the deepest underground detector ($h = 6045$ hg/cm^2 water equivalent) and it was originally designed for proton decay studies. The sensitive units are proportional counters. The multiplicity ~ 20 within the area 6×6 m^2 for this particular event corresponds to the primary particle energy about 10^{18} eV. This rare event is one of the most energetic events ever observed by the muon underground detectors.

Muon detectors situated underground probe different properties of the incoming shower when compared to surface arrays. Hard muon component originates from first interactions at high altitudes above the Earth surface. This fact is demonstrated in Fig. 2.11, where the muon rate is plotted as a function of the generation from which the muon originates. Generation number 1 corresponds to the first, primary interaction of a cosmic nucleus with the atmosphere. Any interaction results in production of mesons like $\pi^{\pm}$, $K^{\pm}$ that subsequently decay in the thin air with high probability into detected muons.

The atmosphere works similarly as a calorimeter in an accelerator experiment. While the surface arrays probe the last layer of that calorimeter, the underground detectors effectively study the first layers, however, only in the hard muon component. The information obtained from underground detectors is important for understanding the shower at its origin and it is complementary to the information obtained from the surface arrays.

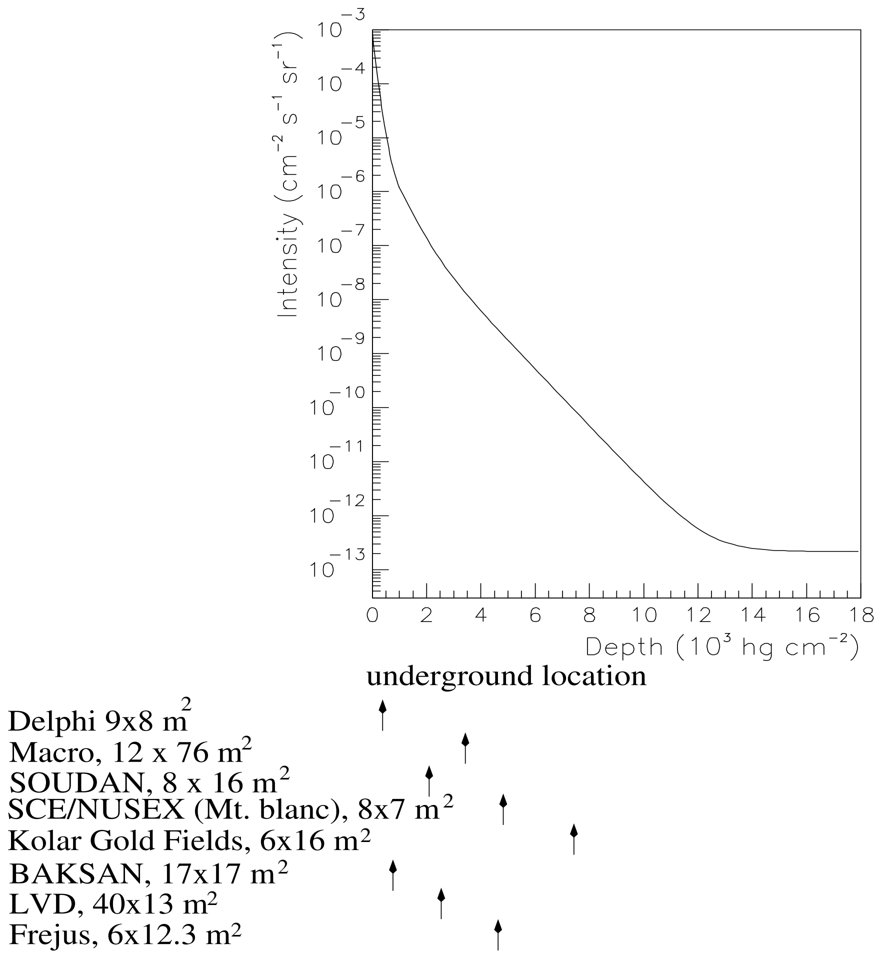

Figure 2.9: The vertical muon intensity as a function of underground depth. The underground location of several experiments is marked by the arrows. Picture is taken from [56] and it represents fit through various experimental measurements.

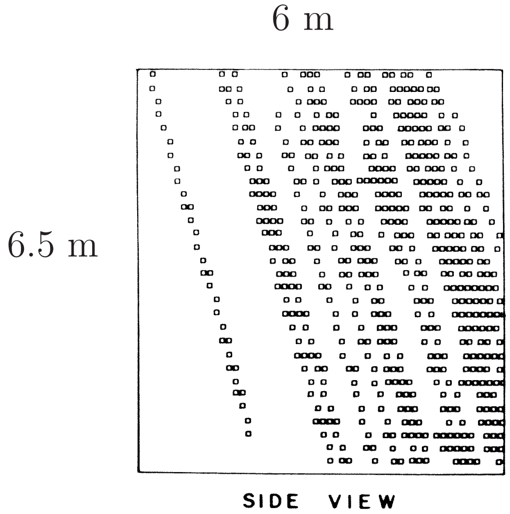

Figure 2.10: Spectacular multi TeV event from Koral Gold field experiment, [57]. About 20 muons are in the detector.

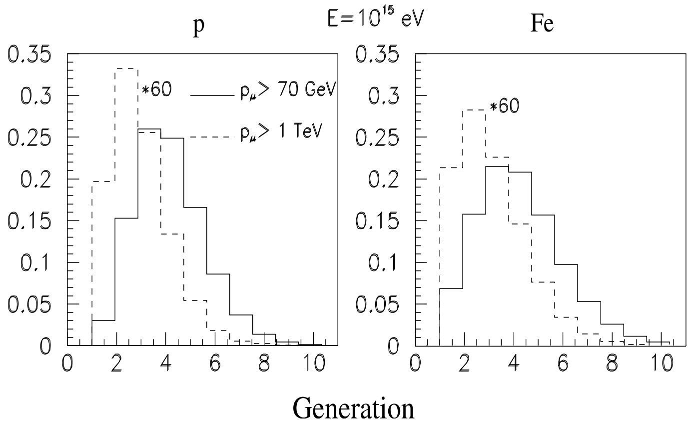

Figure 2.11: Muon rate as a function of generation from which muons originate. Showers with energy 10^{15} eV are plotted in case of proton and iron primary particle. The result is displayed for two imaginary detectors with different energy cutoffs for vertical muons, $p_{CUT} = 70$ GeV, 1 TeV. Histograms are normalized to the total number of events in the case of 70 GeV cutoff. The 1 TeV result is multiplied by 60 to be visible when compared to 70 GeV result.

2.6 Simulation of Extensive Air Showers

The analysis and interpretation of EAS data requires a detailed modeling of a number of processes that occur during the shower evolution. Detailed Monte Carlo calculations are usually used for this purpose. Present knowledge of high energy strong and electroweak interactions has to be taken into account in the simulation code. The most common tool used for simulations of EAS is CORSIKA [1] simulation package originally developed for analysis of KASCADE experimental data. The abbreviation KASCADE stands for KArlsruhe Shower Core and Array DEtector. This experiment is a unique tool for analyzing cosmic ray showers between $10^{14} - 10^{17}$ eV [58]. It is able to measure electromagnetic, muonic [59] as well as hadronic [60] component of the shower.

Since CORSIKA program is used also in this work, a brief overview how CORSIKA represents relevant physical process is given in next sections. For more detailed description the reference [1] is recommended.

2.6.1 Hadronic interactions

Hadronic interactions in CORSIKA are described in two levels according to the energy of hadronic collision. At energies higher than certain value, the interactions are described by one of the models VENUS [61], QGSJET [2], DPMJET [62], SIBYLL [63, 64] or HDPM [65]. If the interaction energy is less than 12 GeV in Center of Mass System (CMS) of interacting hadrons, the GHEISHA [66] subroutines are called. The GHEISHA model has been used for many years by accelerator physicists in various kinds of simulations. In principle also low energy model should be optional like the high energy one. Currently FLUKA is tested as replacement of GHEISHA.

Most of the hadronic interaction models (VENUS, QGSJET, DPMJET, HDPM) at high energies are based on the Gribov-Rege theory considering single or multiple pomeron exchanges. Pomerons are then cut to color strings, which are later fragmented by a procedure similar to the Lund algorithm [67] used for description of hadronization in collider experiments. The SIBYLL interaction model has been essentially designed for the usage in EAS Monte Carlo programs. It is not based on the Gribov-Rege theory. After the nucleon-nucleon collision, the projectile and target particles fragment into quark-diquark or quark-antiquark systems. The created color strings are then fragmented into observed hadrons in the similar way as in the usual Lund algorithm. Models QGSJET, DPMJET, HDPM and SIBYLL include minijet production as well. The minijet effects are of increased importance at high energy. The VENUS model, which does not describe the minijet production at all, is thus recommended not to be used above $2\ 10^{16}$ eV.

The nucleus-nucleus interactions are usually simulated using Glauber model, where number of participating nucleons is determined geometrically assuming Gaussian or Woods-Saxon distributions of nuclear density. The nuclear fragmentation of non-interacting nucleons (spectators) is treated in two extreme ways, either all spectators are taken as free nucleons (total fragmentation) or they are kept together as one nucleus (no fragmentation). The effect of the chosen option does not influence the shower development too much, basically it was shown that the effect is smeared out by shower fluctuations. However, there are more advanced options in CORSIKA, where the spectators are kept together and the excitation energy of the remaining nucleus is calculated. The value of excitation energy determines the number of evaporating nucleons or α particles.

Current version of CORSIKA offers VENUS, QGSJET, DPMJET, SIBYLL and HDPM models. From detailed KASCADE studies [68], it follows that the EAS data prefer QGSJET. This model describes best various correlations between different shower components (hadronic, electromagnetic and muonic). Last but not least the QGSJET model saves the CPU time during computer simulations when compared to other models (e.g. VENUS). Because of the above mentioned arguments, QGSJET has become the standard tool to simulate and interpret EAS data.

The details of the differences between models together with various tests of model validity can be found in [69].

2.6.2 Mean free path and decay length

The distance the particle traverses before it interacts with the air nucleus is determined by the inelastic cross section together with the atmospheric density distribution along the particle path. In general, particle decay and inelastic interaction are two competitive processes.

According to statistical nature of both processes two quantities (l_D and l_I) are randomly generated. Parameter l_D is the path length the particle travels before it decays. Quantity l_I is the length the particle passes through the medium before it interacts. The shorter value is taken as the actual path length to the decay point or to the interaction vertex. By this method it is decided which process (decay or interaction) is realized. If the traced particle is a stable one, only interactions occur. If the particle decays, all decay modes with a branching ratio higher than 1% are taken into account.

The products of a particular decay mode are generated according to theoretical distributions of relevant kinematical variables, that uniquely characterize the final state (i.e. the angular distributions of decay products). The decay is performed in CMS system and kinematical variables of the products are then transformed to the laboratory frame by Lorenz transformation. For detailed description of various decays simulated in CORSIKA see [1].

Some important aspects of CORSIKA are:

- Inelastic interactions of **muons** are very rare and they are omitted in CORSIKA. Processes simulated in case of muons are the muon decay, bremsstrahlung and e^+e^- production.

- The mean free path of a **nucleon** n in air is determined by the hadronic cross sections σ_{n-N_i}, where N_i is the i-th component of air[5]. The numerical values of σ_{n-N_i} depend not only on the energy of the collision but also on the interaction model used. The total cross section in air

$$\sigma_{n-air} = \sum_{i=1}^{3} n_i \sigma_{n-N_i} \tag{2.6}$$

  is calculated as the weighted sum of individual cross sections of air components with the atomic fraction n_i. The three component atmosphere is assumed in CORSIKA. The mean free path λ_{free} is calculated using the formula

$$\lambda_{free} = m_{air}/\sigma_{n-air} \ , \tag{2.7}$$

  where $m_{air} \sim 14.5\ g/mol$ is the average atomic weight of air. The resulting λ_{free} is than obtained in g/cm^2. The probability P of the particle to cross a layer of air with thickness λ without interaction is given by

$$P(\lambda) = e^{-\lambda/\lambda_{free}} \ . \tag{2.8}$$

  As already mentioned nucleon-air cross sections at low energies are supplied by GHEISHA. Both nucleons, protons and neutrons, are treated as stable particles.

- **Nucleus-nucleus** cross sections are calculated according to Glauber theory [70] using nucleon distributions inside nuclei. Nucleon distributions are derived from measured charge distribution of relevant nucleus taking into account the finite size of the proton with a mean square charge radius $< r_p^2 >^{1/2} \sim 0.86\ fm$. The SIBYLL model provides its own table of nucleus-nucleus cross sections independently of the Glauber theory.

- **Pions and kaons** are typical examples, where the decay and strong interaction compete. The mean decay length l_D^0 (in cm) is determined from the meson life time τ using

$$l_D^0 = c\tau\gamma\beta \ , \tag{2.9}$$

[5] Used atmosphere composition is defined in Sec.2.6.6

where c is the speed of light, γ and β are usual relativistic factors. In order to express the mean decay length in g/cm^2, the air density and its variation along the path have to be taken into account. The probability P that particle travels at least the distance l before it decays is

$$P(l) = e^{-l/l_D^0}. \tag{2.10}$$

The interaction lengths are treated similarly as in the case of nucleons according to Eq. 2.7, 2.8. Neutral pions have very short life time $\tau \sim 8\ 10^{-17}\ s$ and their probability to interact is negligible for showers with $E < 10^{14}\ eV$. Below this energy the π^0 interactions are omitted. Above this value, both decays and interactions are taken into account. At $10^{18}\ eV$ the decay length is comparable to the interaction length.

- **Other particles** such as ρ, K^*, and Δ have very short life time $\sim 10^{-23}\ s$ and thus they decay immediately without being traced. The η meson is similar to π mesons. Strange baryons $S = \pm 1,\ \pm 2,\ \pm 3$ are produced by most models and since their mean free path is large, only decay is simulated. Contrary to resonances, their life time $\tau \sim 10^{-10}\ s$ is not small and they have to be traced before the decay occurs.

2.6.3 Electromagnetic interactions

Electron and photon interactions are simulated with Electron Gamma Shower system (EGS4) or with the analytic Nishimura Kamata Greisen (NKG) formula. The former option produces all information about the electromagnetic shower and it simulates all particles in the shower. The latter case saves computing time, but gives only the electron densities (calculated analytically) at certain detection plane.

EGS includes simulation of e^+e^- annihilation, Bhaba scattering, bremsstrahlung, Mϕller scattering and multiple scattering (via the Molière's theory). For gamma rays, following processes are simulated: e^+e^- production, photoelectric reactions, Compton scattering. Methods of simulation of these processes are described elsewhere (e.g. in [71]).

Despite small cross section of photo-production for muons, this process has to be simulated, because it is important channel of muon production in γ ray induced showers. In the limit of high energies $E_\gamma > 1\ TeV$ the suppression of μ pair production (with respect to e^+e^- production) becomes

$$\sigma_{\mu^+\mu^-} = \frac{m_e^2}{m_\mu^2}\sigma_{e^+e^-}\ . \tag{2.11}$$

The description of photo-nuclear processes is based on the assumption that only one nucleon from the target nucleus actually interacts with incoming γ. Gamma-nucleon cross sections are calculated according to empirical formula fitted to experimental data of experiments such as H1 or ZEUS. The number of pions produced in photo-nucleon reaction is a function of energy. While only one pion is produced for $E_\gamma < 0.4\ GeV$, between $1.4 - 2.0\ GeV$ always two pions are produced. In the intermediate energy range from $0.4\ GeV$ to $1.4\ GeV$ the probability for producing only one pion decreases linearly with energy. Within the energy range $2.0 - 3.0\ GeV$ CORSIKA decides whether two pions are produced in standard way or the HDPM model is used for describing multiparticle production. Above $3\ GeV$ only HDPM model[6] is used and for energies above $80\ GeV$ the selected interaction model (VENUS, QGSJET, etc.) is applied. For detailed discussion of photo-nuclear processes see again [1].

In the NKG option the electromagnetic component is calculated by analytical approach [72], consequently no MC simulation of individual particles is performed. The output of the simulation consists of total electron numbers at various atmospheric depths together with some general information about the development of electromagnetic shower. For a few atmospheric depths the lateral electron densities are computed around the shower axis.

Other electromagnetic processes implemented in CORSIKA deal with muon interactions. With increasing energy, muons may suffer from bremsstrahlung and e^+e^- production. The importance of these processes arises above the energy of $\sim 2\ TeV$. To deal with muon's electromagnetic interactions, CORSIKA uses standard GEANT3, see [73] or [1].

2.6.4 Particle tracking

To propagate particles between two points, their space-time coordinates as well as their three-momenta have to be updated. The electron-photon propagation has been already described. In addition to mentioned processes (bremsstrahlung, etc.) the ionization energy loss for electrons has to be included. The deposited energy per radiation length X_0 is linearly dependent on the logarithm of electron energy $ln\ E$ (E in MeV)

$$dE/dx = (61.14 + 5.58\ ln\ E) \quad MeV/X_0\ . \tag{2.12}$$

The linear dependency is valid within certain energy range above which the energy loss saturates. The saturation energy, basically depends on the air pressure. Since the pressure is a function of altitude, the saturation term can be expressed as a

[6]HDPM is a phenomenological generator developed by Capdevielle [65]. The model has been inspired by the Dual Parton Model, and it is adjusted to results of $p\bar{p}$ collider experiments.

function of height h:
$(dE/dx)_{SAT} = (86.65 + 810^{-6} \times h) \quad MeV/X_0$.

The ionization energy loss for heavy charged particles is described by the Bethe-Bloch formula

$$dE/dx = \frac{\gamma^2 Z^2}{\gamma^2 - 1} 0.153(ln(\gamma^2 - 1) - \beta^2 + 9.39) \quad MeV g^{-1} cm^2 \ , \tag{2.13}$$

where γ is the Lorenz factor, $\beta = v/c$ the particle velocity and Z is the particle charge in units of e. This formula is used to calculate ionization energy loss along the particle trajectory. High energy muons suffer an additional energy loss by bremsstrahlung and e^+e^- pair production.

Charged particles are scattered predominantly by Columb field of air nuclei. In this process the direction of incoming particles is affected. However, since the target nuclei are much heavier than the scattered particles, the energy before and after the scattering is almost the same. The angular distribution of multiple scattering is described by Molière's theory or alternatively by a Gaussian function

$$P(\theta, \lambda) = \frac{1}{\sqrt{\pi \theta_S^2 \lambda}} e^{-\theta^2/\lambda\theta_s^2} \ , \tag{2.14}$$

where P is the probability density of the particle to be scattered in polar angle θ and θ_s is correlated with the mean square value of the scattering angle by $< \theta^2 >= \lambda\theta_s^2$. Length λ in Eq. 2.14 is the amount of matter traversed by the particle, i.e. it equals to $\rho \times l$, where ρ is the air density in g/cm^3 and l is the path length given in cm. The value of θ_s can be expressed in terms of m (mass of the particle), γ and β (relativistic factors) as

$$\theta_S^2 = \frac{1}{\lambda_s} (\frac{E_s}{m\gamma\beta^2})^2 \qquad (\lambda_s = 37.7 \ g/cm^2, \ E_s = 0.021 \ GeV). \tag{2.15}$$

The Gaussian approach is a very good approximation of more precise Molière's theory. Only about 2% of the events with large scattering angle occur more frequently than described by Gaussian method.

2.6.5 Magnetic field

All trajectories of charged particles are bent in the Earth magnetic field. A particle with charge Z, traveling along path length l with momentum p is deflected by the magnetic field $\vec{B}$ in the direction normal to the plane defined by vectors $\vec{B}$ and $\vec{p}$. The angle of deflection α is given by

$$\alpha = lZ \ \frac{\vec{p} \times \vec{B}}{p^2} \ . \tag{2.16}$$

In Geneva the vector $\vec{B} = (B_{north}, B_{west}, B_{upward})$[7] of the Earth magnetic field[8] is about $\vec{B} = (21.95, 0.00, 41.40)\ \mu T$.

2.6.6 Atmosphere

The atmosphere consists of N_2, O_2 and Ar with volume fractions $\sim 78\%$, $\sim 21\%$, and 1% respectively. The variation of the air density is modeled by 5 layers. In the lower four layers, the dependence of the mass overburden T on the height h is of the form

$$T(h) = a_i + b_i e^{-h/c_i}\ , \qquad i = 1, \ldots, 4 \quad . \tag{2.17}$$

In the fifth layer the mass overburden linearly decreases with height

$$T(h) = a_5 - b_5 h/c_5 \quad . \tag{2.18}$$

Atmosphere is expected to vanish ($T = 0$) at $h = 112.8\ km$. Parameters $a_i,\ b_i,\ c_i$ are selected so that the function $T(h)$ is continuous at layer boundaries. Various sets of parameters are used, e.g. the U.S. standard atmosphere (for the exact parameterization see [74]).

For nearly horizontal showers ($\theta > 75°$), the influence of the Earth curvature is no more negligible. In order to simulate these showers, the option for the spherical atmosphere is included.

[7] The component B_{north} means projection of $\vec{B}$ onto the direction to the north magnetic pole, B_{west} is the component pointing to the west. Consequently $B_{west} = 0$ by definition.

[8] Vector is given for Geneva geografic coordinates - longitude $6°1'$, latitude $46°20'$.

3 Detection of cosmic muon bundles at DELPHI

The DELPHI experiment has been installed at CERN largest collider LEP. It has been operated for almost 11 years starting from 1989. The experiment was designed for studies of e^+e^- collisions. However, cosmic events were also taken in parasitic mode to e^+e^- data. Short calibration runs without LEP beams in the accelerator registered only cosmics and these data are also studied in this thesis. In 1996 the cathode readout of hadron calorimeter (HCAL) [75, 76] was installed. This device improved granularity of the calorimeter and made possible to observe and reconstruct multi-muon events. In 1998 the cosmic trigger was established in order to improve the quality of events. When possible also the time projection chamber (TPC) was used to reconstruct multi-muon events.

3.1 Location

The experiment is located on the borders between France and Switzerland near Geneva. The apparatus is situated about 100 m underground. The surface altitude is 428 m above the sea level. The composition of the rock above the DELPHI experiment is known from geological survey performed for civil engineering purposes. The simplified picture of the overburden looks like 5 major geological layers with different mass densities. The density along the vertical line through the rock varies between 2.2 $g\ cm^{-3}$ and 2.5 $g\ cm^{-3}$ depending on the layer, Fig. 3.1 a).

The resulting energy cutoff for vertical cosmic muons is $\sim 50\ GeV$. The detector was placed in large experimental cavern equipped with three access shafts. The relative position of these shafts with respect to the DEPLHI detector is shown in Fig. 3.1 b).

3.2 DELPHI detector

The apparatus consists of Barrel (Central) part and two End-Caps on each side. The general layout of the detector is shown in Fig. 3.2.

All subdetectors in the barrel region are concentric with the beam pipe and they occupy the region between $R_{min} = 6.3\ cm$ and $R_{max} = 532.0\ cm$ in the radial direction. The magnetic field in the detector is $|\vec{B}| = 1.2\ T$. Such a high magnetic intensity is provided by superconducting coil which is made by

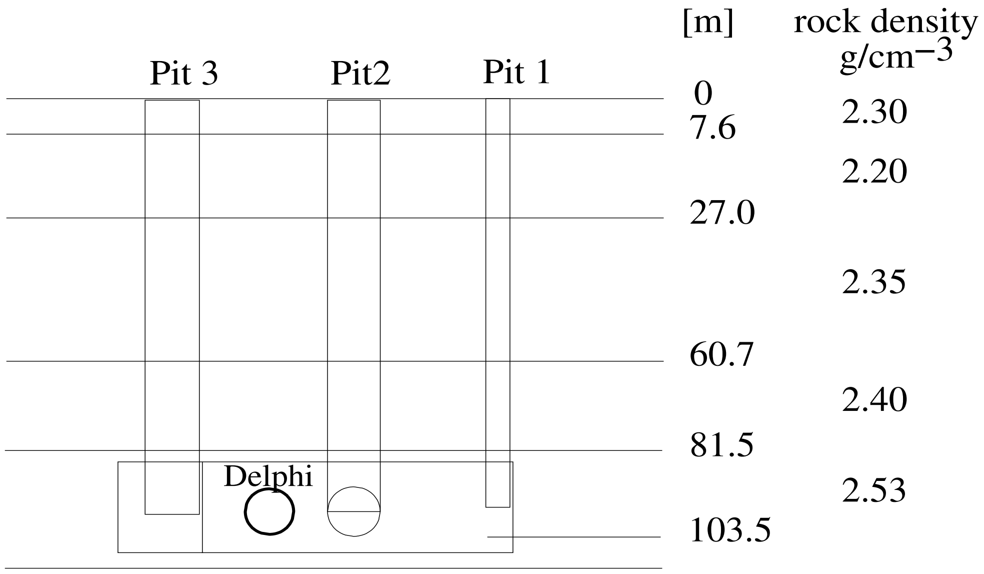

a)

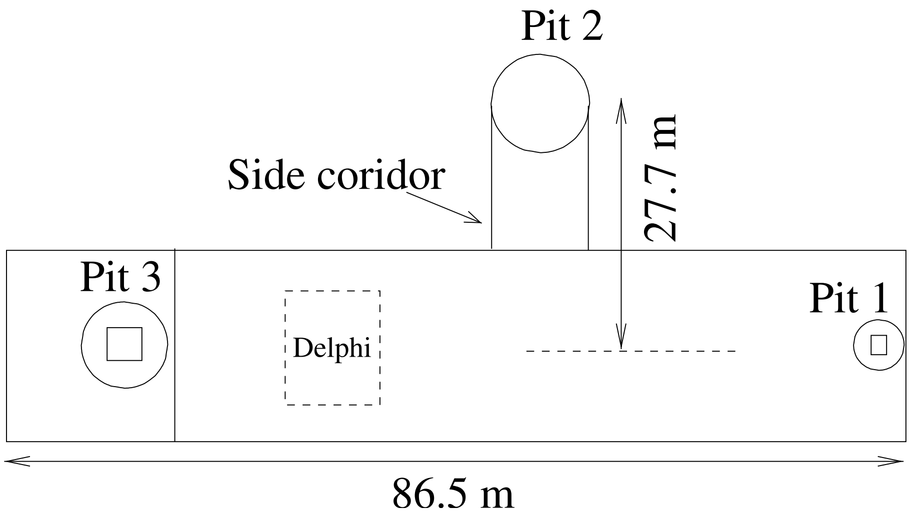

b)

Figure 3.1: The schematic geometry of the experiment location, the vertical a) and the horizontal view b).

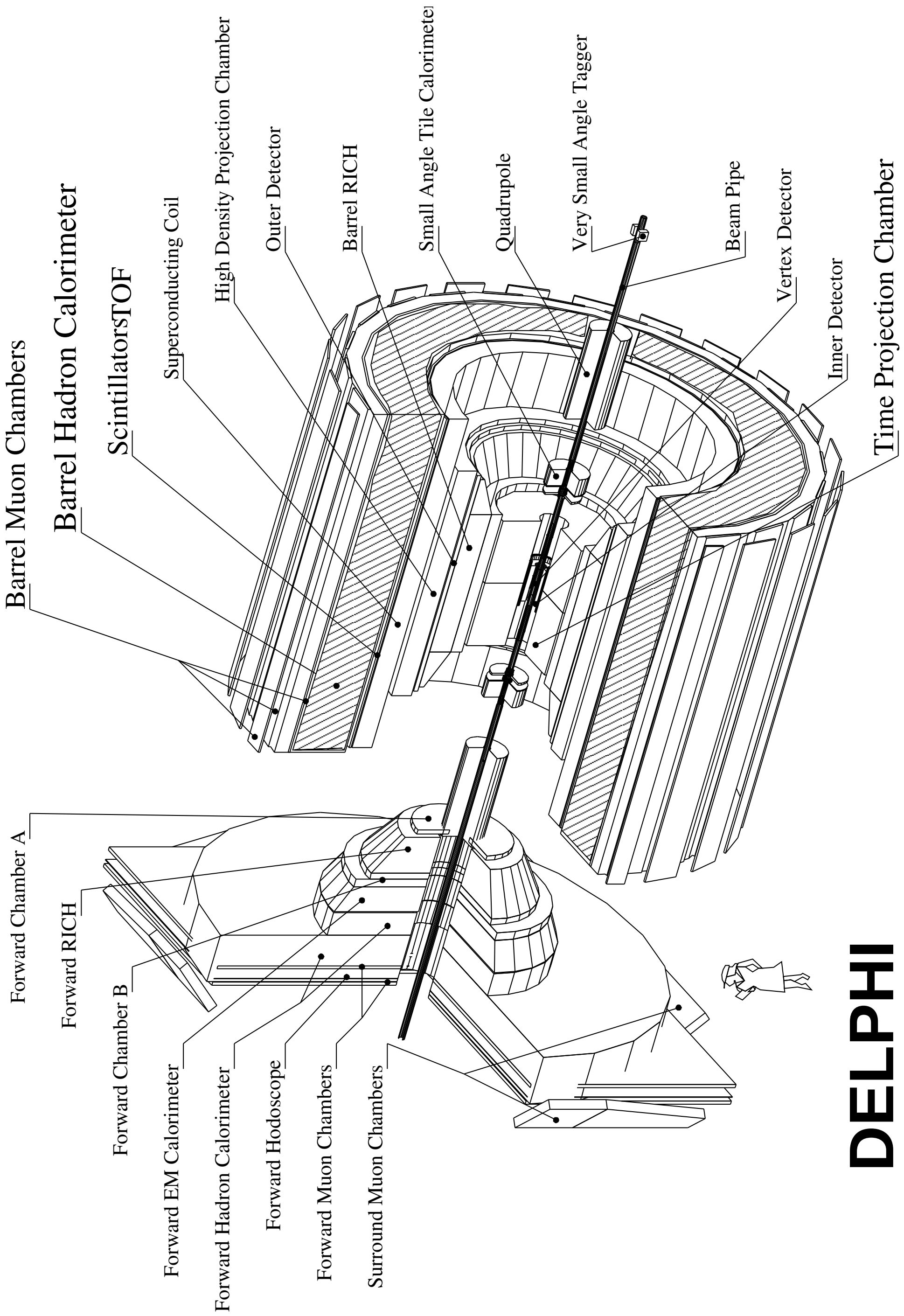

Figure 3.2: The schematic layout of the DELPHI detector. The hatched area represents the barrel part of hadron calorimeter.

single layer of $NbTi$ wires crossed by current of 6000 A. The configuration of the magnetic field (parallel to the beam axis) is assured by two compensating coils.

Brief description of subdetectors used in the analysis is given in the following text. These detectors are: hadron calorimeter, muon chambers, time projection chamber and time of flight detector. A thorough description of other DELPHI components and systems can be found in [76, 77].

If not specified Θ (ϕ) denotes polar (azimuthal) angle and R is the radial position. The definition of DELPHI reference frame can be found in Appendix A.

3.2.1 The Hadron Calorimeter (HCAL)

It is an sampling calorimeter made out of two End-Caps (Forward HCAL) and a barrel part (Barrel HCAL), Fig. 3.3. The hadronic shower develops in iron plates and the sensitive volume is gas mixture: $Ar(10\%)$, $CO^2(60\%)$, $iso{-}butane(30\%)$.

The Barrel HCAL is located between the radial positions $R_{min} = 320\ cm$ and $R_{max} = 477\ cm$. Polar angle is covered in the region $43° < \Theta_{track} < 137°$. The Barrel HCAL is divided into 24 sectors in ϕ with 20 layers radially. Each sensing layer is placed in 1.7 cm slot between two 5 cm iron plates. The detectors are limited streamer tubes with oblong cross-section $1 \times 8\ cm^2$. The length of barrel tubes is 3.5 m and they are placed in both barrel halves. Tubes consist of 8 plastic cathode cells with dimension $0.9\ cm \times 0.9\ cm$ each. The inner surface of the cells is coated with graphite varnish of low conductivity. The anode wire ($d = 80\ \mu m$ cooper-beryllium) is inserted inside each cathode cell. The limited streamer tubes are mounted on the cooper readout board. The boards are segmented into pads which pick up the streamer charges. In barrel part, 5 adjacent pads in radial direction are combined to form projective tower pointing to the intersection point. Typical tower dimension is $25 \times 25 \times 35\ cm^3$ and the angular coverage $\Delta\phi = 3.8°$ and $\Delta\Theta = 3.0°$. The charge in each tower is read out and then it is digitized in 8-bit ADC. The high voltage of 4 kV is needed to induce reasonable signal on external readout boards.

In 1996 a new system was developed to increase the granularity of the detector. Until this year only the pads were read out. The new system collects the cathode signals of individual streamer tubes and thus increases the granularity of the detector in ϕ and R by factors of 3 and 5 respectively. The signals were read out from both ends of HCAL and they were only *yes* or *no*, i.e. we cannot distinguish whether the tube was hit by one or more muons. The End-cap signals were not studied in this analysis, as the cosmic muons move along the tubes. The increased granularity allowed to reconstruct individual μ tracks and enabled us to perform the analysis of cosmic events. The reconstruction of individual tracks is performed by ECTANA package [75] and it is described in more details in Sec. 3.4.

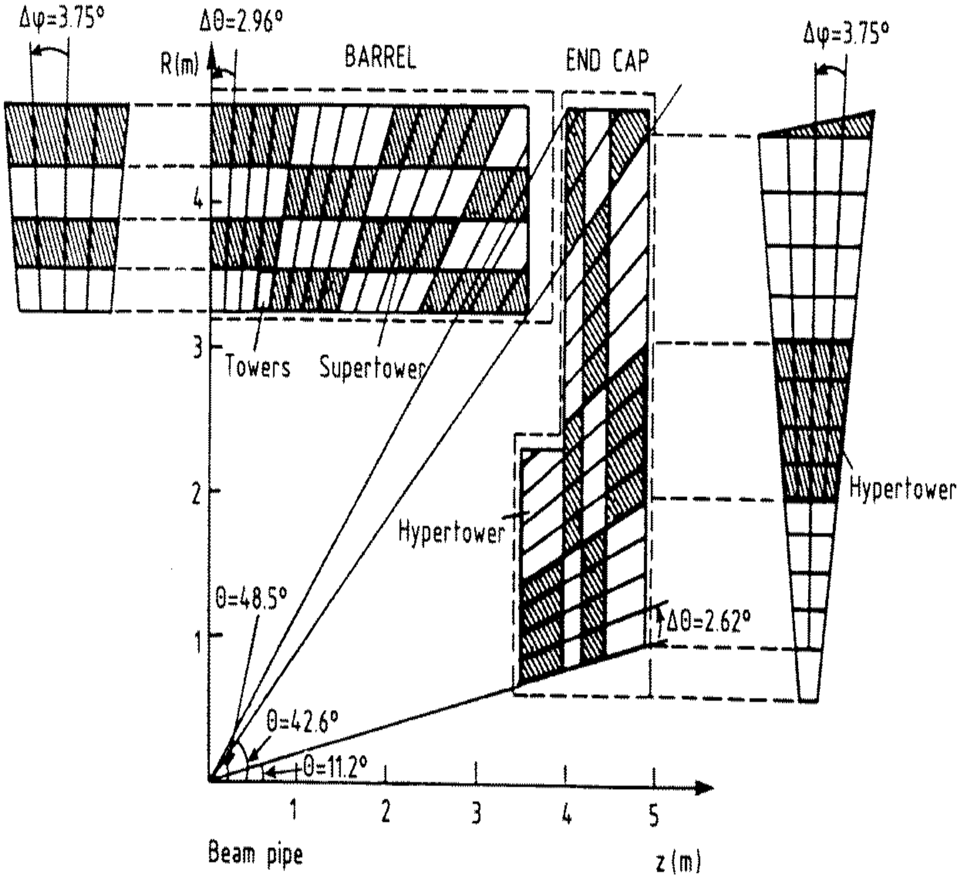

Figure 3.3: The schematic layout of hadron calorimeter.

3.2.2 The Barrel Muon Chambers (MUB)

The Barrel Muon Chambers are made of three planks of detectors parallel to the beam pipe. They are situated at different distances from the interaction point: $R_1 = 444.5\ cm$, $R_2 = 479.3\ cm$ and $R_3 = 532.0\ cm$ in the radial direction. The MUB covers the polar region $53° < \Theta^{track} < 127°$. The inner plank consists of 3 layers. The middle and the outer plank are divided into 2 layers. Each layer consists of several proportional drift chambers with total dimension $4.0 \times 83.2 \times 532.0\ cm$. The outer plank overlaps the gaps left over by the inner and the middle planks. The chamber layout is shown in Fig. 3.4.

The schematic view of one chamber is plotted in Fig. 3.5. The drift time of the ionizing electrons is measured on the anode wire and it determines the $R\phi$ coordinate. The z coordinate along the length of the chamber is given by the time difference of signals from the two ends of the delay line. The signals from one chamber form so called *time triplet*, if the anode signal and both signals from delay line are present. If one of these signals is lost then the combination is called *doublet*.

The achieved MUB precisions are $\sigma_{R\phi} = 3.0\ mm$ and $\sigma_z = 1.8\ cm$.

In this analysis MUB is used only as complementary detector to HCAL. However, chamber signals are of real importance in case of several very high multiplicity events, which cannot be reconstructed by ECTANA as will be discussed in Sec. 3.4. For these events the amount of signals from MUB detector allows us to asses lower limit of the muon multiplicity.

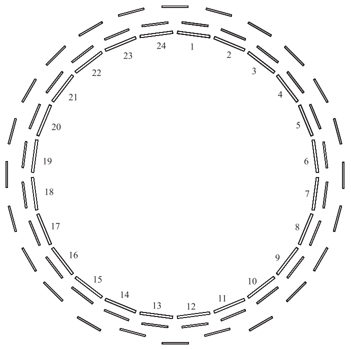

Figure 3.4: Three chamber planks at different radii in the barrel part of the detector.

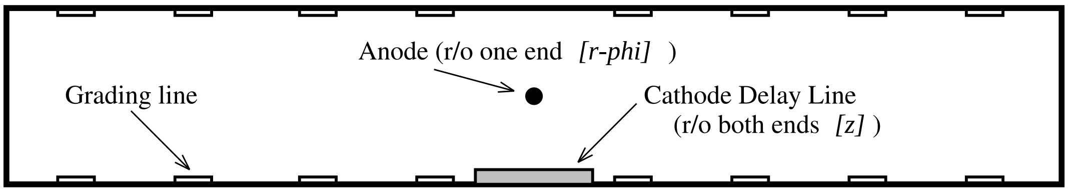

Figure 3.5: Schematic view of the muon chamber with anode, delay and grading line.

3.2.3 Time Projection chamber (TPC)

The Time Projection Chamber (TPC) fills the central barrel region of DELPHI between the radii 30 and 120 cm, Fig. 3.6. Its length along the z axis is $2\times130\ cm$. The chamber is filled with gas mixture $Ar(80\%)$ and $CH_4(20\%)$.

Charged particles crossing the TPC volume ionize the gas and free charges drift along the field lines towards the end plates. The readout is performed by Multi-Wire Proportional Chambers (MWPC) which give the $x \times y$ coordinates of corresponding point on the track segment. The third coordinate z is determined from the measured drift time and known drift velocity of free charges in the gas. The readout on each end plate was organized into six azimuthal sectors with 16 circular pad rows and 192 sensitive wires in total.

In e^+e^- data analysis, TPC was the crucial tracking detector in the DELPHI reconstruction chain. The drift time and consequently the z coordinate was calculated with respect to the starting time t_0 at the instant of beam crossing. The MWPC signals were proportional to dE/dx energy losses. Therefore, apart from the track reconstruction, TPC was partly used for particle identification.

In case of cosmic multi-muon events it was possible to run the reconstruction as well, but the drift time was calculated with respect to the average arrival time of individual muons from signals in Outer Detector (OD).

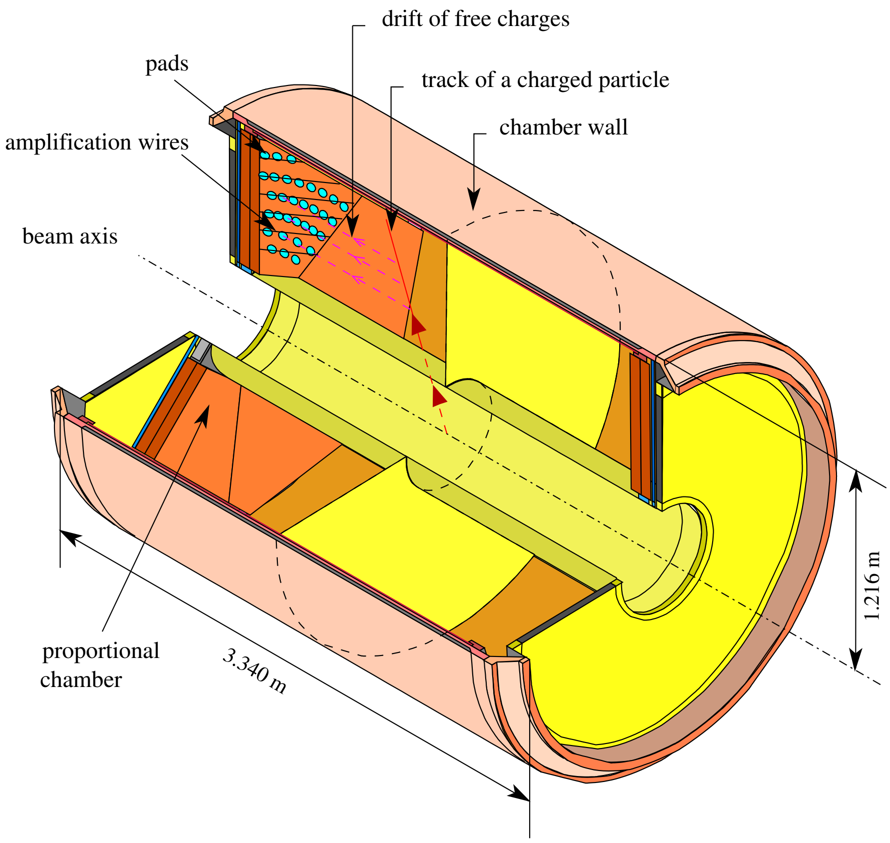

Figure 3.6: Schematic view of TPC with a track crossing its volume.

3.2.4 Outer Detector (OD)

The Outer Detector (OD) consists of drift tubes operating in limited streamer mode. The tube cross-section is $1.65 \times 1.65\ cm^2$ and length $4.7\ m$. The tubes are arranged in 5 layers and 32 columns to form so called plank. OD is composed of 24 such planks as seen from Fig. 3.7. Charged particle crossing a tube produces electrons. Signal with short raise time ($3\ ns$) is created on the wire by drifting electrons. The high voltage ($4.4\ kV$) is applied to the wire. Drift times determine the precise $R\phi$ information. In 3 inner layers of each plank also the z coordinate was estimated using time difference of the signals at both ends of the tubes.

OD is placed 2 meters from the beam axis and it was used with TPC to measure momenta of charged particles. In cosmic mode of TPC reconstruction program the time information of OD is used to estimate t_0 of the events.

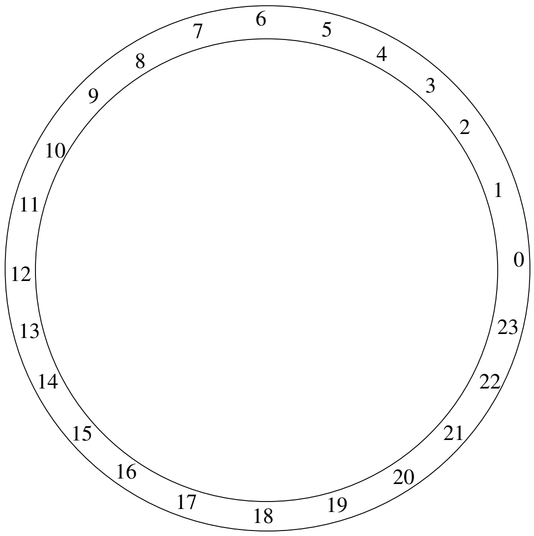

Figure 3.7: 24 planks of OD detector.

3.2.5 Time of Flight detector (TOF)

The time of Flight (TOF) detector consists of a single layer of plastic scintilator counters organized in a cylinder surrounding the magnet cryostat of DELPHI. All counters were identical (see Fig. 3.8). Each counter consists of a scintilator joined with two photomultipliers by light guide.

The TOF cylinder, Fig. 3.9, is divided in the middle into two halves with 24 detector sectors in each part. A sector covers an azimuthal angle of 15° and it consists of 4 scintilator counters.

Because of support structure some parts of azimuth remained uncovered by TOF modules. Following azimuthal regions (shown in Fig. 3.9) are not equipped by counters:

$$210^\circ < \phi < 228.8^\circ \quad , \quad 311.3^\circ < \phi < 330^\circ$$

The polar acceptance $48^\circ < \Theta < 139^\circ$ is slightly reduced in the middle of the detector ($|z| < 3\ cm$).

The TOF detector was the only DELPHI component used in DELPHI cosmic trigger. It was defined as simple coincidence of 3 TOF sectors.

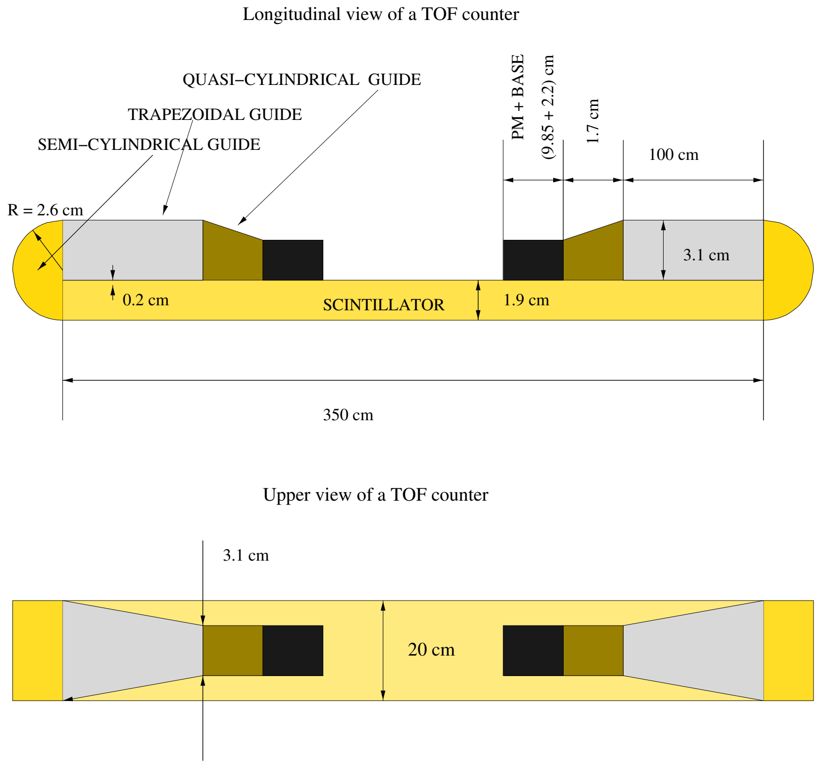

Figure 3.8: Schematic view of TOF counter design.

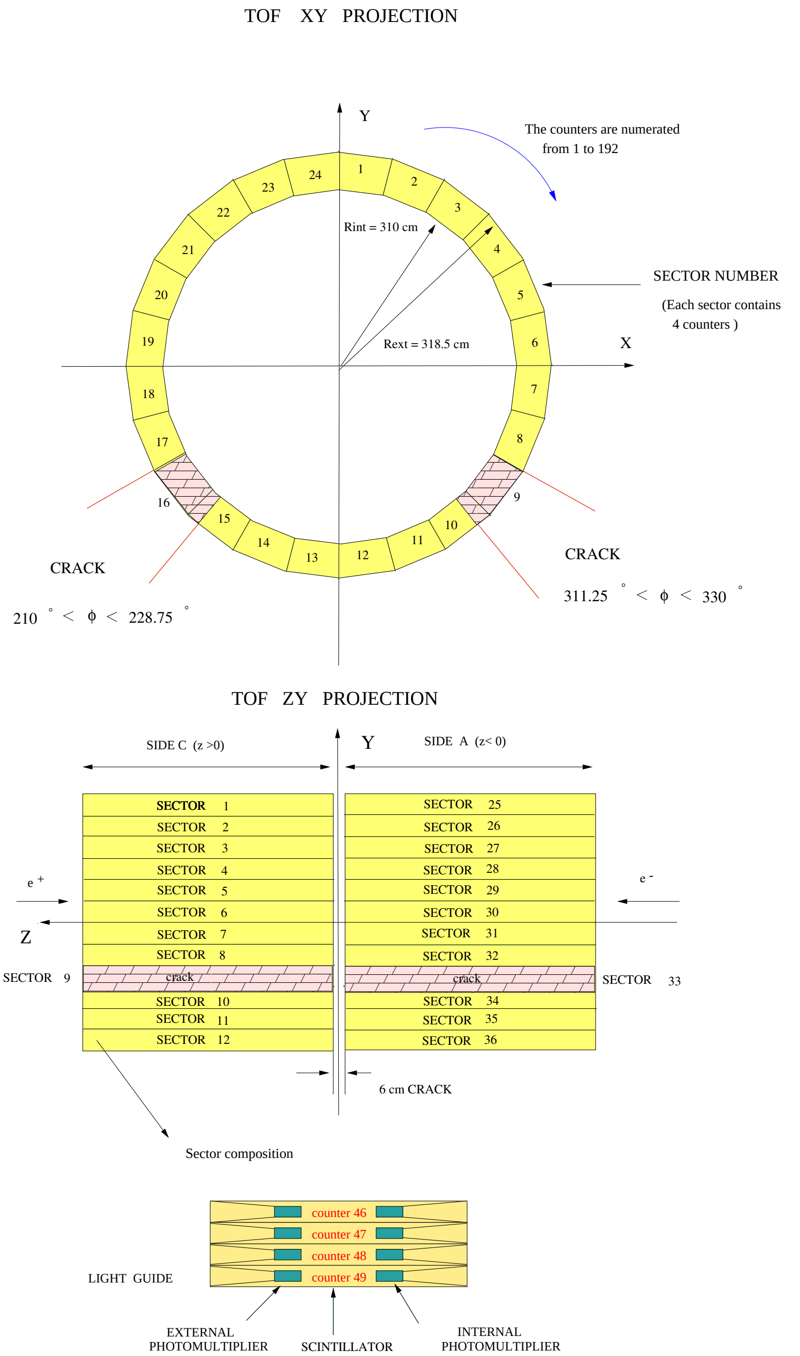

Figure 3.9: Arrangement of scintilator counters and detector sectors in the TOF detector.

3.3 Trigger

The Delphi trigger system is organized in 4 different levels T1, T2, T3 and T4. First two levels of the trigger system (i.e. T1 and T2) are synchronous with the Beam Cross Over (BCO) signal.

The T1 trigger used the information coming from the tracking detectors, scintilators in TOF, forward electromagnetic calorimeter and MUB. The T2 inputs are signals from TOF, TPC, electromagnetic and hadron calorimeter, forward muon chambers, etc. For cosmic stream T1 and T2 triggers were the same and both required 3 active TOF sectors.

The T3 and T4 triggers run asynchronously with respect to BCO. Both are software filters. T3 trigger uses the same selection logic as T2 trigger but more detailed detector information is included. It reduces the background passing through the T2 trigger by a factor of 2. T4 trigger was implemented to reduce about half of the background still remained after T3. The detailed trigger description is presented in [76, 77, 78].

3.4 Event reconstruction

Reconstruction of cosmic events is based on data from from two DELPHI subdetectors, HCAL and TPC. The chain of original DELPHI reconstruction programs was not designed for cosmic events. Consequently the reconstruction is performed in different way compared to e^+e^- analysis.

The track reconstruction from hadron calorimeter requires ECTANA package [75] which was developed to analyze cathode readout of HCAL. ECTANA code allows to reconstruct cosmic events directly from DELPHI raw data files without any previous processing or input from other subdetectors.

The TPC reconstruction is possible with DELPHI standard tool DELANA [79] using TPC package TPCANA, however running in special mode designed for cosmic data.

3.4.1 ECTANA program

The track reconstruction in hadron calorimeter is performed by ECTANA program, which scans signals in barrel modules of HCAL and finds track patterns of hit streamer tubes. This package has advantage that it was developed not only for studies of e^+e^- collisions, i.e. tracks coming from the interaction point in the middle of the detector, but it has the option for the cosmic events as well. When running in cosmic mode it allows to reconstruct tracks originating anywhere in the calorimeter without explicit cut on the track impact parameter. This is the unique feature of the program, because most of other reconstruction programs at DELPHI were generally developed for e^+e^- events only.

The search for active streamer tubes starts from the outer planes of a given module and continues inwards. A group of at least 4 aligned hits is taken as the track element. The track element is also required to have reasonable density of hits, at least 30% of tubes along the track element have to be active. Furthermore the length of the track has to be larger than 50 cm. All possible hypotheses starting from a certain hit found during the scan are analyzed, positions of hits are fitted by a line. The best fit in terms of the number of hits and χ^2 is stored. Before storing the similarity with other hypotheses is checked to avoid double counting. It is furthermore possible to merge pairs of track elements, which intersect inside the calorimeter, by a circle and measure the $x \times y$ projection of the track momentum. However, this option has not been used, because only a few muon tracks are reasonably curved inside the calorimeter and the errors of measured particle momenta are large.

An example of ECTANA reconstructed event with muon multiplicity ~ 120 is shown in Fig. 3.10. Most of the tracks are nicely parallel within $\pm 2°$. The event presented in Fig. 3.10 is one of highest multiplicity events in data.

3.5 Detector simulation

The standard tool for detector simulation at DELPHI is DELSIM package [80]. This is the full detector simulation program, as it includes simulation of all components of the DELPHI subdetectors. Special interface between CORSIKA and DELSIM is used in order to simulate cosmic events. This is done by modification of the DELSIM code of muon generator which was originally used for cosmic background simulation.

To generate significant number of events DELSIM often needs several days of CPU-time on the fastest workstations.

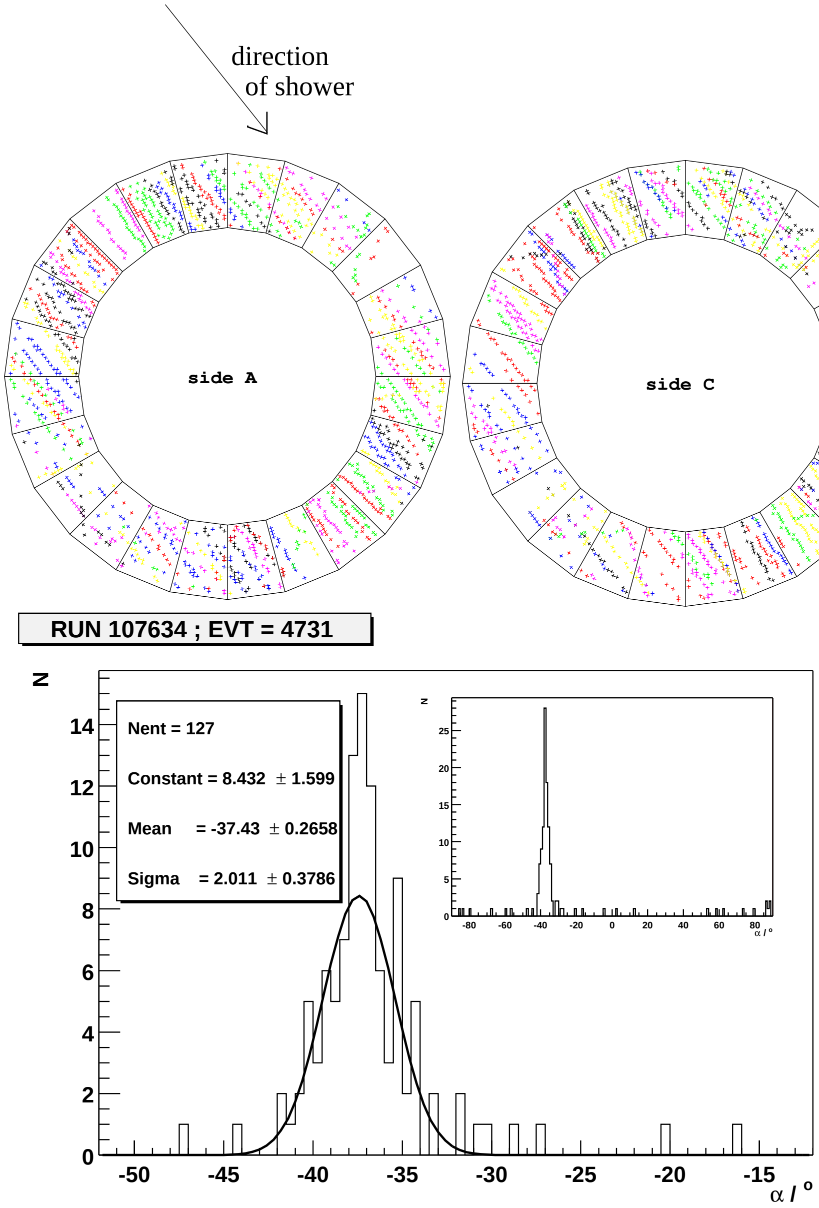

Figure 3.10: Example of cosmic event as seen by HCAL cathode readout. Different tracks are represented by different colors. The lower part of the picture shows the distribution of projected angle measured in HCAL plane.

4 DELPHI data

4.1 Data selection and trigger

To detect the cosmic events, DELPHI cosmic trigger (DCT) has been implemented to the DELPHI trigger system. It requires 3 active time of flight (TOF) detector sectors (TOF MJ3) to trigger the event. The TOF counters are ready to trigger the event within 4 μs starting from the moment of beam crossing. The beam crossing frequency depends on the number of e^+e^- bunches in the machine. When running with 4 bunches in the machine, the beam crossing period is 22.23 μs, while in the 8 bunch mode it is the half of that value, i.e. 11.12 μs. Consequently, the detector is open to trigger cosmic events in $100 \times 4/22.23 = 18\%$ of the total data taking time in 4 bunch mode and 36% in 8 bunch mode respectively. The dedicated cosmic runs (without the beams in the collider) have been performed mainly at the beginning of each year. Although there were no e^+e^- collisions, the beam crossing signals (BCOs) were simulated in such a way, that the detector was in fact running in 8 bunch mode.

The cosmic trigger has been implemented in the autumn 1998 and it was running in stable mode in the years 1999 and 2000. However, the trigger was not active permanently. Tab. 4.1 shows 14 main types of trigger conditions during 1999 and 2000. Each trigger type corresponds to different trigger function. DCT was not implemented in 1999 at beginning of the data taking year (marked by *). Additional problems occurred in cosmic runs during 1999, when the beam crossing frequency was not simulated properly. In these cosmic runs it was finally not clear what is the total live time. Moreover DCT was not active in 2000 for runs marked by (**).

Fig. 4.1 plots the rate of events with more than 4 muons ($N_\mu > 4$) in different run periods with different trigger configurations. The event rates are consistent within their statistical errors for all the periods when DCT was working correctly and permanently. The dependence of event rates on the particular period is the result of the DCT presence (or non-presence) in the trigger setting. Thus only the runs with DCT correctly running were used for further analysis. The total time of selected trigger/run periods is 8.66 10^6 s. When corrected to the effect of beam crossings and 4 μs detection window, the total effective live time is $T_{eff} = 1.55\ 10^6\ s$.

In the ideal case, when a TOF sector fires every time the muon passes through it and assuming a noise free detector, at least two muons are needed to activate the trigger. In the reality the detector is noisy, hence time to time only one muon

I	PY1/PY2	N_{RUN}	t/s	year	run type	comment
1	6/5	136	$1.03\ 10^6$	1999	C	*
2	5/5	409	$1.64\ 10^6$	1999	P	*
3	10/5	52	$0.15\ 10^6$	1999	P	*
4	18/6	511	$1.97\ 10^6$	1999	P	
5	19/11	36	$0.14\ 10^6$	1999	P	
6	20/6	11	$0.13\ 10^6$	2000	C	
7	21/6	127	$2.27\ 10^6$	2000	C	
8	18/6	68	$0.34\ 10^6$	2000	P	
9	23/17	57	$0.23\ 10^6$	2000	P	
10	25/18	364	$1.13\ 10^6$	2000	P	**
11	31/19	319	$1.04\ 10^6$	2000	P	
12	33/19	371	$1.11\ 10^6$	2000	P	
13	33/20	530	$1.43\ 10^6$	2000	P	
14	34/20	397	$1.26\ 10^6$	2000	P	**

Table 4.1: Trigger settings (run periods) with live times larger then 10^5 s. I is the trigger label. Numbers in *PY1/PY2* column represents the DELPHI internal labels for the trigger configuration in two trigger levels 1/2. Time t is the total time of corresponding N_{RUN} runs. Label C means that the run type is dedicated cosmics and P is the ordinary physical run. Comments (*) and (**) are explained in the text.

passing through the apparatus can cause the trigger. The detection efficiency is, of course not 100% and it is an increasing function of the track length in TOF counters, i.e. it depends on the muon incoming angle and position. Consequently, the trigger efficiency at very low muon multiplicities depends on many factors and it changes during time, because the conditions change. However, if we increase the multiplicity we ensure that at least a fraction of muons in an event activates the trigger. Therefore at higher multiplicities the trigger is almost 100% efficient.

The influence of increasing multiplicity on the event rate can be demonstrated using data from different run periods. As an example two run periods (index 4 and 7 in Tab. 4.1) are compared with the run period 12 (reference). Let us define the quantity R as:

$$R = \frac{N(TEST \mid N_\mu).T_{REF}}{N(REF \mid N_\mu).T_{TEST}},$$

where $N(TEST/REF \mid N_\mu)$ is the number of events with muon multiplicity N_μ during studied respectively reference run period and $T_{TEST/REF}$ is the total run time of the corresponding period. R should be essentially 1 for perfect agreement between tested and reference data. Fig. 4.2 plots the quantity R as function of muon multiplicity N_{μ}, which is required for the events to be counted.

Staring from multiplicity 4 the agreement is obtained within the statistical errors in the run period 7. For the run period 4 the agreement is even at smaller multiplicities. Similar conclusions can be obtained in all selected run periods. The reasonable minimal multiplicity at which the event rates are consistent with each other is 4. At lower multiplicities the trigger fluctuates according to actual TOF state.

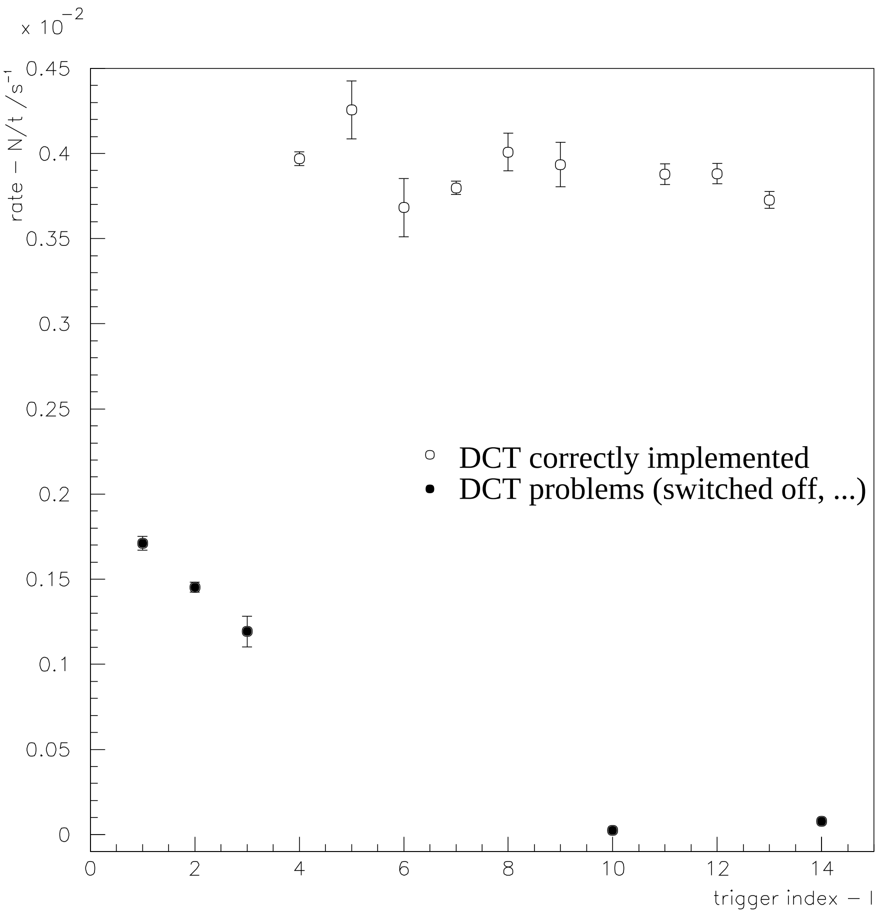

Figure 4.1: Event rates with more than 4 muons reconstructed in HCAL ($N_{\mu} > 4$) at different trigger settings.

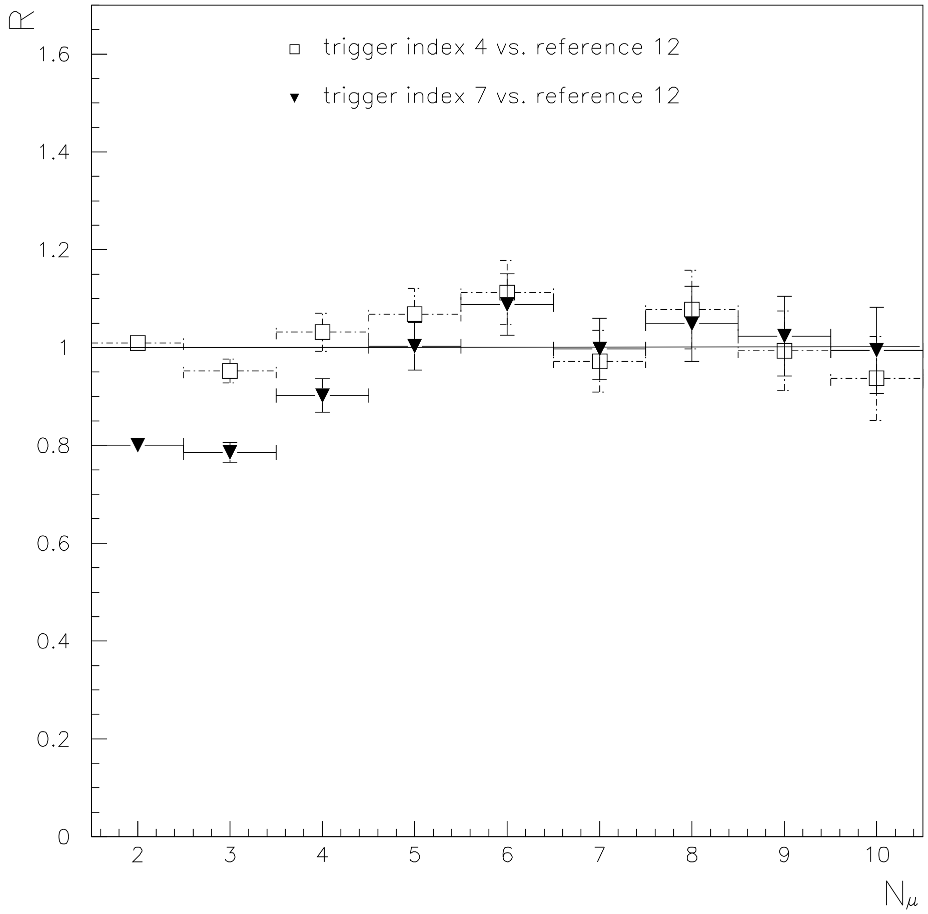

Figure 4.2: Dependence of the quantity R defined in the text on the muon multiplicity N_μ. Only the events that are triggered by DCT are taken into account. The fraction of DCT triggered events to the total number of events is above 99% for multiplicity 4 and higher.

4.2 Muon multiplicities

The selected data sample consists of 54201 events with muon multiplicities higher than 3 ($N_\mu > 3$). The number of events with at least 30 muons in the apparatus is 1065 as seen from Tab. 4.2.

The scanning of all events with $N_\mu \geq 30$ has been performed in order to check them and ensure the rejection of electro-magnetic showers originating from muon interactions in the cavern ceiling or detector material. We found 14 shower like events corresponding to 1.3% of 1065 scanned events. The parallelism of reconstructed tracks was checked also by the cut that requires more than 50% of reconstructed tracks to be within 5° from the mean value of all track angles in

	number of events
$N_\mu > 3$	54201
$N_\mu \geq 6$	26303
$N_\mu \geq 30$	1065
$N_\mu \geq 70$	78
$N_\mu \geq 100$	24

Table 4.2: Event statistics in selected data sample.

the event. The cut rejected the same events as the scanning.

The multiplicity distribution measured in HCAL from selected runs is plotted in Fig. 4.4. In addition to reconstructed events another 7 events with almost all HCAL tubes active have been detected. These events are proven to have cosmic origin because vacancies in almost saturated HCAL can be fitted by parallel lines. An example of saturated event is shown in Fig. 4.3.

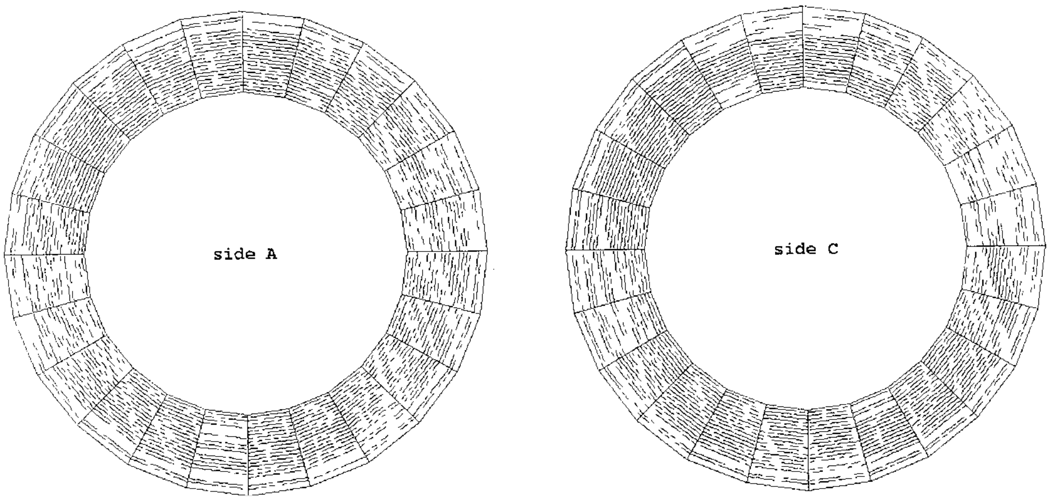

Figure 4.3: Example of saturated event. Parallel "tracks" can be reconstructed from vacancies in almost full HCAL.

We have tried to use additional information from muon chambers in order to find approximative estimate of the muon multiplicity from number of anode hits. In case of cosmic events the muon chambers do not provide information on event by event basis because their effective readout after BCO is active for shorter time compared to HCAL and TOF. As a result only 2 out of these 7 saturated events have full information from muon chambers. Even if the track reconstruction in muon chambers is not available for the multi-muon bundles the approximative estimation of multiplicity is done according to the total number of anode hits. Sample of events with information from both HCAL and muon chambers has been studied in order to find the correspondence between the HCAL multiplicity and the number of MUB anode hits. Results are plotted in Fig. 4.5. It seams reasonable to expect that these two events have multiplicity about 150 or higher should it be possible to reconstruct them. Remaining 5 saturated events are just expected to have multiplicity higher than the highest multiplicity reconstructed from unsaturated HCAL events ($N_\mu > 127$).

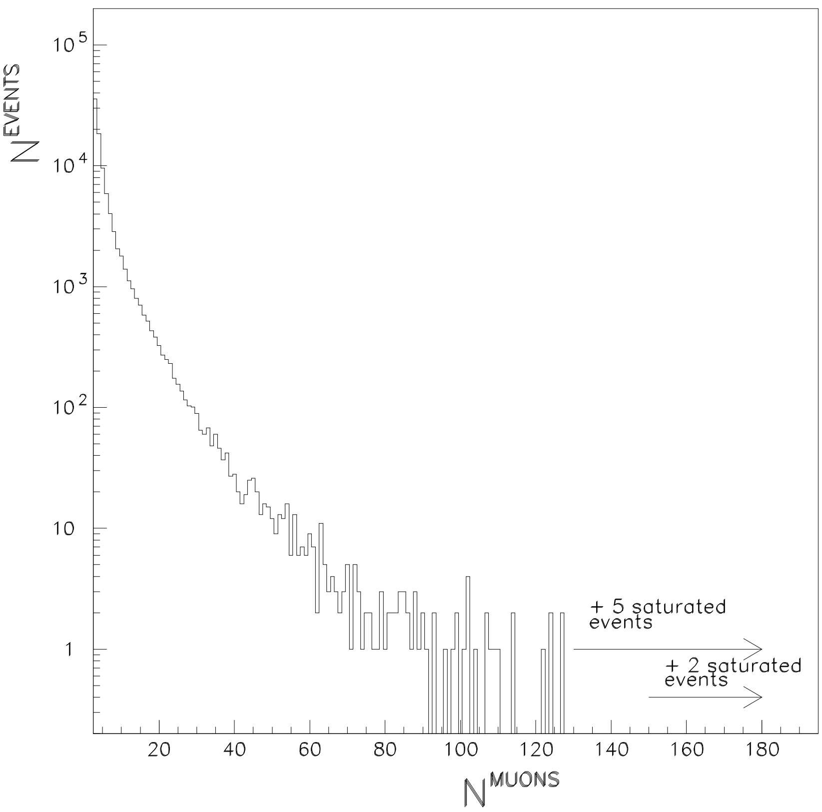

Figure 4.4: Distribution of muon multiplicity measured in HCAL from selected runs.

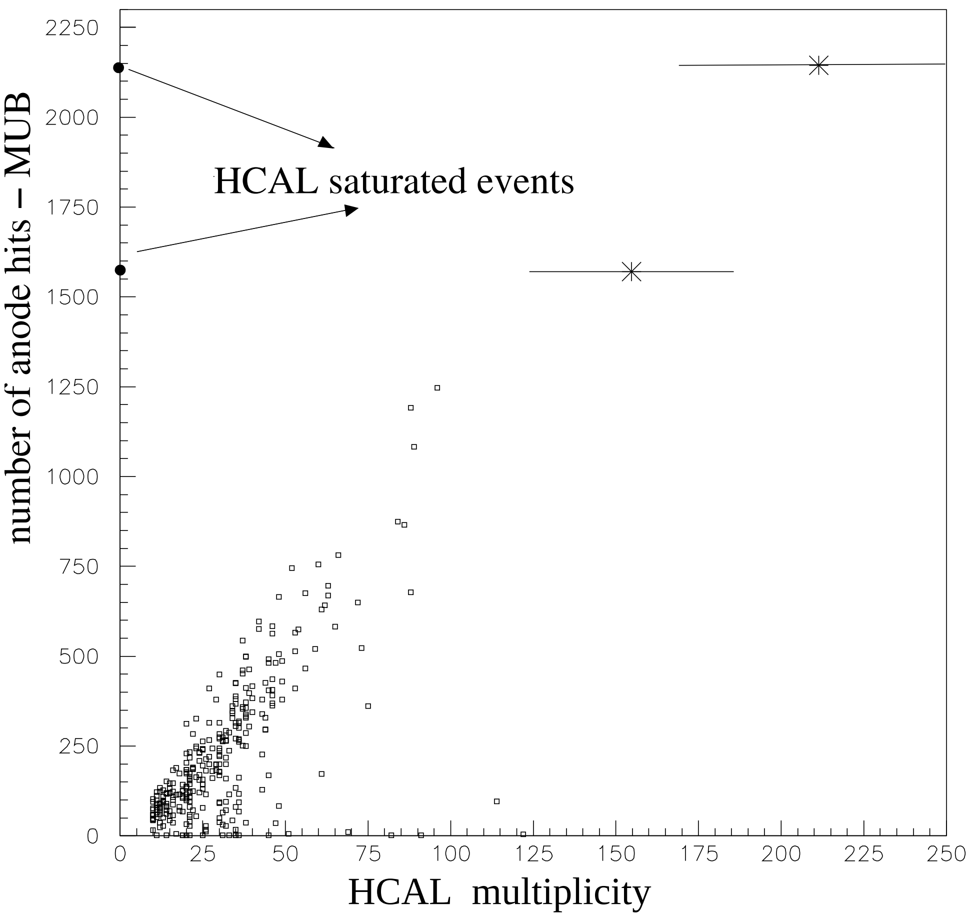

Figure 4.5: Correlation between the HCAL multiplicity and the number of anode hits in muon chambers

4.3 Projected angle

The distribution of reconstructed shower angles in *(x,y)* HCAL projection plane (see Appendix A) is plotted in Fig. 4.6 for all events with more than 3 reconstructed muons.

Authors of the work [81] found the $\cos^n \theta$ ($n = 3.32$) dependence of the zenith angle distribution. In order to compare this result with our measurement a simple Monte Carlo calculation was performed. About 100000 tracks were generated so that they fulfill the mentioned zenith angle distribution. A track was represented by a simple line pointed to the middle of the detector. For each track the projection onto the plane of HCAL was calculated and the angle stored. The result is plotted in Fig. 4.6 with dashed line. DELPHI data and data [81] agree reasonably and give similar distribution of projected angle.

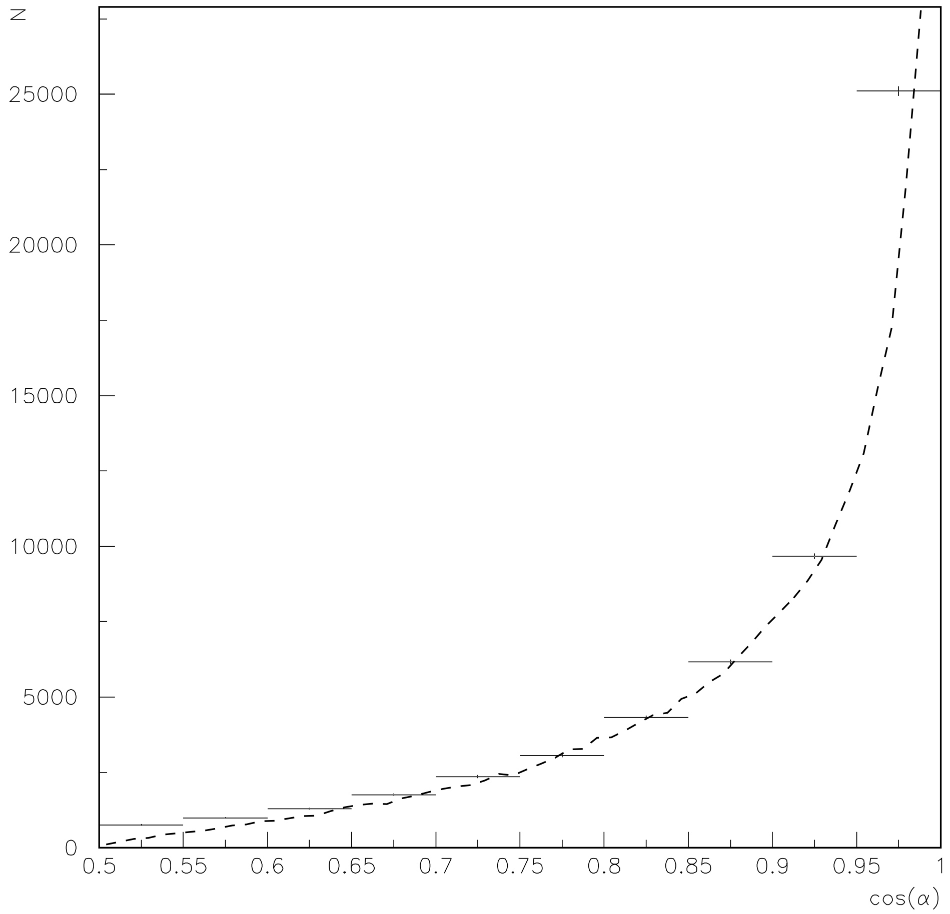

Figure 4.6: Distribution of $cos\ \alpha$, α is measured in the HCAL projection with respect to the vertical direction. Events with $N_\mu > 3$ contribute to the histogram. The dashed line corresponds to the distribution of $\cos\theta$ (θ is the zenith angle) in the form $\sim (\cos\theta)^{3.32}$. This dependence was observed in [81].

4.4 Day time dependence

Should the cosmic events originate mostly from the Sun, the event rate would depend on the day time, i.e. it should be strongly suppressed during nights. In fact, this is not expected.

The energy of primary particle which is high enough to produce a multi-muon event has to be higher than $\sim 10^{14}\ eV$. Only at these energies several muons in an event can pass through 100 m of rock. The energy $10^{14}\ eV$ falls already in the energy interval of presumed galactic cosmic rays. DELPHI multi-muon events originate from the Galaxy and not from the Sun. Hence the event rate should be stable during the day time.

The time dependence of event rates plotted in Fig. 4.7 fulfills this expectation.

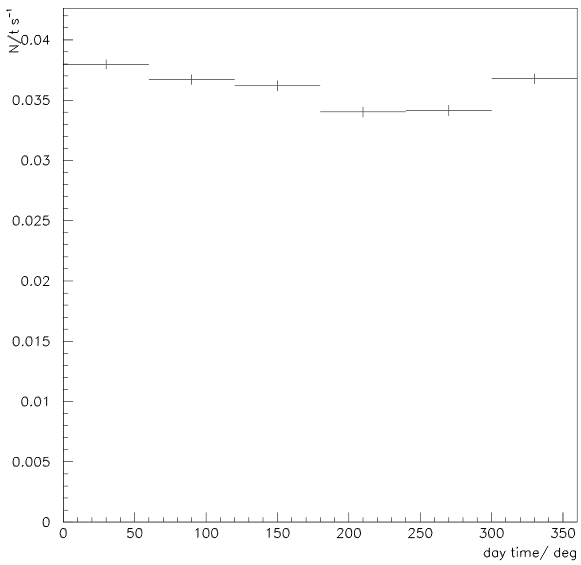

Figure 4.7: The event rate versus the solar time expressed in degrees. Events with more than 3 reconstructed muons are taken into account.

4.5 Sidereal time dependence

The sidereal time is defined with respect to distant stars. One sidereal day lasts from the moment when a distant star crosses the meridian until its next passage over the meridian. Since the Earth moves in its orbit around the Sun, the sidereal day is by about 4 *min* shorter than the solar one. The effect is demonstrated in Fig. 4.8.

In order to calculate sidereal time for each individual event with reasonable precision more exact algorithm is chosen. This algorithm takes into account various corrections such as the real elliptical shape of the Earth orbit and it ensures 5 μs precision in the final calculation.

Should the cosmic events originate from one or a few cosmic ray sources, the event rate would be amplified or suppressed according to the source position with respect to horizon.

Fig. 4.9 shows no event rate modulation during the sidereal day in agreement with the idea of isotropic distribution of cosmic ray sources in the Galaxy.

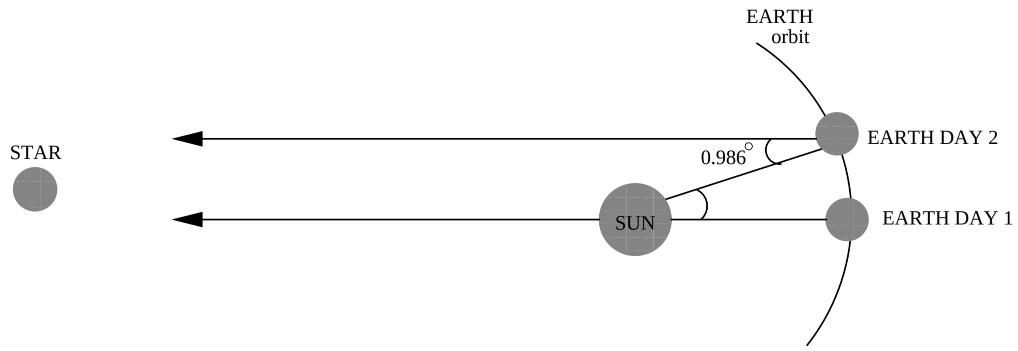

Figure 4.8: The effect of Earth movement around the Sun shortens the sidereal day with respect to solar day.

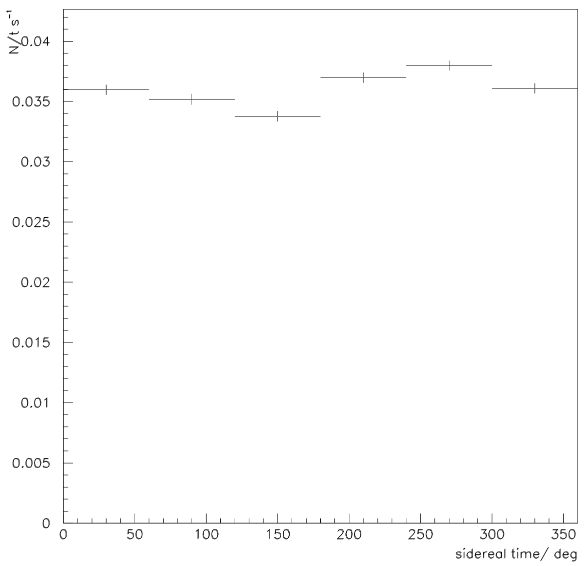

Figure 4.9: The event rate versus the sidereal time expressed in degrees. Events with more than 3 reconstructed muons are taken into account.

4.6 TPC multiplicity

The distribution of muon multiplicities as measured by TPC is plotted in Fig. 4.10. The events correspond to high multiplicity events with the number of muons $N_\mu > 15$ reconstructed from calorimeter.

In order to reconstruct muon tracks from HCAL by ECTANA, only the raw data of event records are needed. In case of TPC, DELANA subroutines need to read also run headers in order to get all relevant information about TPC status.

During the procedure of archiving DELPHI cosmic data tapes into more modern robotic machine, some particular runs had not been copied correctly. While all event records were stored separately in PC disks, some run headers were lost. This offline effect leads to reduction of data taking time when dealing with TPC data from 1.6 $10^6 s$ in HCAL to 1.2 $10^6 s$ in case of TPC. Due to this reason the total number of events in Fig. 4.10 does not match the number of events with $N_\mu > 15$ in the calorimeter.

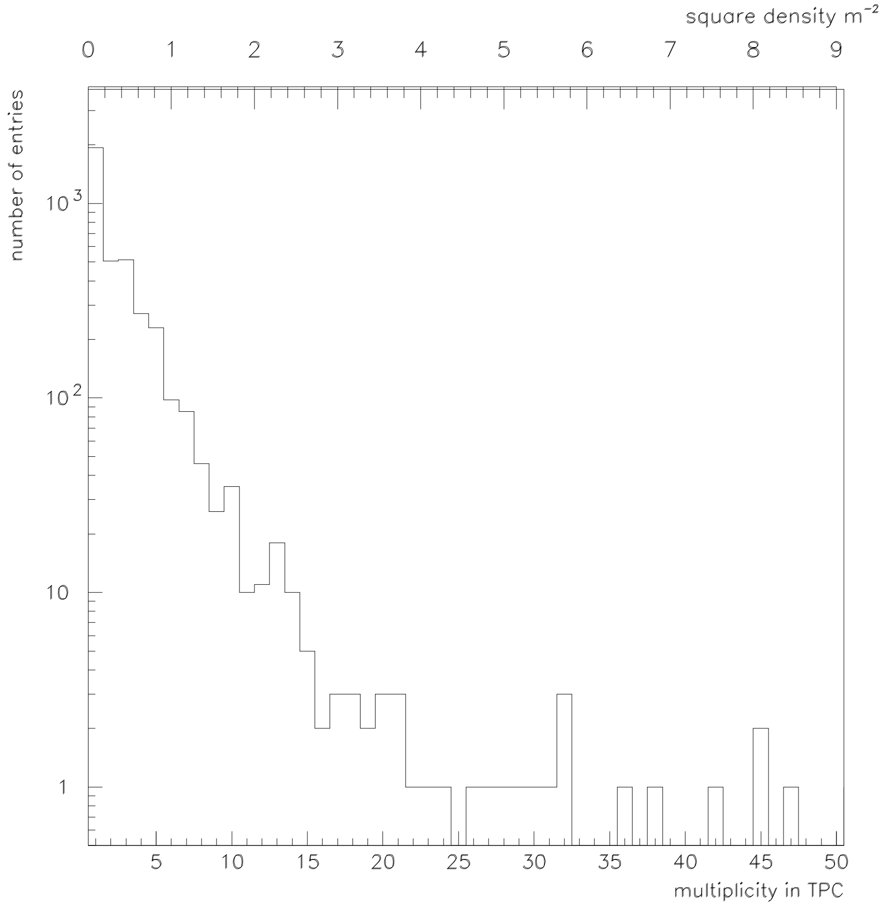

Figure 4.10: The TPC multiplicity of events with more than 15 muons reconstructed in HCAL.

4.7 Sky plot

In TPC all the spatial information is reconstructed and it allows us to search for possible sky sources of largest events. The sky plot as seen by TPC for reconstructed events with more than 15 tracks in HCAL and more than 3 tracks in TPC is presented in Fig. 4.11.

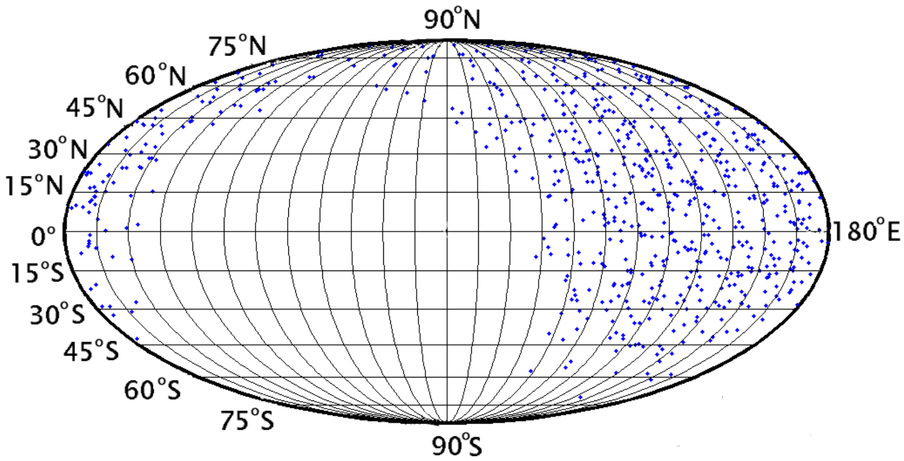

Figure 4.11: The sky plot of events with more than 15 tracks in HCAL and more than 3 reconstructed tracks in TPC. No clear event clustering is apparent.

5 Simulation

The aim of the MC simulation is to find out expected multiplicity distributions so that they can be compared with the measurement. To fulfil this aim it is clear that we have to assume certain flux and composition of primary particles. While the flux is relatively known in corresponding energy range, the composition is still subject of intensive research and no final conclusion has been drawn yet.

Since the chemical composition is still unknown, only two extremal cases of hadron primary particles are investigated in this work - p and Fe. This is based on the natural assumption that the primary flux is composed from nuclei with mass between that of p and Fe. Proton is simply the lightest nucleus. Iron is the heaviest and most stable nucleus that can be created by nuclear fusion processes in stars and it survives long time in the interstellar space.

Taking into account this assumption, it is clear that multiplicity distribution should be between these two extremal predictions of proton and iron primary particles. On the other hand, if both p and Fe predictions underestimate or overestimate data, then it could be a signature that the underlying model of nucleus-nucleus interactions is not able to describe the shower properties in this particular aspect.

The procedure of applying two extremal assumptions (p and Fe) on the primary particle mass is frequently used in various model tests of dedicated cosmic ray experiments (e.g. see the above-mentioned work [68]) .

5.1 Interaction models

CORSIKA (*ver. 6.014* from March 2002) simulation package was used in the presented analysis to describe evolution of atmospheric showers. Various interaction models describing primary interactions can be employed within CORSIKA. These models are tuned to available accelerator data and their validity is tested also using cosmic ray data. For this reason the model predictions as well as settings of internal model parameters change in time. This is demonstrated in Fig. 5.1, where proton-air inelastic cross-sections are plotted as a function of proton momentum. The two pictures demonstrate the situation in years 1998 and 2000. It is evident that agreement between models increases, however in the year 2000 the discrepancy between models is still about 10% at 10^6 GeV and about 25% at 10^9 GeV.

The models are compared in Fig. 5.2 in terms of average charge multiplicity in p-N^{14} collisions. It is evident from the plot, that QGSJET01 predicts on average larger numbers of charged particles with respect to other models.

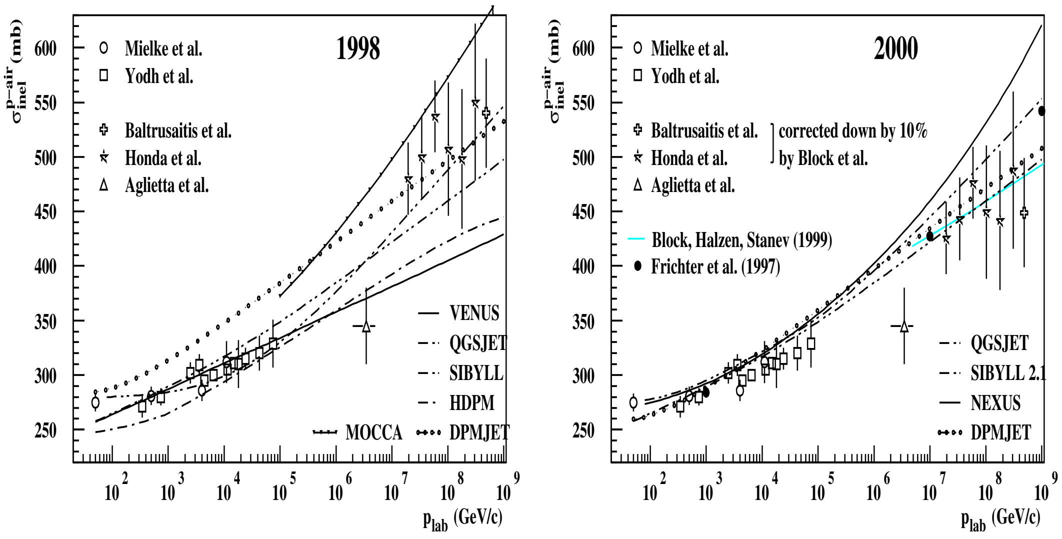

Figure 5.1: The proton-air inelastic cross-section measured by various experiments and the predictions of different models. Two graphs, from [46], compare the situations in 1998 and 2000 respectively.

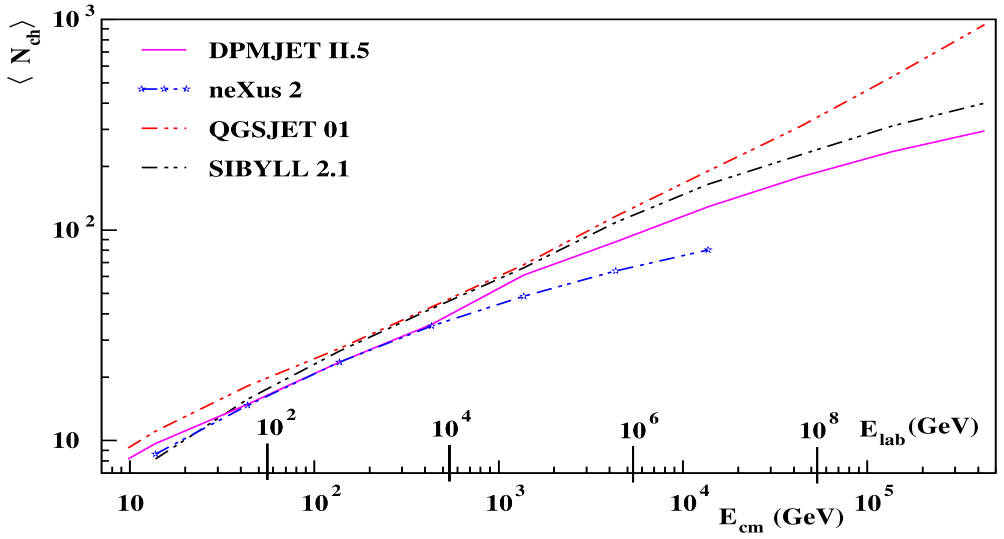

Figure 5.2: The average charged multiplicity in $p - N^{14}$ collisions as a function of the center of mass energy for different models. Picture is taken from [82]. The proton energy in N^{14} rest frame is given above the horizontal axis.

As mentioned previously QGSJET is preferred in the community of astroparticle physicists. It was shown that this model describes best the correlations between different shower components, (see e.g. work [68]).

From the point of view of underground muons three models (QGSJET, DPMJET, SIBYLL) are compared in Fig. 5.3 and 5.4 in terms of muon Lateral Distribution Functions (LDF). These plots were obtained for vertical showers and represent mean muon densities as a function of distance from shower core. To simulate the situation 100 m underground, only muons with momentum $p > 50\ GeV$ are taken into account. It shows that QGSJET predicts larger muon densities than other selected models especially at distances close to shower core $R < 40\ m$.

5.2 Simulation chain

In order to be able to simulate the cosmic ray induced showers in the DELPHI environment, a chain of simulation programs has been set up. The interaction model (QGSJET) is used within the CORSIKA simulation package. The transport of particles through the rock is simulated using GEANT3 [73]. The detector response is simulated via full simulation of DELPHI in DELSIM program [80]. The muon tracks inside HCAL are then reconstructed using ECTANA package [75].

5.2.1 CORSIKA

Data sets were simulated for protons and iron nuclei as primary particles in 10 energy ranges as seen in Tab. 5.1. It turned out that the two intervals $10^{17} - 3\ 10^{17}\ eV$ and $3\ 10^{17} - 1\ 10^{18}\ eV$ almost do not contribute to the observed multiplicity spectrum due to small flux of primary particles at these energies and too short observation time. The energies smaller than $3\ 10^{13}\ eV$ are also not relevant for the final result because the muon energy cut-off ($50\ GeV$) does not allow us to observe significant number of multi-muon events generated in these energy intervals.

E	number of events	E	number of events
$10^{13} - 3\ 10^{13}\ eV$	100000	$3\ 10^{15} - 10^{16}\ eV$	6000
$3\ 10^{13} - 10^{14}\ eV$	100000	$10^{16} - 3\ 10^{16}\ eV$	1000
$10^{14} - 3\ 10^{14}\ eV$	100000	$3\ 10^{16} - 10^{17}\ eV$	600
$3\ 10^{14} - 10^{15}\ eV$	10000	$10^{16} - 3\ 10^{17}\ eV$	100
$10^{15} - 3\ 10^{15}\ eV$	10000	$3\ 10^{17} - 10^{18}\ eV$	100

Table 5.1: Energies of input primary particles and the number of simulated events.

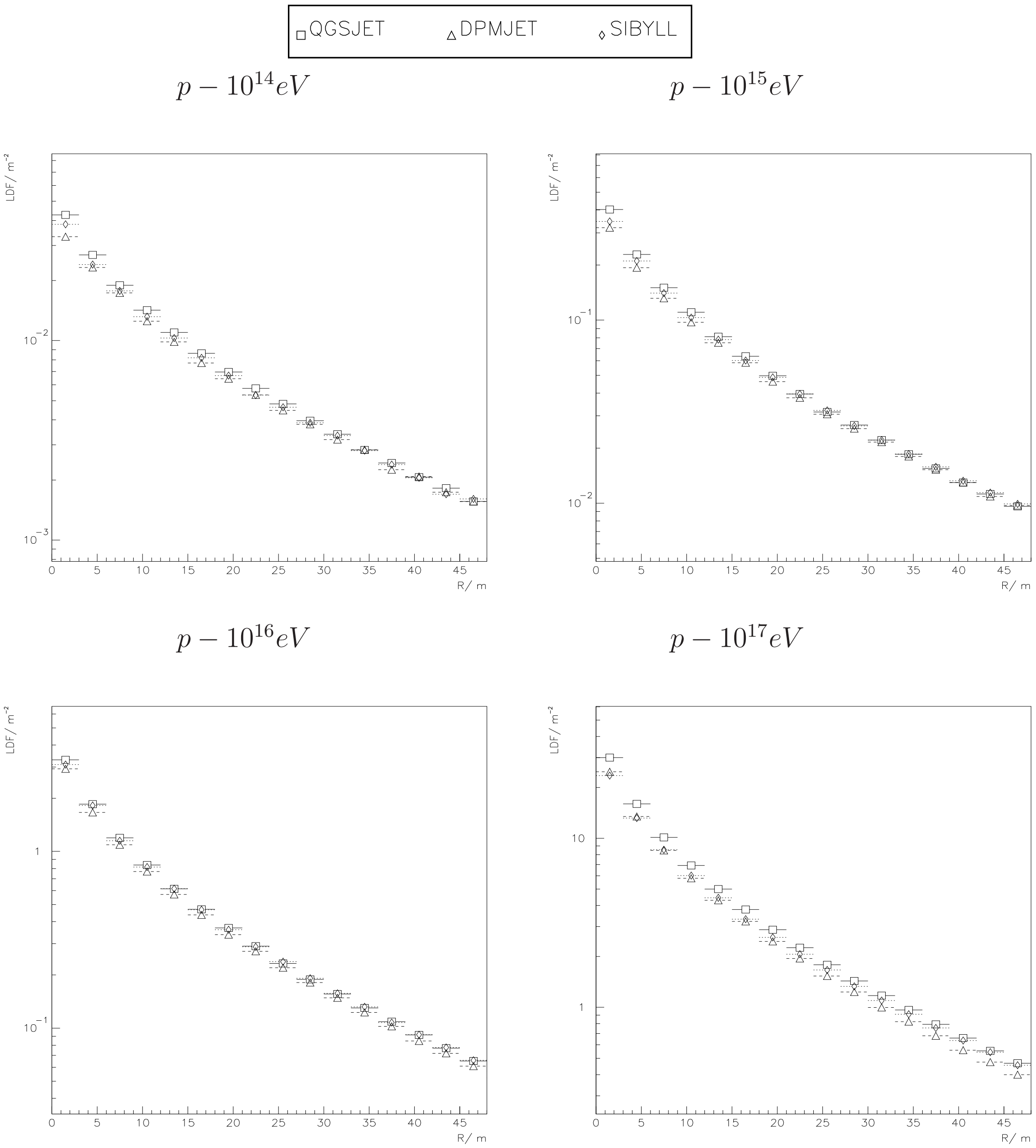

Figure 5.3: Muon lateral distribution functions ($E_\mu > 50\ GeV$) for proton vertical showers at different energies. Predictions of three models (QGSJET, DPMJET, SIBYLL) are marked by different labels - see the legend above the plots and the text in Sec. 5.1.

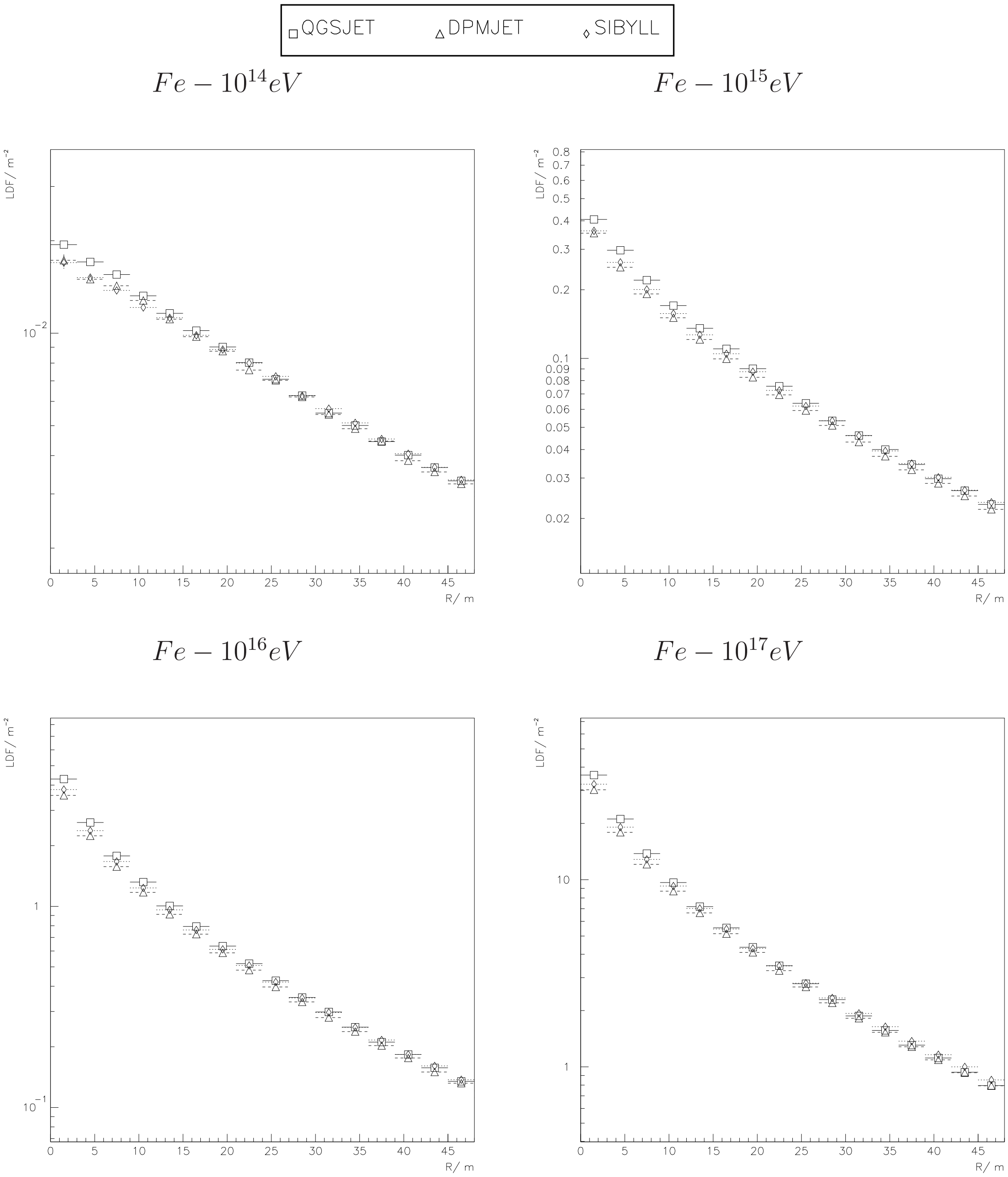

Figure 5.4: Muon lateral distribution functions ($E_\mu > 50\ GeV$) for iron vertical showers at different energies. Predictions of three models (QGSJET, DPMJET, SIBYLL) are marked by different labels.

The energy distributions in all simulated data samples were generated with the energy spectrum E^{-1} in order to obtain sufficient representation of the events at the upper part of the energy spectrum (i.e. in the range of large multiplicities). Events were then re-weighted to appropriate natural energy spectrum: E^{-3} bellow the knee and $E^{-2.7}$ above the knee. The statistical errors in any (re-weighted) distribution (e.g. multiplicity, projected angle) have to be re-weighted as well. Statistical error Δ_i of bin i in a given weighted distribution could be derived according to formula: $\Delta_i = \sqrt{\sum_{j=1}^{n_i} w_{ji}^2}$, where i is the bin number, n_i is the number of entries in bin i and w_{ji} is the weight of event j in bin i.

The standard U.S. atmosphere parameterized by J. Linsley was taken in the simulation. The NKG option explained in Sec. 2.6.3 was used to describe the electromagnetic component. This choice saves computing time and electrons (gammas) are not needed in our case. Muon multiple scattering is simulated according to the Molière theory. All simulations were done without thinning.

5.2.2 Choice of the simulation area

Because the detector is small compared to the size of showers, the shower core position is not known in experiment. It is consequently necessary to simulate showers in reasonable large area around the DELPHI detector, i.e. to smear showers around DELPHI. The choice has to be made about the size of this area. It is a question of a compromise between two competitive aspects. If the area size is too small a systematic decrease of small multiplicities appears in the final multiplicity distribution. On the other hand, showers with large distance from the detector produce just small number of muons or they are not measured at all. Thus unreasonably large area requires much bigger data samples in order to obtain enough statistic at high multiplicities. The value R of the radius, within which the generated showers are smeared, was finally chosen to be 200 m, having in mind both above-mentioned aspects.

Fig. 5.5 a) and 5.6 a) show the fraction of vertical showers within circle of the radius R around the detector that are recorded by DELPHI as at least 1, 2, $\ldots$, 10 muon events. The value R at which a curve is close to unity means that almost all showers (giving corresponding number of muons) have to be within the radius R. The crosscheck concerning the choice $R = 200\ m$ can be performed from these plots. The events giving muon multiplicity N_μ have to be almost fully contained within circle of $R = 200\ m$, i.e. the fraction at $R = 200\ m$ should be ~ 1. As mentioned in Chapter 4 the cosmic trigger is stable at $N_\mu > 3$. Considering this multiplicity the blue curve in Fig. 5.5 a) and 5.6 a) is relevant for our purpose. The crosscheck works for all energies chosen in Fig. 5.5 a) and 5.6 a) except of the highest energy $10^{18}\ eV$. At this energy $\sim 2.5\%$ of showers giving $N_\mu \geq 4$ are produced outside the region with $R < 200\ m$. However, these events do

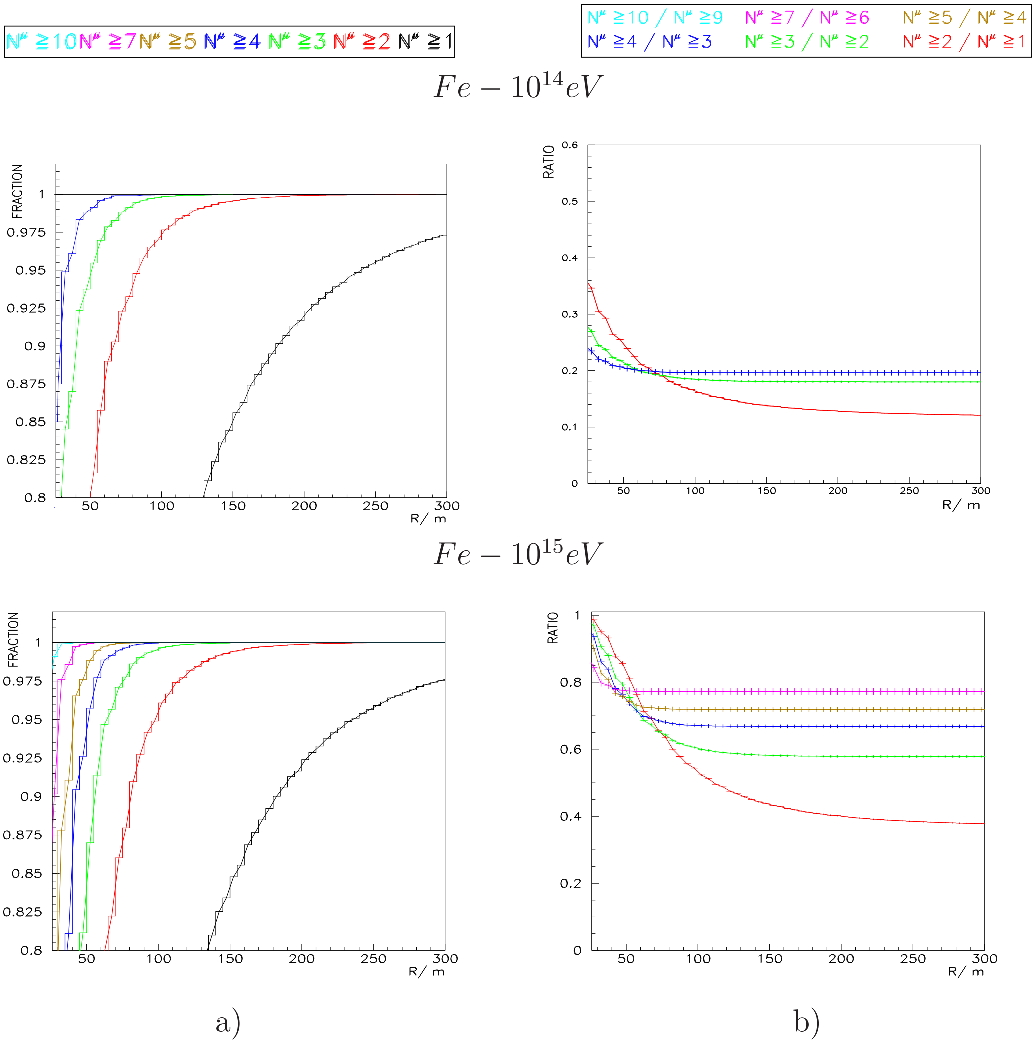

Figure 5.5: a) Fraction of vertical showers within circle of the radius R around the detector that are recorded by DELPHI as at least 1, 2, $\ldots$, 10 muon event. b) Ratio of two adjacent bins ($N_\mu \geq 2/N_\mu \geq 1$, $N_\mu \geq 3/N_\mu \geq 2$, $\ldots$, $N_\mu \geq 10/N_\mu \geq 9$) in integral multiplicity distribution as a function of the radius R. QGSJET model is used with CORSIKA to get these distributions. For further discussion see the text in Sec. 5.2.2.

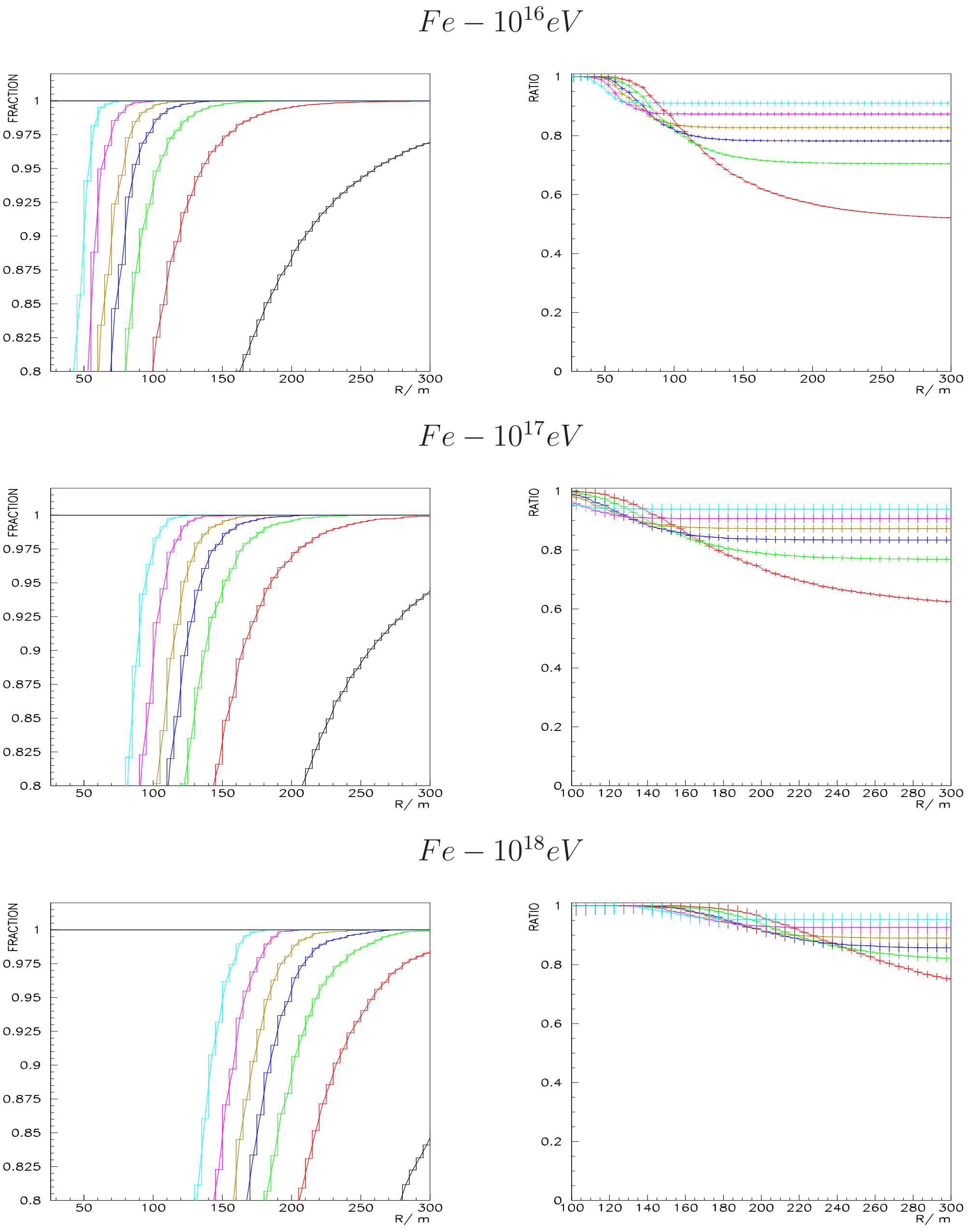

a) b)

Figure 5.6: a) Fraction of vertical showers within circle of the radius R around the detector that are recorded by DELPHI as at least 1, 2, $\ldots$, 10 muon event. b) Ratio of two adjacent bins ($N_\mu \geq 2/N_\mu \geq 1$, $N_\mu \geq 3/N_\mu \geq 2$, $\ldots$, $N_\mu \geq 10/N_\mu \geq 9$) in integral multiplicity distribution as a function of the radius R.

not influence the total multiplicity spectrum, because the population of small multiplicities is dominated by energies $< 10^{15}\ eV$.

The right hand side of Fig. 5.5 and 5.6 represents the ratio of two adjacent bins ($N_\mu \geq 2/N_\mu \geq 1$, $N_\mu \geq 3/N_\mu \geq 2$, $\ldots, N_\mu \geq 10/N_\mu \geq 9$) in integral multiplicity distribution. As the radius R increases the ratio stabilizes. The multiplicity distribution is stable at $R = 200\ m$ for almost all tested energies and $N_\mu \geq 4$. At $10^{18}\ eV$ the stability is approached at $N_\mu \geq 7$.

In Fig. 5.5 and 5.6 the iron nucleus was chosen as primary particle because it generally produces showers with larger spread compared to light nuclei.

The smearing of shower cores is performed around the center of the detector in the plane perpendicular to the shower direction. This procedure was chosen according to [83] and it requires CORSIKA program running in the mode of “volume detector”. Other option is to use default “flat” version of CORSIKA, i.e. to assume flat detector and then smear showers in the horizontal plane. It turned out during the analysis that the latter option changes the angular dependency of final reconstructed events and makes the upper part of zenith angular distributions incompatible with the data. For this reason the volume CORSIKA is taken and the smearing is performed in the plane perpendicular to the shower direction.

Also the influence of geomagnetic field was checked. The displacement of hard muon component with respect to shower center due to different geomagnetic rigidity is small compared to the radius of the smearing area. Only at smaller energies ($E \sim 10^{13}\ eV$) the effect is of some relevance and it slightly influences the predicted number of low multiplicity events ($N_\mu < 4$) (DELPHI triggers sufficiently only higher multiplicities).

During the shower smearing each shower was used $10\times$ at energies $E < 10^{16}\ eV$. For higher energies the number of moves is 100. However, taking 100 moves and energy interval $10^{16} - 3\ 10^{16}\ eV$ (simulation with iron nuclei) one shower contributed to the whole multiplicity spectrum ($N_\mu > 3$) on average $20\times$. In the region of large multiplicities ($N_\mu > 40$), which is dominated by primary energies $> 10^{16}\ eV$, one shower contributes on average only once.

5.2.3 Rock overburden

The rock above the DELPHI detector is represented according to simplified scheme shown in Fig. 3.1. The shape of the experimental cavern as well as basic structures such as concrete wall and three access shafts are included.

As already mentioned the energy cut-off for muons penetrating $\sim 100\ m$ of DELPHI overburden is about $50\ GeV$. However, this value is not sharp and the muon propagation was simulated using GEANT3 simulation. Fig. 5.7 shows the low energy part of muon spectrum (energy given on the Earth surface) for iron induced showers with primary energies $3\ 10^{15} - 10^{16}\ eV$ (zenith $0° - 60°$). As seen from Fig. 5.7 there are some muons with surface energy even less than 45 GeV. It is demonstrated in Fig. 5.8 that these muons come from the access shafts in the experimental cavern and the energy cutoff is thus significantly reduced in case of these muons. However, the inclusion of the shafts to the geometry description in GEANT simulation is not so important aspect since the probability of muon to pass through the shaft is small. No increase of multi-muon events in the direction pointing to one of the shafts has been observed in the data as well as in the simulation. The effect of shafts is relevant only for single muon events.

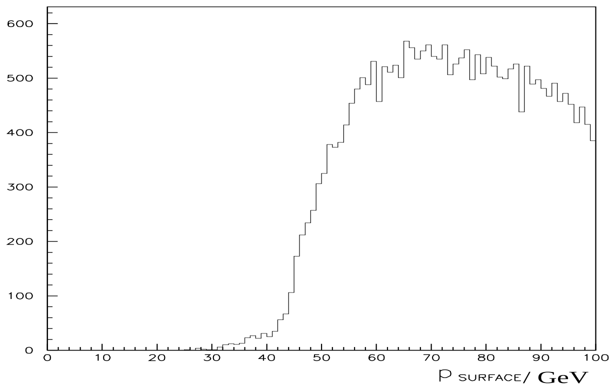

Figure 5.7: Example of the low part of momenta distribution of detected muons. The values on horizontal axis correspond to momenta on the Earth surface. Picture was obtained from iron induced showers with primary energies $3\ 10^{15} - 10^{16}\ eV$ (zenith $0° - 60°$)

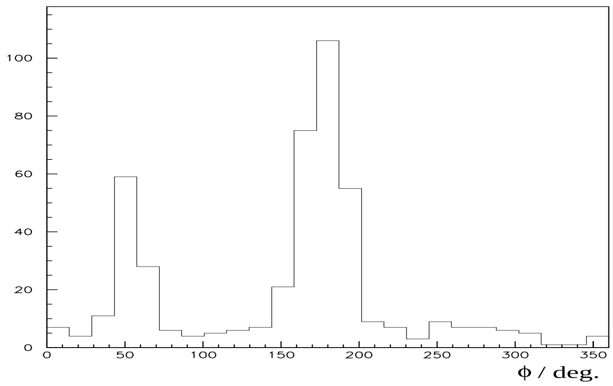

Figure 5.8: Example of the distribution of muon azimuthal angle. The content of the histogram corresponds only to the low energy part ($p_\mu < 45\ GeV$) of Fig. 5.7. The left (right) peak corresponds to shaft marked PIT2 (PIT3) in Fig.3.1.

More relevant for the simulation is the correct cylindrical shape of the experimental cavern. For example, when assuming the (incorrect) planar shape of the cavern ceiling, the energy cut-off for inclined showers would be reduced. The extremum is reached when the shower direction is perpendicular to the line between Pit 1 and Pit 3 in Fig. 3.1. The additional energy loss in case of the correct cylindrical cavern shape when compared to the planar approximation is 1 GeV at zenith angle $\theta = 30°$ and 5 GeV at $\theta = 60°$.

5.2.4 ECTANA reconstruction in HCAL

Finally, the simulated events are reconstructed in the same way as the real data, i.e. using ECTANA reconstruction program. Because the muon tracks are reconstructed in one spatial projection only (plane perpendicular to the LEP beams - Appendix A), at high multiplicities some muons in HCAL overlap and consequently the reconstructed multiplicity is smaller than the real one. This shadowing effect is demonstrated in Fig. 5.9 where the reconstructed multiplicity is plotted as a function of the number of muons entering the calorimeter. The shadowing effect requires detailed simulation of DELPHI HCAL. This was done with the DELSIM simulation package. The MC simulations are compared with the data in terms of reconstructed multiplicity, i.e. when the shadowing effect is already taken into account.

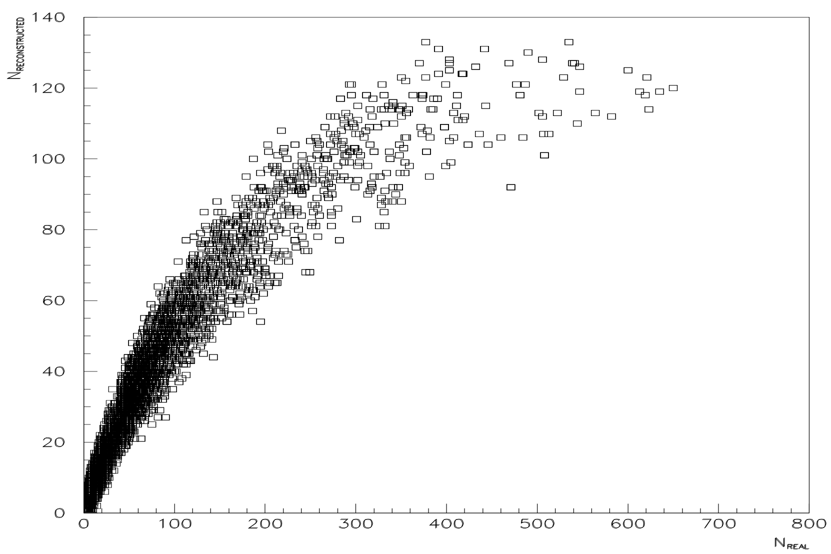

Figure 5.9: The relation between real and reconstructed number of muons in HCAL.

The probabilities that the N_{MC}^{REAL} multi-muon event is reconstructed as the event with N_{μ}^{REC} muons are plotted in Appendix B. The distributions are given for different values of N_{MC}^{REAL}. The Gaussian parameterization of these distributions is satisfactory for each value of N_{MC}^{REAL}.

5.2.5 TPC reconstruction

Contrary to HCAL the TPC reconstruction does not suffer from shadowing effect and the number of reconstructed muons corresponds to the known number of muons entering the TPC volume. Consequently it was not necessary to run detailed reconstruction program DELANA (TPCANA) on the simulated events and the reconstructed multiplicity was taken as a count of muons passing through TPC.

5.3 Multiplicity distributions

The final simulated distributions of muon multiplicities depend necessarily on the assumed energy spectrum of primary particles. For purpose of this section the spectrum corresponding to the full line in Fig. 5.10 is taken (line labelled as number *1*). It represents upper limit of recent measurements and it assumes spectrum energy dependence in the form:

$$dN/dE \sim E^{-2.7} \ \ (E < 3\ 10^{15} eV) \qquad\qquad dN/dE \sim E^{-3.0} \ \ (E > 3\ 10^{15} eV)$$

As already explained, the multiplicity measurement in HCAL suffers from shadowing effect which reduces the number of reconstructed tracks when compared to the number of muons entering the calorimeter. Therefore only the integrated multiplicity distributions are given. All events with given multiplicity or higher contribute to the corresponding bin in the integrated distributions. Fig. 5.11 and Fig. 5.12 show the contributions of different energy intervals to the final integrated multiplicity distribution. The histograms are calculated with protons and iron nuclei as primary particles.

The result is of course limited by the size of MC samples. The statistical errors are given. Influence of other uncertainties will be discussed in the next chapter (Sec. 6.4).

The saturated events appear also in the simulation as well as in real data. In case of iron primaries the total number of (re-weighted) saturated events is 3.3 ± 1.1. In case of primary protons the number of expected saturated events is 1.1 ± 0.4. These events were included in Fig. 5.11 and Fig. 5.12 in the histogram corresponding to energies $10^{16}\ eV - 10^{17}\ eV$.

The simulated multiplicity distribution as measured in TPC is plotted in Fig. 5.13 for both assumed types of primaries. In this figure it is required that

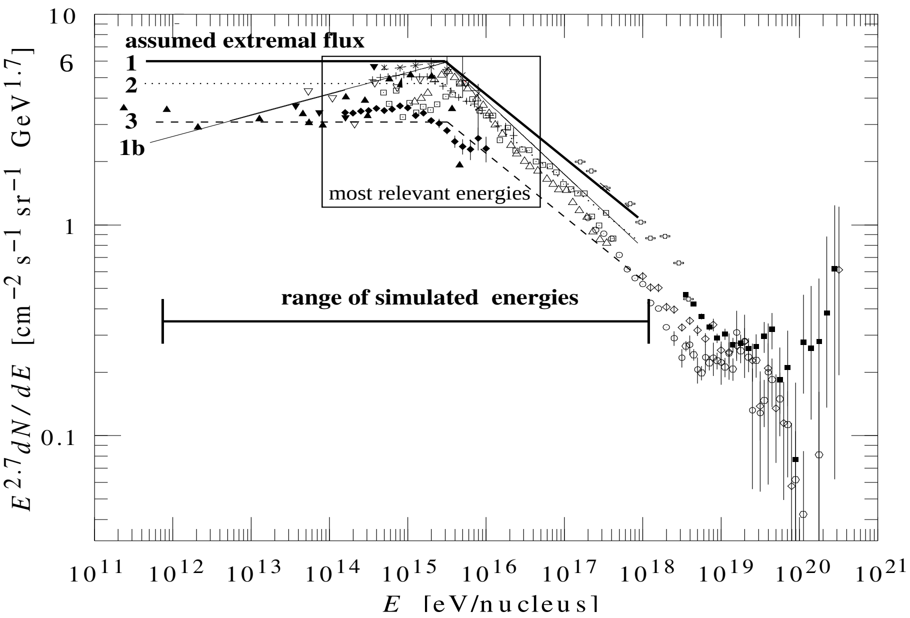

Figure 5.10: Assumed fluxes compared to various measurements. The picture is taken from [30] and modified. For references to different experimental points see Fig. 2.2. The squares close to line *1* correspond to results of Haverah Park taken from [84] using the macro available at http://astroparticle.uchicago.edu/announce.html. Fluxes are multiplied by $E^{2.7}$.

the HCAL multiplicity is higher than 15, i.e. the same condition is applied as in the real data analysis (see Sec. 4.6 and Fig. 4.10). It should be emphasized that the size of TPC is about 7 m^2 in the projection perpendicular to vertical axis. Compared to 75 m^2 of HCAL area the TPC is by a factor 10 smaller. Therefore the absolute values of multiplicities are much reduced. For technical reasons described in Sec. 4.6 the live time in case of TPC data is 1.2 10^6 s only.

The normalization of all distributions in Fig. 5.11, 5.12, 5.13 is absolute. It is inferred from the flux (marked as *1*) in Fig. 5.10 taking into account the total data taking time and the size of the area where we smear the showers. The choice of the particular flux *1* means that the distributions 5.11, 5.12, 5.13 describe the upper limit of what can be measured at DELPHI.

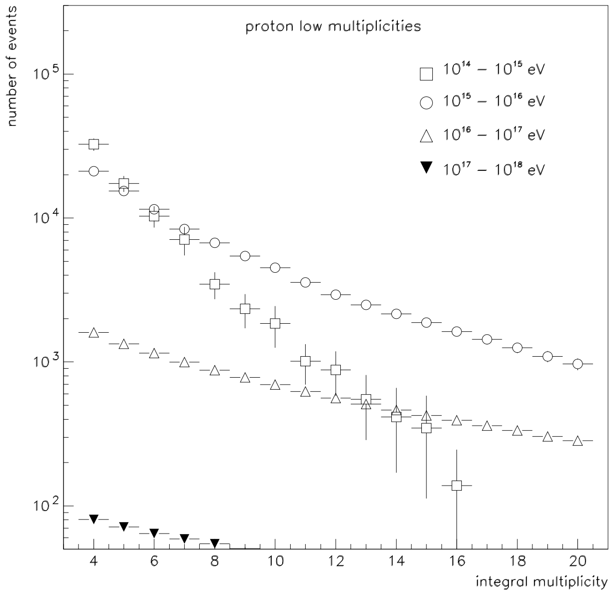

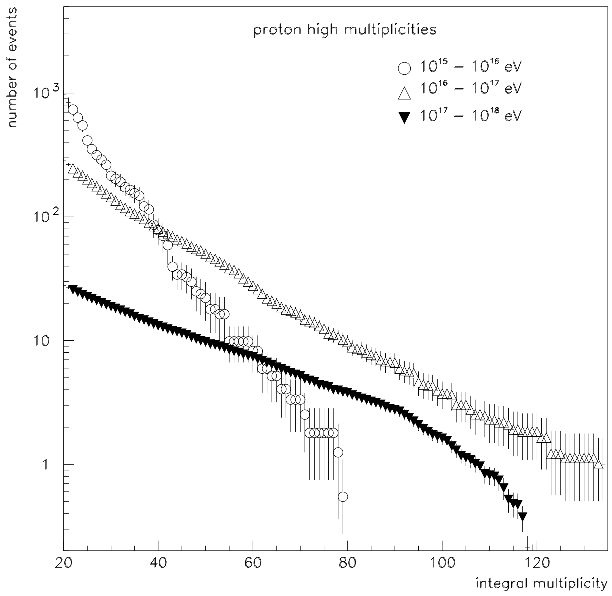

Figure 5.11: Contributions of different energy intervals to the final integral multiplicity distribution. Primary particles are proton nuclei. The energy intervals $E < 10^{14}\ eV$ significantly contribute only to multiplicities $N_\mu \leq 3$.

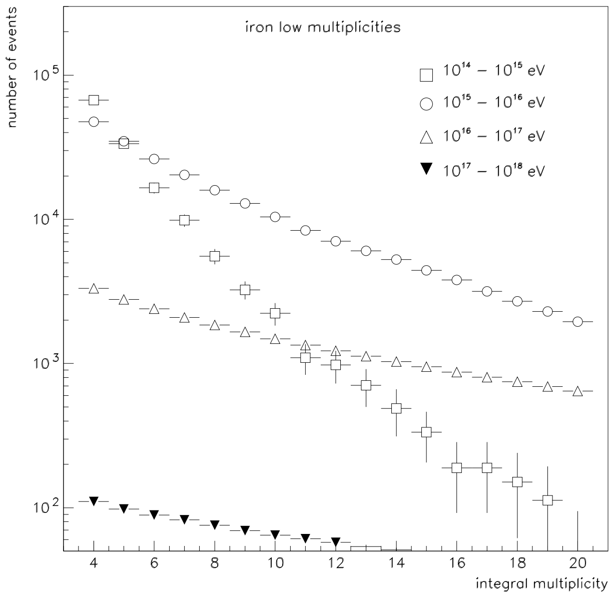

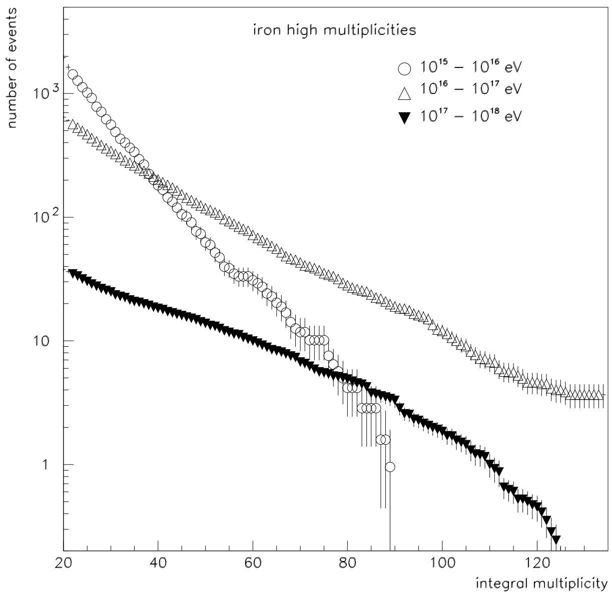

Figure 5.12: Contributions of different energy intervals to the final integral multiplicity distribution. Primary particles are iron nuclei.

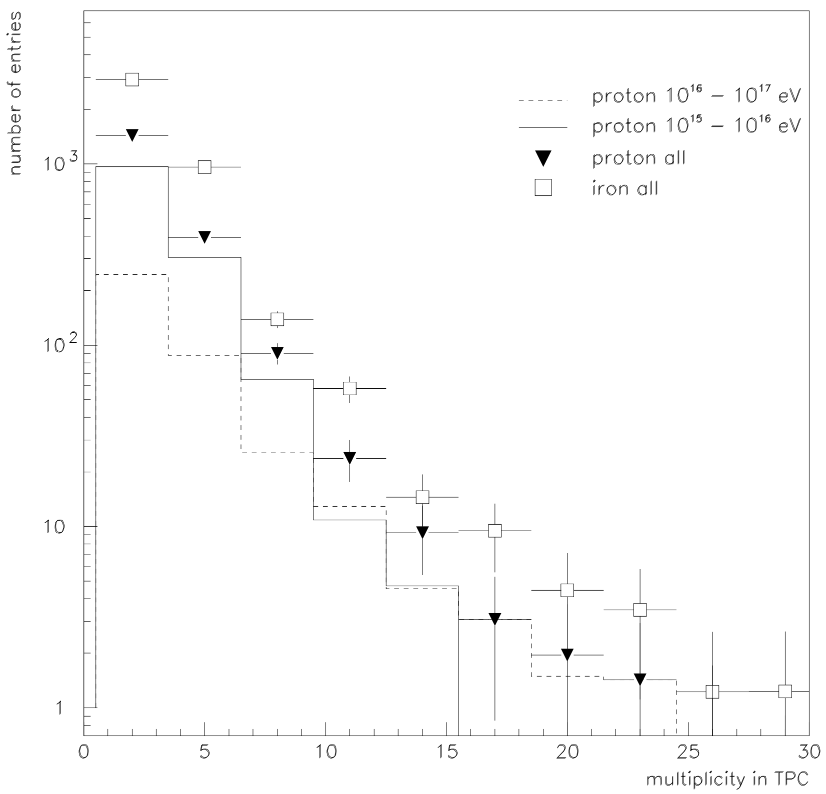

Figure 5.13: Multiplicities of events with more than 15 muons in hadron calorimeter as measured in TPC. Predictions for protons and iron nuclei are displayed. In case of protons, histograms of two most contributing energy ranges $10^{15}\ eV\ -\ 10^{16}\ eV$, $10^{16}\ eV\ -\ 10^{17}\ eV$ are plotted as well.

6 Results

The results predicted by CORSIKA with QGSJET model can be compared with measurements of reconstructed multiplicity in HCAL and mean projected angle from HCAL. The results obtained from TPC data are also compared with the simulation.

6.1 HCAL multiplicity

The comparison of the predicted and measured multiplicity reconstructed from HCAL is plotted in Fig. 6.1. Because of the shadowing effect the distributions represent the integrated multiplicity. The assumed primary flux represents the upper limit of various measurements and it corresponds to line *1* in Fig. 5.10.

From Fig. 6.1 it is clear that the data are compatible with the proton spectrum in first several bins at low multiplicities. In the multiplicity range $10 - 20$ the data could be described as a mixture of light (proton) and heavy (iron) component of primary cosmic rays. Higher multiplicities could be described only by the extreme assumption that all primary particles are iron nuclei. At the highest multiplicities even the MC prediction for iron nuclei is not sufficient to reproduce the measurement.

The relative statistical errors induced by limited size of MC samples are larger at the highest multiplicities. Ratio defined as the number of observed events to the number of predicted events $R = N_{DATA}/N_{MC}^{IRON}$ equals 1.28 ± 0.18 for $N_\mu \geq 70$ and 1.45 ± 0.23 for $N_\mu \geq 80$. The event excess in the data with respect to prediction of iron nuclei is thus observed with the significance 1.6 σ ($N_\mu \geq 70$) and 1.9 σ ($N_\mu \geq 80$). Data are clearly above the prediction for protons starting already from low multiplicities $N_\mu > 7$. At multiplicity $N_\mu > 20$ the ratio $R = N_{DATA}/N_{MC}^{PROTON}$ gives the value 2.24 ± 0.17 corresponding to the significance $\sim 7.4\ \sigma$.

On the other hand, the assumed flux in Fig. 6.1 is the very upper limit of recent measurements. At lower fluxes the observed number of high multiplicity events clearly exceeds the MC prediction for iron nuclei. The dependency of the result on the assumed primary flux is discussed in Sec. 6.3.

6.2 Projected angle

The projected angle of observed tracks is defined in the DELPHI *(x,y)* plane (Appendix A). It was shown in Fig. 4.6 that the distribution of projected angle is similar to what one would expect from the work [81].

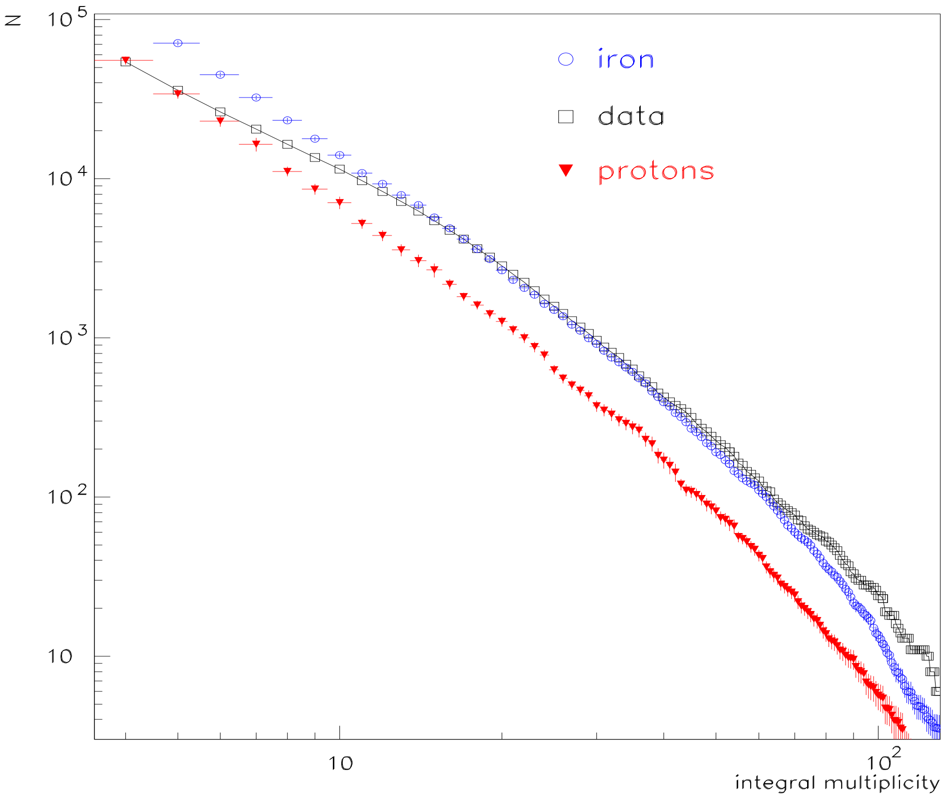

Figure 6.1: Integrated multiplicity measured in HCAL together with the result of MC simulation for iron and proton primary particles. Contributions of different energy intervals in Figs. 5.11, 5.12 are summed up.

The distribution of the projected angle is compared with the MC simulation for two event samples with $N_\mu \geq 4$ and $N_\mu \geq 20$ respectively. The first multiplicity corresponds to the point in Fig. 6.1 where data can be described by proton primaries only. Similarly the second multiplicity represents the region where the MC simulation of iron nuclei almost coincides with the data. From Fig. 6.2 and 6.3 it is apparent that the data agree with the proper one of the two MC predictions in the whole range of angles.

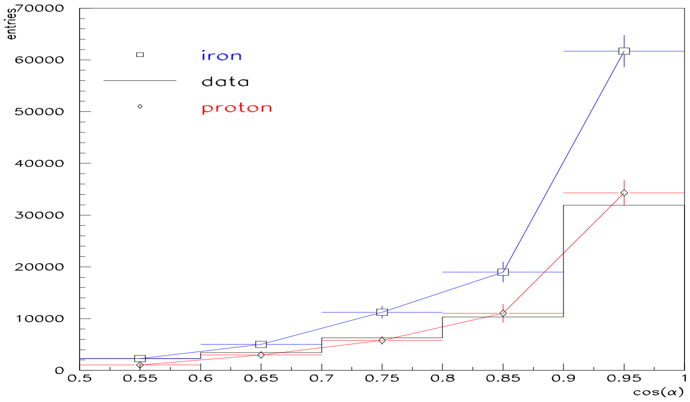

Figure 6.2: Projected angle at $N_\mu \geq 4$ for iron simulation (squares), data (full line) and proton simulation (diamonds).

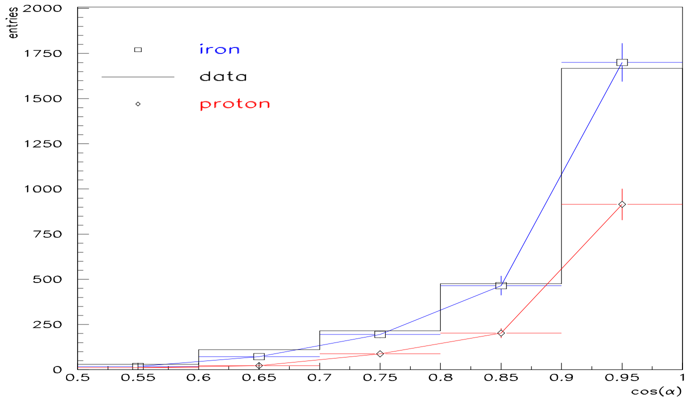

Figure 6.3: Projected angle at $N_\mu \geq 20$ for iron simulation (squares), data (full line) and proton simulation (diamonds).

6.3 Flux

The predicted multiplicity distributions of course depend on the assumed flux of primary particles. Fig. 5.10 shows four lines corresponding to different assumed fluxes. Lines *1*, *2* and *3* have power law indices $\gamma = 2.7$ below the knee ($E_{knee} = 3\ 10^{15}\ eV$) and $\gamma = 3.0$ above the knee. Assumption *1b* is defined by exponents $\gamma = 2.6$ below and $\gamma = 3.05$ above the knee. Line *1* corresponds to maximal allowed flux which at low and high energies overestimates the measurements but in the crucial part of energy spectrum it fits the upper limit of the experimental values. So far only this flux has been used in the analysis. In Fig. 6.4 it is plotted the comparison between the data and three assumed fluxes *1*, *2* and *3*. The data agree better with high flux in the energy region $10^{15}\ eV - 10^{16}\ eV$, only with this assumption the prediction for iron nuclei can approach the data points at medium multiplicities. When using the other two assumptions *2* or *3*, the data disagree both with the proton and iron predictions already at lower multiplicities. The choice of particular pair of power law indices of course influences the shape of the predicted multiplicity spectrum[1]. However, these predictions should always be within the red (blue) region defined by maximal and minimal assumption *1* and *3*.

The general conclusion one can draw from Fig. 6.4 is that only extreme combination of high assumed fluxes and heavy composition of cosmic particles approaches the data. In the region of very high multiplicities $N_\mu \geq 70$ the data are slightly above the prediction for iron nuclei even when the maximal flux *1* is assumed. Unfortunately, due to large statistical errors the significance in this region is only on the level of 1.6 σ ($N_\mu \geq 70$) or 1.9 σ ($N_\mu \geq 80$). Already in case of the flux *2* the ratio $R = N_{DATA}/N_{MC}^{IRON}$ reaches the value of 1.71 ± 0.24 ($N_\mu \geq 70$) corresponding to the disagreement on the level of about 3 σ.

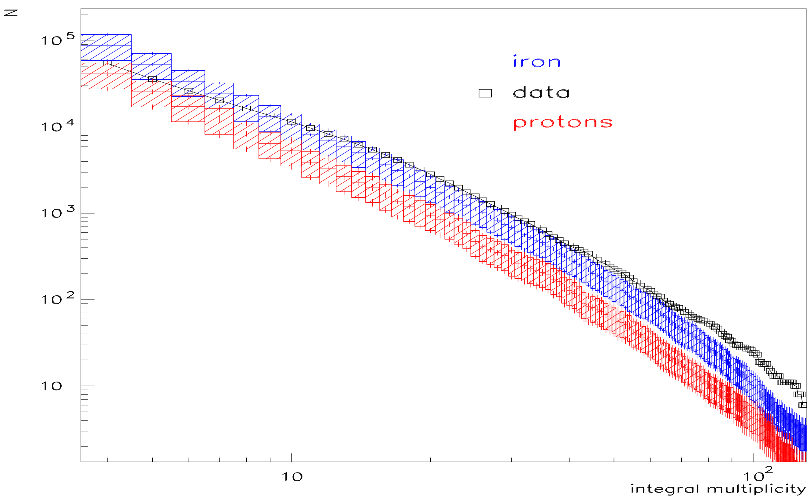

Figure 6.4: Results of three assumed fluxes *1* (the highest results) , *2* (the middle distributions) and *3* (the lowest curves). Both iron nuclei and proton curves are plotted.

[1]Results with other pair of power law indices (flux *1b*) will be shown in Sec. 6.6 with the modified QGSJET.

6.4 Errors

The result is influenced by various detector effects. Even if DELPHI apparatus is simulated in details, the additional impact of cathode readout electronics is taken into account in this Section.

When the muon track passes close ($\sim 50\ cm$) to the readout boards between the barrel parts of HCAL and end-caps, the electronic signal from streamer tubes is stronger and it could propagate to subsequent electronic channel corresponding to another nearby tube. This effect is called "cross-talk" and it could be simulated within the ECTANA package as an alternative option. Faked hits are effectively produced and if the number of such hits is high enough the widened track can obscure more other tracks than normally or an artificial track could be reconstructed close to the real one. The impact of this effect is demonstrated in Fig. 6.5, where the simulations with and without the cross-talk are shown in case of the energy interval $E = 10^{16} - 10^{17}\ eV$ with iron nuclei as primary particles. The results with and without the effect are strongly correlated, because the same CORISKA/GEANT data are used in both cases. The important observation is, however, that the results agree within the statistical errors. The impact of cross-talk at low multiplicities, where the simulation statistics is better, is about 3% with respect to the simulation without cross-talk option.

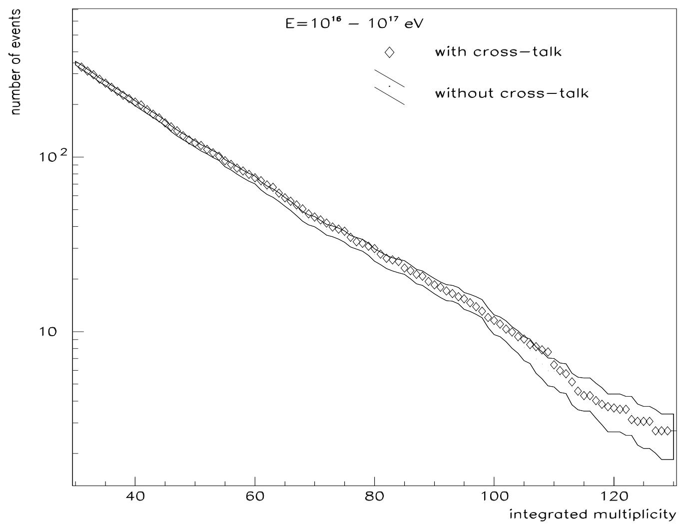

Figure 6.5: The predicted integrated spectrum of muon multiplicities at energy interval $10^{16}\ eV - 10^{17}\ eV$ for iron primary particles. Two simulations with and without cross-talk are compared.

6.4.1 Uncertainty of the rock definition

Another uncertainty concerns the rock overburden. The densities of individual rock layers were given in Sec. 3.1 (Fig. 3.1). The $\pm 5\%$ error of the rock density is assumed. From point of view of our analysis the eventual overestimation of the density is more serious as this could lead to decreased muon multiplicities. Therefore the emphasis was put on -5% case. The impact of modified density was studied and the results with changed density values were clearly consistent with the default rock within the statistical errors.

The results for the energy interval $3\ 10^{16}\ eV - 10^{17}\ eV$ for rock density $\rho' = 0.95 \times \rho$ are presented in Fig. 6.6. The modified distribution and the default one are again strongly correlated, because the same CORSIKA events are propagated through different rocks. However, within the statistical errors the results are consistent between each other also at the highest multiplicities.

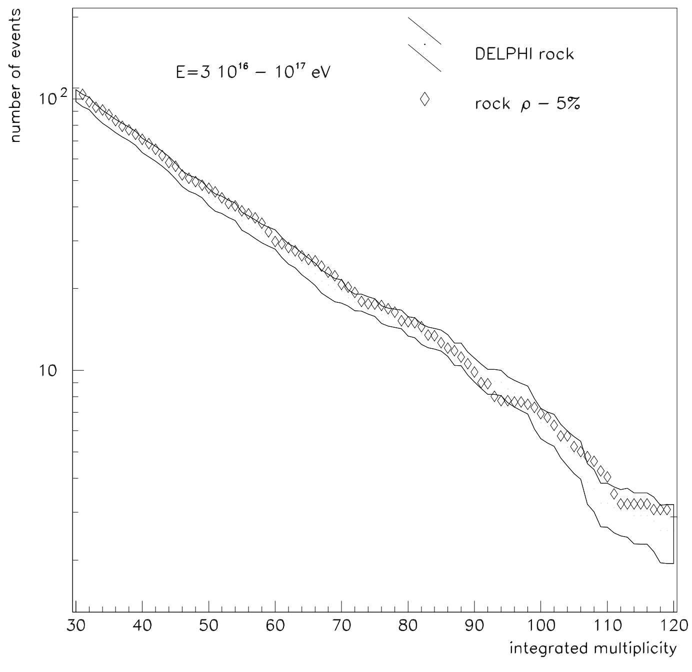

Figure 6.6: The predicted integrated spectrum of muon multiplicities in case of energy interval $3\ 10^{16}\ eV - 10^{17}\ eV$ with iron primary particles. Two simulations of different rock are given: standard rock as defined in Fig. 3.1 and results with densities changed by -5%.

6.5 Results from TPC

The muon multiplicity measured in TPC (Fig. 4.10) is compared to the prediction of iron nuclei and protons in Fig. 6.7. The distributions are normalized with respect to flux *1*.

The data have tendency to be close to the iron prediction because only events with HCAL multiplicity higher than 15 are analyzed. The occupancy at the highest multiplicities are slightly above the prediction for iron nuclei.

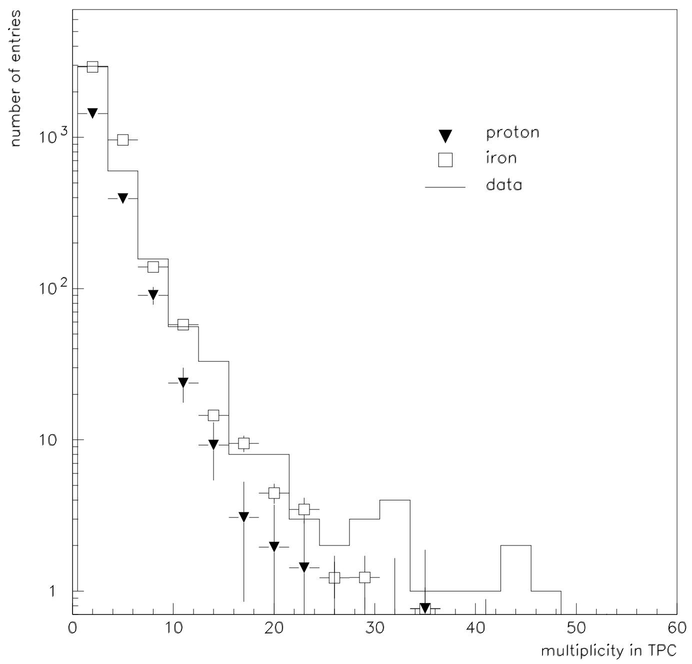

Figure 6.7: The multiplicity spectrum measured in TPC. Predictions for the flux *1* are given in case of proton and iron nuclei. More than 15 muons are required in HCAL.

6.6 Modification of QGSJET parameters

The QGSJET model [2] developed by Kalmykov and Ostapchenko is widely used in the community of astroparticle physicists. It was shown that this model best describes the correlations between different components of atmospheric shower [68]. As seen from previous parts of this chapter, even the QGSJET prediction describes the observed muon multiplicity spectrum only with extreme assumptions that starting from certain energy all cosmic primaries are iron nuclei and the flux has to be assumed as high as possible. In Sec. 5.1 (Fig. 5.3, 5.4) it was demonstrated that QGSJET predicts more high energy muons than DPMJET and SIBYLL - the other two models used frequently for shower simulations. From this point of view we cannot expect that these models would help us to improve the consistency between data and simulations. Due to this reason it was suggested [85] not to check the multiplicity spectra predicted by other models like SIBYLL but rather to study the impact of QGSJET internal parameters on the produced multiplicity spectrum.

The work [86] deals with various modifications of QGSJET interaction parameters. It was found that certain changes of inelastic cross-section and elasticity in the model can help to improve our understanding of the inconsistencies among the results of various air shower experiments concerning the cosmic ray composition. In general, the experiments measuring particle distributions at ground level give quite different results of mean logarithmic mass $< ln\ A >$ (see Fig. 2.3) compared to experiments measuring the longitudinal development of showers.

When decreasing the cross-section, the showers penetrate deeper into the atmosphere. Similar effect is caused by the reduction of inelasticity. The average fraction of energy transfered to secondary particles is smaller in each interaction. The leading particle carries away more energy, consequently the shower maximum is reached deeper in the atmosphere.

Changing the model parameters the interpretation of data changes as well. For a given shower with lower assumed inelastic cross-section (or higher elasticity) the extracted mass of the cosmic primary (at a given energy) has to be larger. Only in this way the shower maximum is created at the same height in the atmosphere. Consequently the estimated $< ln\ A >$ increases. Better consistency between measurements on the ground and estimates based on the longitudinal shower profiles is thus obtained. Furthermore the work [86] stresses that the (modified) results of individual experiments are consistent with phenomenological *poly gonato* model [87] of cosmic ray composition. The best consistency between the phenomenological model and re-calculated $< ln\ A >$ was found for modification marked *3a* in [86].

Concerning the measurements on the ground the number of produced muons and electrons also changes when modifying original parameters. The decrease of cross-section and increase of elasticity lead to increase of the average number of observed muons as shown in [86]. The modification *3a* induces $\sim 15\%$ gain in the number of muons (with the energy threshold $E_\mu > 100\ MeV$) with respect to QGSJET. The unique data allow us to test further the implications of the changed parameters on high energy muon component of the showers. The model *3a* from [86] was chosen because the largest effects are expected for this particular modification.

The inelastic cross-sections in the model *3a* were reduced by reducing the minijet contribution. Changing this parameter the pseudo-rapidity was also influenced and another parameter was adjusted to match the measured pseudo-rapidity distribution from TEVATRON. Similarly the average transverse momentum $< p_t >$ is also affected and it was again re-adjusted to match the measurements. Moreover the elasticity of the most energetic particle in π-nucleus collisions has been additionally increased by $\sim 10\%$ relatively to what one would obtain by reduction of minijets only. For details we refer to [86].

The changed inelastic *pp* cross-sections in the modification *3a* are compared to QGSJET in Tab. 6.1 and Fig. 6.8 as a function of laboratory energy. The experimental points in Fig. 6.8 correspond to values obtained from three TEVATRON experiments as a difference between the total measured cross-sections (CDF [88], E-710 [89], E-811 [90]) and the cross-sections in the elastic channel (CDF [91], E-710 [92], E-811 [90]). The model 3a corresponds to about 1 σ deviation from what is measured by E-711 and E-811.

energy	QGSJET	model 3a
E [eV]	σ_{pp}^{inel} $[mb]$	σ_{pp}^{inel} $[mb]$
10^{11}	30	30
10^{12}	35	35
10^{13}	40	40
10^{14}	48	45
10^{15}	57	51
10^{16}	68	57
10^{17}	80	64
10^{18}	93	72
10^{19}	107	80

Table 6.1: The inelastic *pp* cross-section in QGSJET and the modification 3a from [86]

Fig. 6.9 shows the lateral distribution functions generated by QGSJET and the modification *3a* in case of two energies (10^{15} eV, 10^{16} eV) and iron nuclei as primary particles. It is demonstrated that the modification *3a* produces more muons when compared to QGSJET. Close to the shower core the average amount of muons is higher by about 10% in case of the model *3a* compared to original QGSJET.

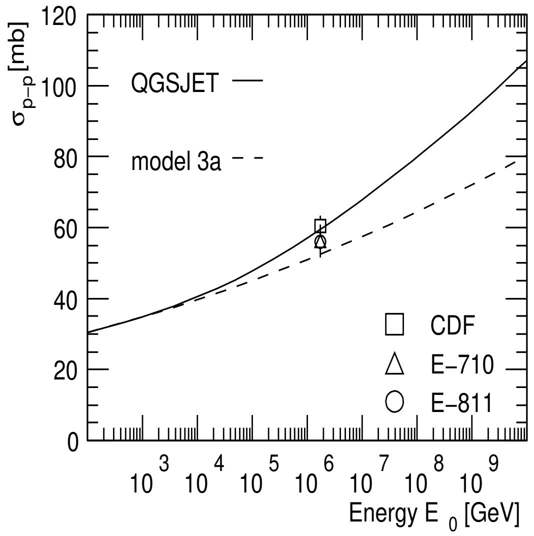

Figure 6.8: The inelastic pp cross-section in QGSJET and modification 3a as a function of laboratory energy. TEVATRON measurements of $p\bar{p}$ inelastic cross-section by three experiments CDF, E-710, E-811 are given. The picture was taken from [86].

6.6.1 Results with modified parameters of QGSJET

The final comparison of data with the predicted multiplicity spectra in the case of QGSJET and the model with modified parameters is plotted in Fig. 6.10. The normalization of all simulated predictions is done according to the flux *1* in Fig. 5.10, i.e. to the highest assumed flux. The latest version of CORSIKA (*ver 6.031* from February 2004) was used in case of the model *3a*.

It is clear that the modification adds to the prediction of QGSJET about 10% events spread in the whole range of multiplicities. The relative gain in the number of events is a bit larger in case of protons than in case of iron nuclei.

The model *3a* enlarges the region where the data are between the proton and iron predictions. Using QGSJET, the data reach the iron prediction at multiplicity ~ 20. With the model *3a* the data are consistent with the mixture of light and heavy component up to the multiplicity ~ 70 (the ratio $R = N_{DATA}/N_{MC}^{IRON}$ equals 1.14 ± 0.15 at $N_\mu \geq 70$). Slight event excess in data compared to prediction of iron nuclei is still apparent at the highest multiplicities, however, now with smaller significance (for $N_\mu \geq 80$, $R = 1.36 \pm 0.21$ corresponding to $\sim 1.7\ \sigma$ effect). Consequently, the results with modified parameters are more consistent with the underground muon data.

In first two bins the number of predicted events (in proton case) is now higher than data. Taking the flux assumption *2* the number of events in first bins

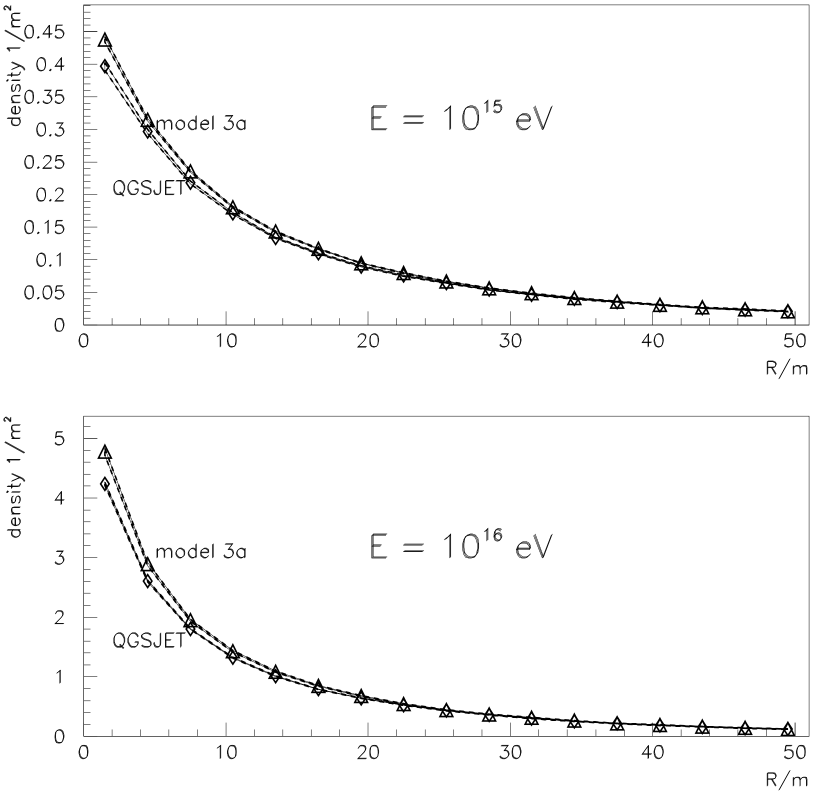

Figure 6.9: Muon lateral distribution function of vertical showers 100 m underground in case of iron primaries at two energies 10^{15} , 10^{16} eV. Results of QGSJET are compared with the modification *3a* from [86].

becomes compatible with the data. Similar effect is obtained by modification of the first power law index from $\gamma = 2.7$ to $\gamma = 2.6$, e.g. according to flux marked *1b* in Fig. 5.10. The result with the assumption *1b* is plotted in Fig. 6.11.

More realistic flux *1b* is smaller than the flux *1* at all assumed energies. Consequently, the number of predicted events in case of *1b* is smaller than the prediction of the flux *1* in the whole range of multiplicities.

When testing the model *3a* with flux *1b*, the data reach the iron prediction at multiplicity $N_\mu \sim 50$. The ratio $R = N_{DATA}/N_{MC}^{IRON}$ equals 1.24 ± 0.17 at $N_\mu \geq 70$ ($R = 1.49 \pm 0.23$ $N_\mu \geq 80$). The significance of the event excess in data w.r.t. MC prediction of iron is now equivalent to 1.4 σ at $N_\mu \geq 70$ (2.0 σ at $N_\mu \geq 80$).

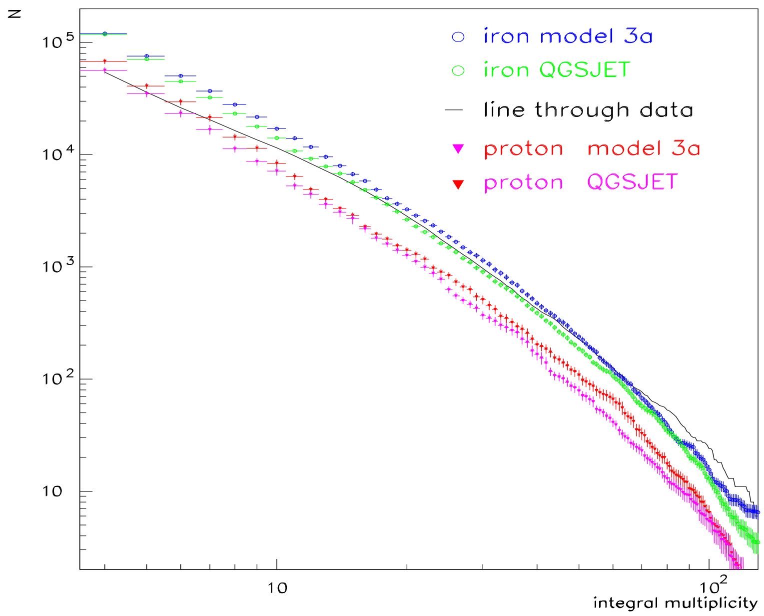

Figure 6.10: The integral multiplicity distribution for QGSJET and modification *3a* compared to data. Flux *1* is assumed.

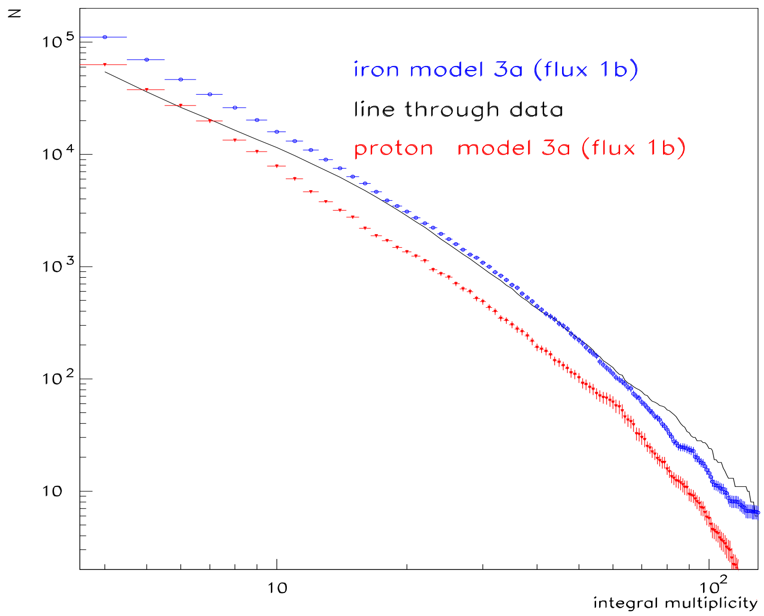

Figure 6.11: The integral multiplicity distribution for the modification *3a* compared to data. Flux *1b* is assumed.

6.7 Results of other LEP experiments

Qualitatively similar results are obtained from another LEP experiment COSMO-ALEPH. Large TPC with the detection area of about 16 m^2 was used in this experiment to reconstruct multi-muon bundles. They estimated the muon multiplicity distribution of measured events and compared it to the prediction of CORSIKA/QGSJET. In the simulation the muon energy cut-off E_{CUT} was assumed to depend on the zenith angle θ as $E_{CUT} = 70\ GeV/cos\theta$. The value $70\ GeV$ corresponds to the energy cut-off for vertical muons and it was estimated using the known underground location of the experiment (140 m below the Earth surface). All muons with direction pointing to the TPC volume and with energy higher than E_{CUT} were assumed to be detected and reconstructed.

Similarly to DELPHI, COSMO-ALEPH group [81] also observed the transition from light to heavy component with increasing energy. At the highest multiplicities they found indication of event excess in the data when compared to the prediction of iron nuclei. However, the observed excess suffered from low statistics (data are ~ 5 events above the prediction for iron nuclei). The medium multiplicities were consistent with reasonable mixture of iron and proton, see Fig. 6.12.

Another LEP experiment, L3+C precisely measured the spectrum of muon momenta in the energy range $20\ GeV - 2\ TeV$ using reconstruction of track curvature in muon chambers [93]. They were also able to reconstruct multi-muon events up to the multiplicity ~ 30. It was found that the dominance of heavy ions (iron) would be necessary to describe their data. Pure iron composition was consistent with the data in almost whole range of multiplicities [94, 95]. Their results are displayed in Fig. 6.13 separated into bins representing showers with different electromagnetic size. The electromagnetic component was measured by array of scintilator counters situated on the Earth surface above L3. The extreme assumption that almost all primary particles are heavy nuclei was necessary not only in case of QGSJET model but naturally also for other models used (SIBYLL, VENUS, NEXUS).

The multi-muon events have been analyzed also in other L3+C analysis [96]. It was found that the absolute rate of multi-muon events cannot be explained by CORSIKA/QGSJET. To study well reconstructed low multiplicity events authors of [96] define the event selection criteria:

$$N_\mu(E_\mu \geq 100\ GeV) \geq 5,\ 6 \leq N_\mu \leq 14\ \ . \tag{6.1}$$

The assumed flux was derived from direct measurements of JACEE and RUNJOB. The mixture of primary composition of p, He, *medium mass nuclei* and Fe was simulated with the ratios 2 : 2 : 1 : 1. With these assumptions CORSIKA/QGSJET underestimates production of selected events by at least 50%.

The energy range most relevant to the selection defined in Eq. 6.1 is the interval $10^{14} - 10^{15}\ eV$. Here the expected flux of direct measurements is closer to line *2* than to other two fluxes *1* and *3* in Fig. 5.10. Taking the same flux assumption in our analysis the medium parts of the uncertainty regions in Fig. 6.4 are

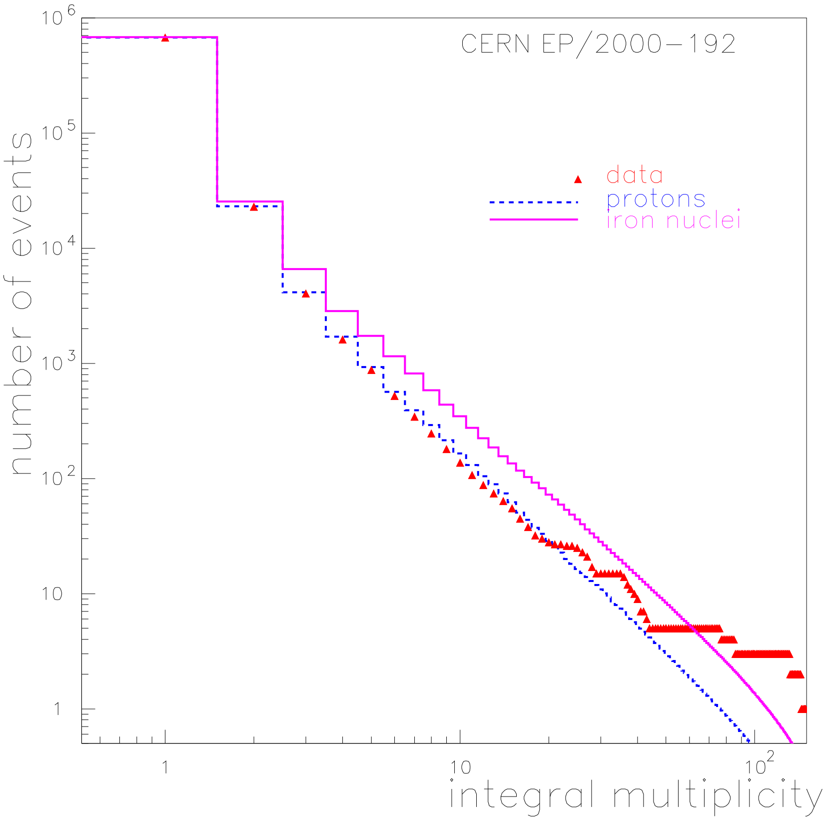

Figure 6.12: The integral multiplicity distribution as measured at ALEPH compared to prediction of QGSJET model [81]. The plot is obtained with agreement of COSMO-ALEPH collaboration from [81] by adding their muon multiplicity distributions for zenith angles $\theta < 30°$ and $30° < \theta < 60°$.

relevant. In this case the disagreement between the data and the predicted event intensities are apparent already at low multiplicities, similarly to the discussed result of L3+C.

It is difficult to make direct comparison of individual analyses of LEP experiments DELPHI, ALEPH and L3+C. The experiments differ by the used measurement technique, by the size of detection area and also by the thickness of overburden (L3 - 30 m, DELPHI - 100 m and ALEPH - 140 m). However, all of them deal with similar problems when comparing the amount of observed multi-muon events with the MC simulations based on CORSIKA/QGSJET. Moreover the choice of the other models (DPMJET, SIBYLL, VENUS) does not improve the consistency. In case of the analysis [96] the data were compatible with the model COMUGEN [97]. However, this model has been developed in particular for purpose of L3+C and it has not been used by any other experiment.

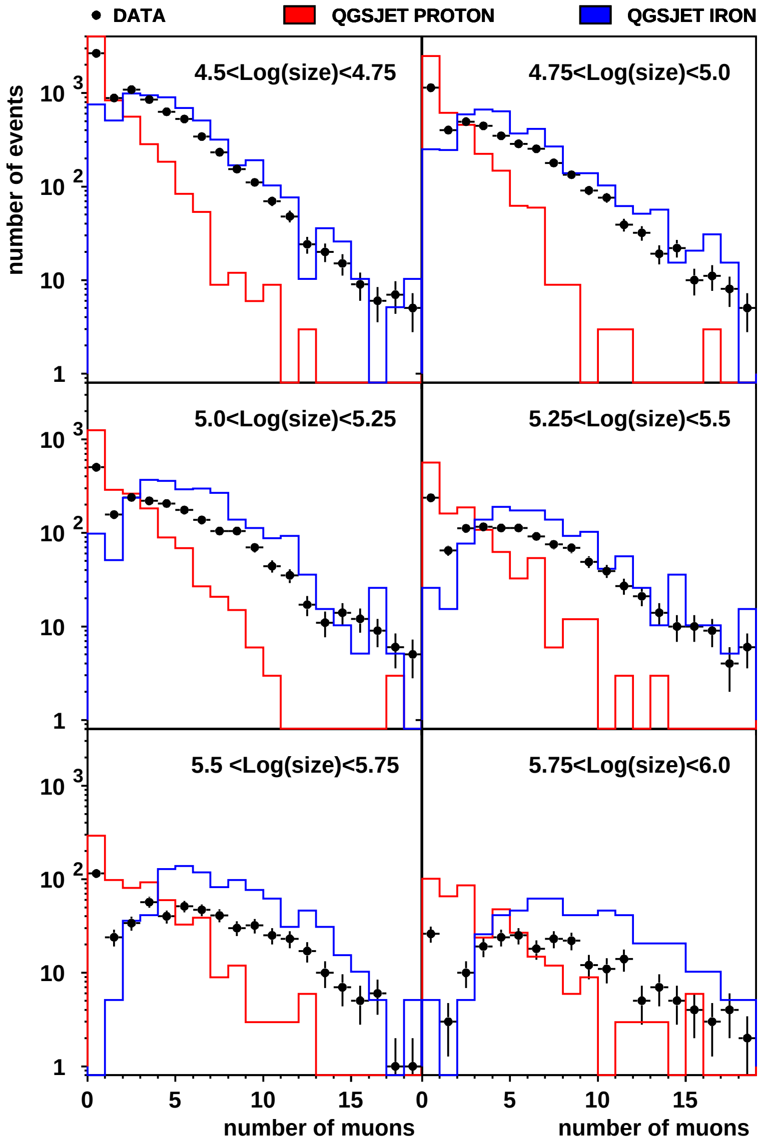

Figure 6.13: L3+C results. The multiplicity distributions in bins of different electromagnetic shower size. Picture is taken from [95], where details of event selection are explained.

6.8 Summary and Discussion

The simulations based on CORSIKA package were performed in order to compare measured and simulated multiplicity distributions. QGSJET [2] was chosen as the input model to describe high energy interactions of hadrons. We have two main motivations for this choice of model. First, it is probably the most common model and second, it is claimed [68] that it describes best various correlations between different shower components.

It was found that the data could be understood only with extremal assumption that above certain multiplicity (energy) most of the primary cosmic particles have to be very heavy. The agreement between Monte Carlo and data depends strongly on the assumed flux. However, even the assumption of high flux (at the very upper limit of measurements) and heavy primary composition hardly describes the upper part of multiplicity spectrum.

The result is more likely connected with inefficiencies of high energy interaction models than with dramatic change of the composition of cosmic rays.

Since other models DPMJET and SIBYLL predict high multiplicity events less frequently when compared to QGSJET, it cannot be expected that the full simulation with these models would give more satisfactory result[2]. We have therefore tested the modification of QGSJET internal parameters (according to [85] with model *3a* from [86]), because it was found that it produces showers with larger muon content [86].

The results with modification *3a* enlarge the region where the data are between the prediction for protons and iron nuclei. The consistency with the data is thus in this case better. At small multiplicities the data prefer lower flux of primary particles compared to the results obtained with QGSJET. More realistic flux *1b* is compatible with direct measurements (JACEE, etc.) and it is sufficient to produce enough low multiplicity events initiated by proton primary particles. At high multiplicities, flux *1b* naturally gives smaller number of events when compared to flux *1*. However, the model *3a* with flux *1b* still produces more high and medium multiplicity events than QGSJET with flux *1*.

The large computing power necessary to simulate atmospheric showers without thinning is the biggest limitation of this work. Because of this reason the full simulation is performed only for two primary particle types and only with two MC schemes. The size of the simulated data samples is of course not ideal, however, it is sufficient to draw the above-mentioned conclusions.

It should be mentioned that the data depend not only on the high energy interaction model, but the low energy model GHEISHA is also of some relevance. Alternative replacements by FLUKA or URQMD were not studied because of

[2] The interaction model NEXUS [98] was not used as an alternative tool, because it requires large computing power

limited computer power. The low energy model of hadron-hadron interactions is used only if the CMS energy available for generation of secondary particles drops below 12 GeV. This value corresponds to laboratory energy of about 80 GeV. Some observed 50 GeV muons could be thus created in decays of mesons produced according to low energy model. However, most of the observed muons originate from mesons created in collisions with energy $10-100$ times larger than the muon energy [99]. In our case the most relevant collisions are those with laboratory energy $500-5000$ GeV, i.e. collisions already described by QGSJET. Consequently the impact of the low energy model on the presented analysis can be neglected.

The work suffers from experimental limitations as well. The size of the detector is rather small and it corresponds to just a fraction of the shower size. Therefore, the only information we measure is in fact the local muon density in particular place of the shower. Much better analysis would be possible with larger detector device. The detector array on the ground would also improve the analysis since it would measure electromagnetic properties of the showers which could be then compared with their muon content (e.g. L3+C results). Although there were some attempts to build experiment with large surface and underground array at CERN [56] the idea was not realized. Another experiment devoted to multi-muons is however under construction in Center for Underground Physics in Pyhälmi mine [100] in Finland.

The estimates of the mass composition of cosmic rays with the energy higher than 10^{14} eV still suffer from many uncertainties. The important source of this uncertainties originates from models describing the high energy interactions of hadrons. Not only results of individual experiments are inconsistent between each other, but also various measurements of one experiment depend on the particular model used.

However, there is a hope that the situation will improve in following years. The accelerator data relevant to cosmic ray physics at the knee energies become available from TEVATRON. In few years even more data will come from the LHC accelerator, where the forward physics (crucial for the cosmic ray experiments) will be studied. In particular TOTEM experiment devoted to measurement of elastic cross-section will provide us some important input. All this information will be used to tune the interaction models. Together with cosmic ray experiments the accelerator measurements will hopefully clarify the uncertainties of the models and consequently the inconsistencies in the mass composition of cosmic rays will be much reduced.

7 Conclusions

The DELPHI detector has been used to study cosmic ray events detected in the apparatus as multi-muon bundles. The main sub-detector used in this analysis was hadron calorimeter with its cathode readout. Additional information was obtained also from time projection chamber, however, only fraction of the events could be analyzed. The important steps towards the detection of multi-muon bundles were *i)* the construction of cathode readout in the hadron calorimeter in $1996 - 1997$ and *ii)* the implementation of DELPHI cosmic trigger in the year 1998. The selected data correspond to $1.6\ 10^6\ s$ of the live time during the years 1999 and 2000.

The muon multiplicity distributions of cosmic ray events were estimated from hadron calorimeter and time projection chamber. The aim of the work was to compare the measured distributions with the predictions of Monte Carlo simulations.

Standard simulation tool CORSIKA [1] with QGSJET [2] model of hadron-hadron collisions was used to simulate cosmic ray showers in the atmosphere. The muon transport through the rock above DELPHI as well as the detector response were simulated in details. Two extremal cases of hadron primary particles were investigated in the work, p and Fe. They represent the lightest (p) and the heaviest (Fe) component of primary cosmic rays. The measured muon multiplicity distribution should be between these two extremal predictions.

The result of simulation necessarily depends on the assumed energy spectrum of primary cosmic rays. Several possible spectra were investigated. Assuming flux *1* (Fig. 5.10 - very upper limit of measurements) the number of observed events is compatible with the proton prediction at low multiplicities $N_\mu^{HCAL} < 6$. Up to the multiplicity ~ 20 the data could be described as a mixture of light (proton) and heavy (iron) component of primary cosmic rays. At medium muon multiplicities the MC simulation with pure iron nuclei as primary particles is needed to obtain number of events comparable with the data. In the region of the highest muon multiplicities the number of events in the data is above both predictions of proton and iron primary particles. It is likely that the problems originate in the interaction model which underestimates production of multi-muons.

It was found that the modification of QGSJET parameters (model *3a* from [86]) improves the consistency of the simulation with the data. This modification decreases the inelastic cross-sections and increases the elasticity of hadron collisions as described in Sec. 6.6. Assuming the same flux (no. *1* in Fig. 5.10) like in the case of QGSJET, the simulation with model *3a* and iron nuclei as primary particles still predicts smaller number of events compared to the data but now only in the region of very high multiplicities and with smaller significance (effect on the level of $\sim 1.7\ \sigma$ at $N_{\mu}^{HCAL} \geq 80$). The number of events at low muon multiplicities in case of proton primaries is now larger than in the data. Smaller and more realistic flux *1b* predicts the number of low multiplicity events consistent with the data. On the other hand, it produces also smaller number of high multiplicity events. Consequently, the significance of the excess of high multiplicity events in the data with respect to the prediction of iron nuclei increases ($\sim 2.0\ \sigma$ at $N_{\mu}^{HCAL} \geq 80$). However, the model *3a* with flux *1b* still produces more events at high and medium multiplicities than QGSJET with flux *1*.

The interpretation of data from cosmic ray experiments has to deal with many uncertainties. In case of fluoresce and Čerenkov technique the most important aspects are the unknown properties of atmosphere and impact of the used hadron interaction model. Surface detectors study only the information in one particular place of the atmospheric shower. Interpretation of their data is completely dependent on the models of the shower propagation, including the modeling of high energy hadron collisions.

The underground experiments detect deeply penetrating muon component. Depending on the underground location, muons created in the upper atmosphere are selected and in fact the properties of several first interactions are studied. Within this context the underground data from medium-depth cosmic ray experiments provide new handle to test the models of high energy hadron interactions.

The aim of this analysis is not to quantify the excess of muons in the data with respect to simulation. It is in fact not possible with the current knowledge of cosmic ray composition and flux. However, the data clearly show that the models underestimate production of high energy muons (at $E_{\mu} > 50\ GeV$) measured in multi-muon bundles. Our measurement shows similar effect as ALEPH or L3+C analyses.

Interpretations of measurements obtained from indirect cosmic ray experiments rely on the underlying models of hadron-hadron interactions. Especially the estimates of cosmic ray composition still suffer from the inconsistencies caused by the models. Improvements in description of hadron-hadron collisions and tunings to new precise measurements of the forward particle production at corresponding energies are needed to improve our understanding of cosmic rays in the knee region and above. In this sense, future experiments at LHC could significantly influence also the cosmic ray physics. However, the accelerator experiments can hardly investigate the very forward region of interactions. From this point of view, the underground experiments can provide complementary data.

Currently there is no large detector device at the medium depth underground dedicated to cosmic rays, which would provide precise measurements. In this sense, results of LEP experiments are very useful, even if these detectors are rather small and they were not originally designed for cosmic ray physics.

A DELPHI reference frame

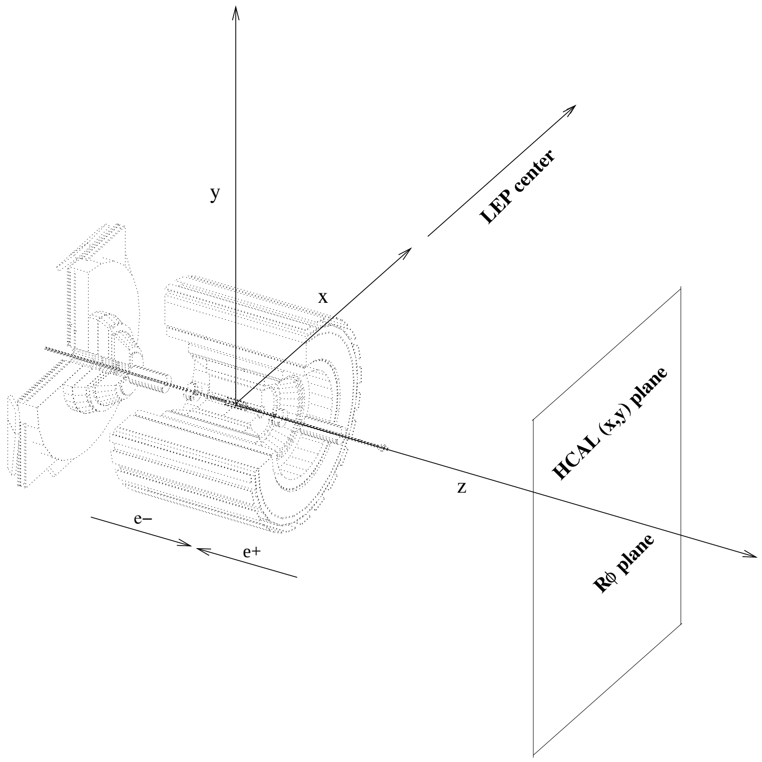

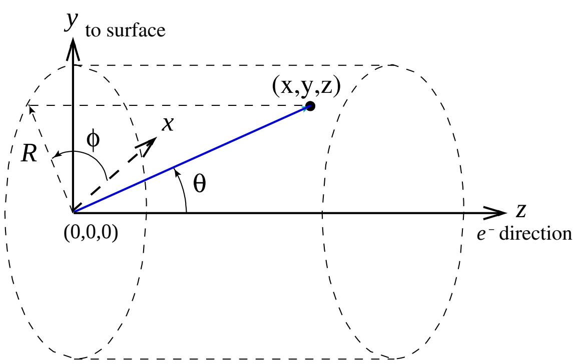

B ECTANA reconstruction probabilities

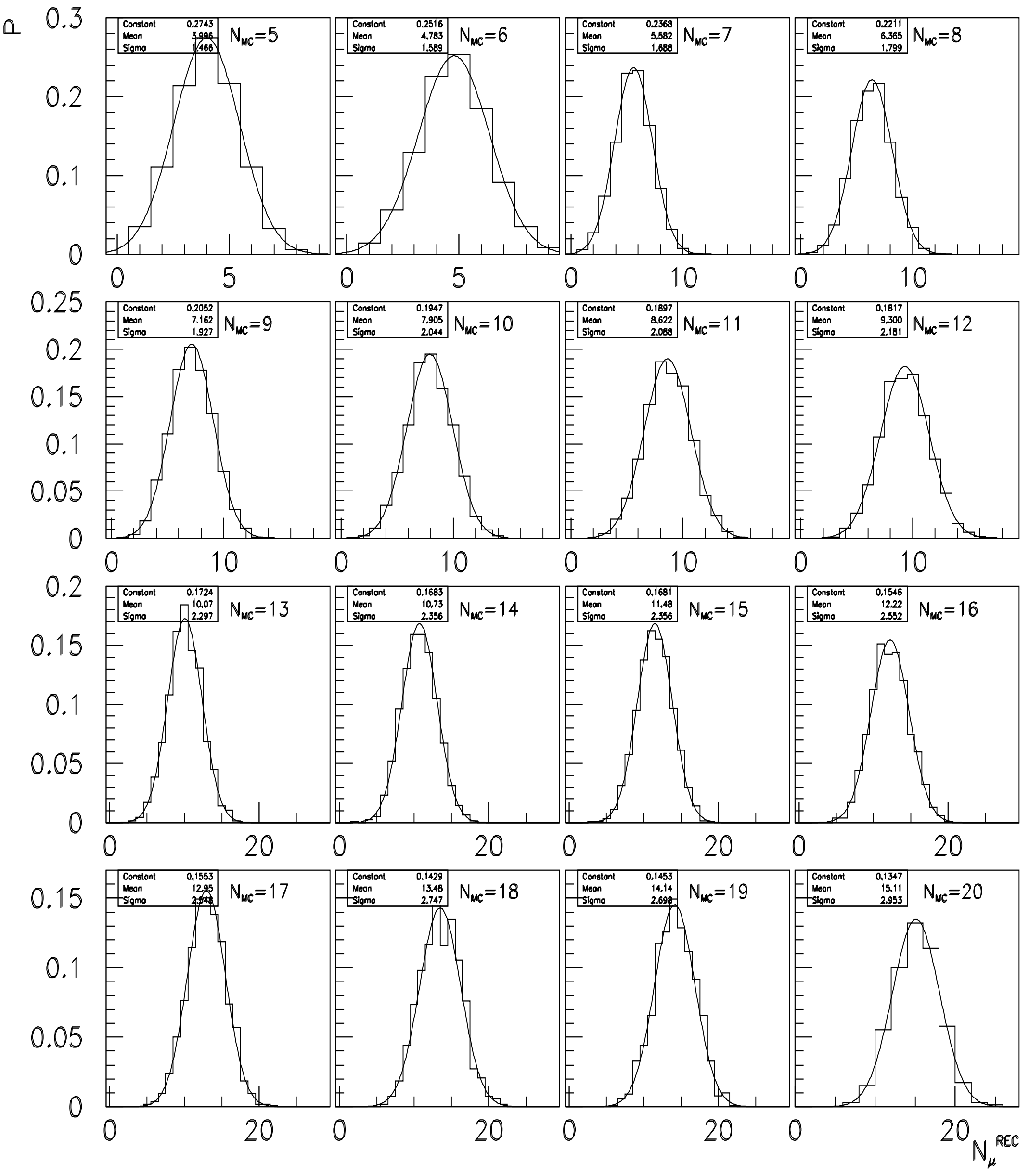

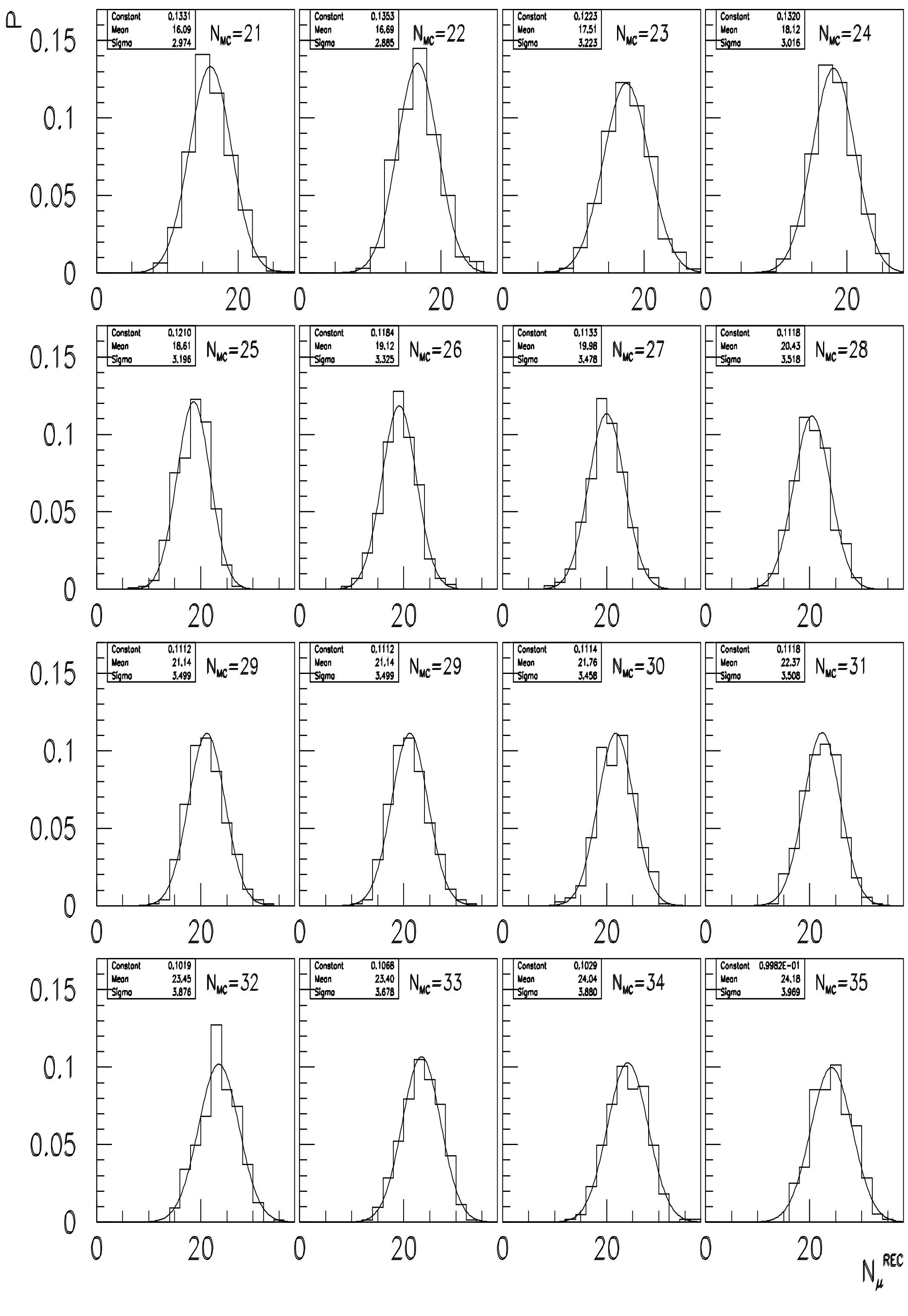
P
Constant 0.1331 Mean 16.09 Sigma 2.974
N_MC=21
Constant 0.1353 Mean 16.69 Sigma 2.885
N_MC=22
Constant 0.1223 Mean 17.51 Sigma 3.223
N_MC=23
Constant 0.1320 Mean 18.12 Sigma 3.016
N_MC=24
Constant 0.1210 Mean 18.61 Sigma 3.196
N_MC=25
Constant 0.1184 Mean 19.12 Sigma 3.325
N_MC=26
Constant 0.1133 Mean 19.98 Sigma 3.478
N_MC=27
Constant 0.1118 Mean 20.43 Sigma 3.518
N_MC=28
Constant 0.1112 Mean 21.14 Sigma 3.499
N_MC=29
Constant 0.1112 Mean 21.14 Sigma 3.499
N_MC=29
Constant 0.1114 Mean 21.76 Sigma 3.458
N_MC=30
Constant 0.1118 Mean 22.37 Sigma 3.508
N_MC=31
Constant 0.1019 Mean 23.45 Sigma 3.876
N_MC=32
Constant 0.1068 Mean 23.40 Sigma 3.678
N_MC=33
Constant 0.1029 Mean 24.04 Sigma 3.880
N_MC=34
Constant 0.9982E-01 Mean 24.18 Sigma 3.969
N_MC=35
N_μ^REC

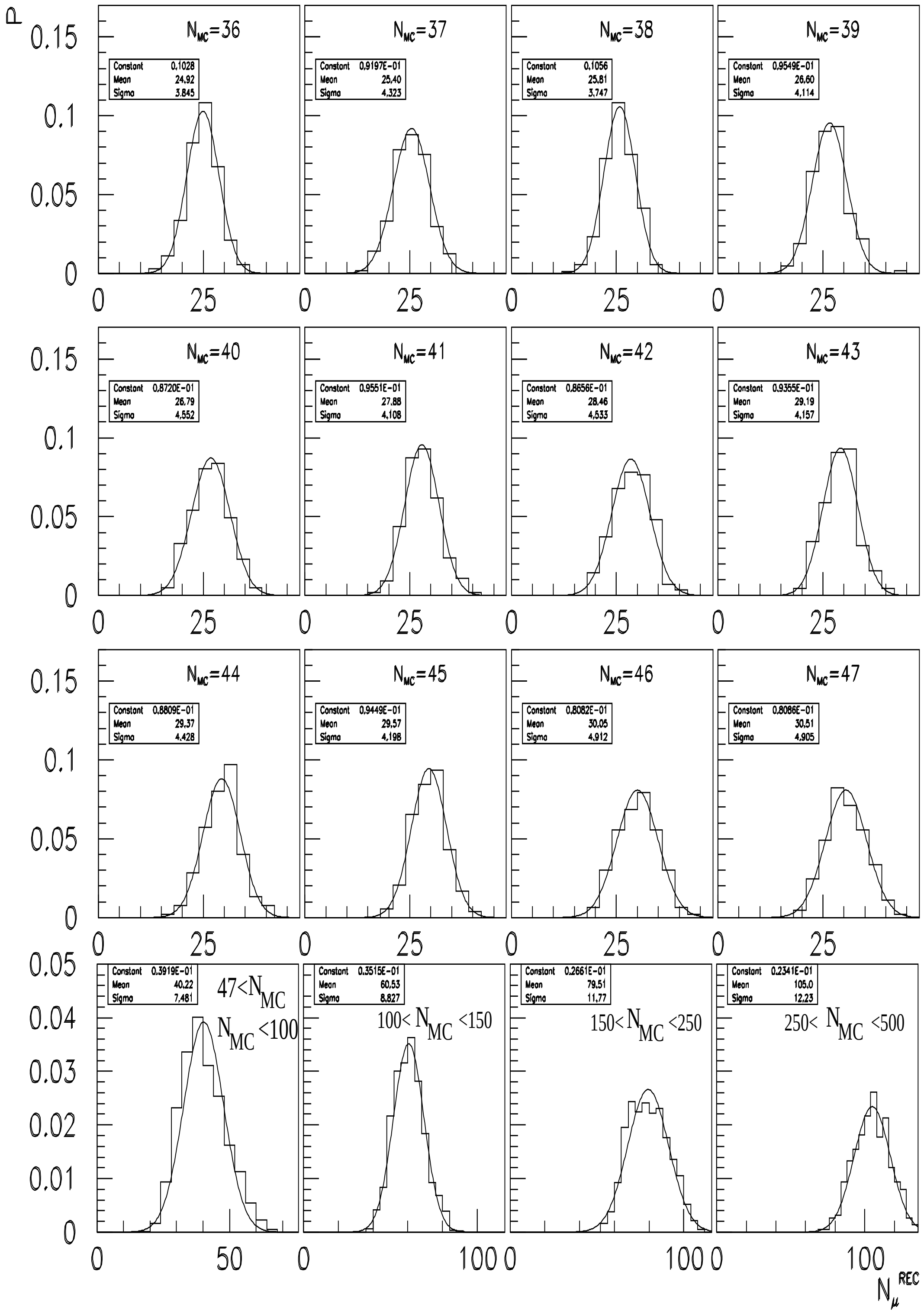
P
N_{MC}=36
Constant 0.1028
Mean 24.92
Sigma 3.845
N_{MC}=37
Constant 0.9197E-01
Mean 25.40
Sigma 4.323
N_{MC}=38
Constant 0.1056
Mean 25.81
Sigma 3.747
N_{MC}=39
Constant 0.9549E-01
Mean 26.60
Sigma 4.114
N_{MC}=40
Constant 0.8720E-01
Mean 26.79
Sigma 4.552
N_{MC}=41
Constant 0.9551E-01
Mean 27.88
Sigma 4.108
N_{MC}=42
Constant 0.8656E-01
Mean 28.46
Sigma 4.533
N_{MC}=43
Constant 0.9355E-01
Mean 29.19
Sigma 4.157
N_{MC}=44
Constant 0.8809E-01
Mean 29.37
Sigma 4.428
N_{MC}=45
Constant 0.9449E-01
Mean 29.57
Sigma 4.198
N_{MC}=46
Constant 0.8082E-01
Mean 30.05
Sigma 4.912
N_{MC}=47
Constant 0.8086E-01
Mean 30.51
Sigma 4.905
Constant 0.3919E-01
Mean 40.22
Sigma 7.481
47<N_{MC}
N_{MC}<100
Constant 0.3515E-01
Mean 60.53
Sigma 8.827
100< N_{MC} <150
Constant 0.2661E-01
Mean 79.51
Sigma 11.77
150< N_{MC} <250
Constant 0.2341E-01
Mean 105.0
Sigma 12.23
250< N_{MC} <500
N_{μ}^{REC}

Bibliography

[1] D. Heck, G. Schatz, T. Thouw, J. Knapp and J. N. Capdevielle, *"CORSIKA: A Monte Carlo code to simulate extensive air showers,"* FZKA-6019 also at
`http://ik1au1.fzk.de/~heck/corsika/physics_description/corsika_phys.html`

[2] N. N. Kalmykov, S. S. Ostapchenko and A. I. Pavlov, *"Quark-Gluon String Model And Eas Simulation Problems At Ultra-High Energies,"* Nucl. Phys. Proc. Suppl. **52B**, 17 (1997).

N. N. Kalmykov and S. S. Ostapchenko, *"The Nucleus-Nucleus Interaction, Nuclear Fragmentation, And Fluctuations Of Extensive Air Showers,"* Phys. Atom. Nucl. **56**, 346 (1993) [Yad. Fiz. **56N3**, 105 (1993)].

[3] J. Ridky, P. Travnicek (DELPHI Collaboration), Nucl. Phys. Proc. Suppl. **122**, 285 (2003)

[4] J. Ridky, P. Travnicek, DELPHI-NOTE: 2002-075 CONF 609, accepted contribution of ICHEP 2002, presented by Charles Timmermans from L3+C

[5] J. Ridky, P. Travnicek (DELPHI Collaboration), *"Cosmic Multi-Muon Bundles Detected By Delphi,"* Acta Physica Polonica B **35**, No. 6, 1813, (2004)

[6] C. T. R. Wilson, Camb. Phys. Soc. Proc. 11, 32, (1901)

[7] V. F. Hess, *"Über Beobachtungen der durchdringenden Strahlung bei sieben Freiballonfahrten"* Phys. Z. **13**, 1084, (1912)

[8] W. Kolhörter : Phys. Z., **14**, 1153, (1913)

[9] Bohacova, M.: personal discussions

[10] J. Clay: Proc. Ned. Akad. v. Wet. **30**, 1115 (1927)
A. H. Compton: Phys. Rev. **43**, 387, (1933)
T. H. Jonson: Phys. Rev. **45**, 569, (1934)

[11] C. D. Anderson, *"The Positive Electron,"* Phys. Rev. **43**, 491 (1933).

[12] K. Schmeiser and W. Boethe, : Ann. Phys. **32**, 161, (1938)

[13] W. Kolhörster *et al.*: Naturwiss. **26**, 576, (1938)

[14] P. Auger, R. Maze and T. Grivet-Mayer, *"Extensive Cosmic Showers In The Atmosphere Containing Ultra–Penetrating Particles,"* Compt. Rend. Acad. Sci. (Ser. II) **206**, 1721 (1938).

[15] R. Cahn, G. Goldhaber, *"Experimental foundation of particle physics"*, Cambridge University Press, Cambridge 1989

[16] J. J. Aubert *et al.* (S. C.C. Ting), *"Experimental Observation Of A Heavy Particle J,"* Phys. Rev. Lett. **33**, 1404 (1974).

[17] J. E. Augustin *et al.* (B. Richter), *"Discovery Of A Narrow Resonance In E+ E- Annihilation,"* Phys. Rev. Lett. **33**, 1406 (1974).

[18] S. W. Herb *et al.* (L. M. Lederman), *"Observation Of A Dimuon Resonance At 9.5-Gev In 400-Gev Proton - Nucleus Collisions,"* Phys. Rev. Lett. **39**, 252 (1977).

[19] F. Abe *et al.* [CDF Collaboration], *"Observation of top quark production in anti-p p collisions,"* Phys. Rev. Lett. **74**, 2626 (1995) [arXiv:hep-ex/9503002].

[20] S. Abachi *et al.* [D0 Collaboration], *"Observation of the top quark,"* Phys. Rev. Lett. **74**, 2632 (1995) [arXiv:hep-ex/9503003].

[21] M. L. Perl *et al.*, *"Evidence For Anomalous Lepton Production In E+ E- Annihilation,"* Phys. Rev. Lett. **35**, 1489 (1975).

[22] K. Kodama *et al.* [DONUT Collaboration], *"Observation of tau-neutrino interactions,"* Phys. Lett. B **504**, 218 (2001) [arXiv:hep-ex/0012035].

[23] R. J. Davis, D. S. Harmer and K. C. Hoffman, *"Search For Neutrinos From The Sun,"* Phys. Rev. Lett. **20**, 1205 (1968).

[24] Q. R. Ahmad *et al.* [SNO Collaboration]: *"Direct evidence for neutrino flavor transformation from neutral-current interactions in the Sudbury Neutrino Observatory,"* Phys. Rev. Lett. **89**, 011301, (2002)

[25] Y. Fukuda *et al.* [Super-Kamiokande Collaboration]: *"Measurement of the flux and zenith-angle distribution of upward through-going muons by Super-Kamiokande,"* Phys. Rev. Lett. **82**, 2644, (1999)

[26] E. Andres *et al.*: *"The AMANDA neutrino telescope: Principle of operation and first results,"* Astropart. Phys. **13**, 1, (2000)

[27] G. D. Hallewell [ANTARES Collaboration]: *"Status Of The Antares Underwater Neutrino Telescope,"* Nucl. Instrum. Meth. A **502**, 13, (2003)

[28] Tzamarias S.E. : S. E. Tzamarias [NESTOR Collaboration], *"Nestor: A Deep-Sea Neutrino Telescope,"* Nucl. Instrum. Meth. A **502** (2003) 150.

[29] B. Wiebel-Sooth: *"Measurement of all particle energy spectrum and chemical composition of COSMIC rays at HEGRA detector"* WUB-DIS-98-9 (1998)

[30] K. Hagiwara *et al.* [Particle Data Group Collaboration], *"Review Of Particle Physics,"* Phys. Rev. D **66**, 010001 (2002).

[31] K. Asakimori et al.: Proc. 23rd Int. Cosmic Ray Conf., Calgary, 2, 25, (1993); Proc. 22nd Int. Cosmic Ray Conf., Dublin, 2, 57 and 97 (1991).

[32] N. L. Grigorov, V. E. Nesterov, I. D. Rapoport, I. A. Savenko and G. A. Skuridin, *"Investigation Of Energy Spectrum Of Primary Cosmic Particles With High And Superhigh Energies Of Space Stations *Proton*,"* Yad. Fiz. **11** (1970) 1058.
and Proc. 12th Int. Cosmic Ray Conf., Hobart, 2, 206, (1971).

[33] T.V. Danilova et al.: Proc. 15th Int. Cosmic Ray Conf., Plovdiv, 8, 129 (1977).

[34] Yu. A. Fomin et al.: Proc. 22nd Int. Cosmic Ray Conf., Dublin, 2, 85 (1991).

[35] M. Amenomori *et al.* [Tibet AS gamma Collaboration], *"The Cosmic ray energy spectrum between 10**14.5-eV and 10**16.3-eV covering the 'knee' region,"* Astrophys. J. **461**, 408 (1995).

[36] M. Nagano *et al.*, *"Energy Spectrum Of Primary Cosmic Rays Between 10**14.5-Ev And 10**18-Ev,"* J. Phys. G **10**, 1295 (1984).

[37] F. Arqueros *et al.* [HEGRA Collaboration], *"Energy spectrum and chemical composition of cosmic rays between 0.3-PeV and 10-PeV determined from the Cherenkov-light and charged-particle distributions in air showers,"* Astron. Astrophys. **359** (2000) 682 [arXiv:astro-ph/9908202].

[38] M. A. K. Glasmacher *et al.*, *"The Cosmic Ray Energy Spectrum Between 10**14-Ev And 10**16-Ev,"* Astropart. Phys. **10**, 291 (1999).

[39] D. J. Bird *et al.* [HIRES Collaboration], *"The Cosmic Ray Energy Spectrum Observed By The Fly's Eye,"* Astrophys. J. **424**, 491 (1994).

[40] M. Takeda *et al.*, *"Extension of the cosmic-ray energy spectrum beyond the predicted Greisen-Zatsepin-Kuzmin cutoff,"* Phys. Rev. Lett. **81**, 1163 (1998) [arXiv:astro-ph/9807193].

[41] T. K. Geisser: *"Cosmic rays and particle physics,"* Cambridge press, (1990)

[42] V. S. Ptuskin *et al.*: Aston. Astroph. **321**, 434, (1997)

[43] K. Kobayakawa, Y. Sato and T. Samura, *"Acceleration of particles by oblique shocks and cosmic ray spectra around the knee region,"* Phys. Rev. D **66**, 083004 (2002) [arXiv:astro-ph/0008209].

[44] A. D. Erlykin, M. Lipski and A. W. Wolfendale, Astropart. Phys. **8**, 283 (1998).

[45] J. R. Hörandel, *"On the Knee in the Energy Spectrum of Cosmic Rays"*, 27th Internat.Cosmic Ray Conf., Hamburg, August 7-15, 2001 ; ICRC 2001 Katlenburg-Lindau : Copernicus Ges., 2001 **Vol.1** S.71-74

[46] S. P. Swordy *et al.*, *"The composition of cosmic rays at the knee,"* Astropart. Phys. **18**, 129 (2002) [arXiv:astro-ph/0202159].

[47] K. Greisen, Phys. Rev. Lett. **16**, 748 (1966).

[48] V. A. Kuzmin, G. T. Zatsepin: JETP Lett. **4**, 78-80, (1966); Pisma Zh. Eksp. Teor. Fiz. **4**, 114-117, (1966)

[49] J. W. Cronin, *"The highest-energy cosmic rays,"* arXiv:astro-ph/0402487.

[50] E. Fermi: *"On The Origin Of The Cosmic Radiation,"* Phys. Rev. **75**, 1169, (1949).

[51] K. T. Gaisser: *"Cosmic Rays and Particle Physics, Cambridge University Press"*, (1990), ISBN - 0 521 32667 2, page 153

[52] A. R. Bell, *"The Acceleration Of Cosmic Rays In Shock Fronts. I,"* Mon. Not. Roy. Astron. Soc. **182**, 147 (1978).

[53] A. M. Hillas, Ann. Rev. Astron. Astrophys. **22**, 425 (1984).

[54] P. Bhattacharjee and G. Sigl, *"Origin and propagation of extremely high energy cosmic rays,"* Phys. Rept. **327**, 109 (2000) [arXiv:astro-ph/9811011].

[55] K. Greisen, Ann.Rev. of Nuclear Science, 10, 63, (1960)

[56] V. Avati *et al.*, *"CORAL : A cosmic ray experiment in and above the LHC tunnel,"* CERN-SPSC-2001-003 ; SPSC-P-321. - Geneva : CERN , 8 Jan 2001.

[57] H. Adarkar *et al.*, *"A Multi - Tev Muon Bundle Observed In The Kgf Underground Detector,"* Phys. Lett. B **267**, 138 (1991).

[58] KASCADE proposal available at `http://www-ik.fzk.de/publication/Kascade-proposal.ps.gz`

[59] H. Bozdog *et al.*, Nucl. Instrum. Meth. A **465**, 455 (2001).

[60] J. Engler *et al.*, Nucl. Instrum. Meth. A **427**, 528 (1999).

[61] K. Werner, *"Strings, pomerons, and the venus model of hadronic interactions at ultrarelativistic energies,"* Phys. Rept. **232**, 87 (1993).

[62] J. Ranft, Phys. Rev. D **51**, 64 (1995).

[63] R. S. Fletcher, T. K. Gaisser, P. Lipari and T. Stanev, Phys. Rev. D **50**, 5710 (1994).

[64] J. Engel, T. K. Gaisser, T. Stanev and P. Lipari, Phys. Rev. D **46**, 5013 (1992).

[65] J. N. Capdevielle, *"A Monte Carlo Generator For Cosmic Ray Collisions,"* J. Phys. G **15**, 909 (1989).

[66] H. Fesefeldt: Report **PITHA-85/02**, RWTH Achen, (1985)

[67] T. Sjostrand, *"The Lund Monte Carlo For Jet Fragmentation And E+ E- Physics: Jetset Version 6.2,"* Comput. Phys. Commun. **39**, 347 (1986).

[68] T. Antoni *et al.* [KASCADE Collaboration], *"Test of high-energy interaction models using the hadronic core of EAS,"* J. Phys. G **25**, 2161 (1999) [arXiv:astro-ph/9904287].

[69] J. Knapp, D. Heck, G. Schatz: FZKA report 5828; also at `http://ik1au1.fzk.de/~heck/corsika/modelcomp/modelcomp.html`

[70] R. J. Glauber and G. Matthiae, *"High-Energy Scattering Of Protons By Nuclei,"* Nucl. Phys. B **21**, 135 (1970).

[71] W. R. Nelson, H.Hirayama, D. W. O. Rogers: Report SLAC **265** (1985)

[72] K. Greisen: Prog. cosmic ray Physics Vol **III**, J.G. Wilson ed. (North Holland Publishing co. Amsterdam) (1965)

[73] R. Brun, *et al.*: GEANT3, *Report CERN DD/EE/84-1* (1987), CERN, Geneva

[74] Heck, D., Knapp J.: CORSIKA reference manual at `http://ik1au1.fzk.de/~heck/corsika/usersguide/corsika_tech.html`

[75] J. Ridky, V. Vrba, J. Chudoba, Delphi note 99-181 TRACK 96 (1987)

[76] P. Abreu *et al.* [DELPHI Collaboration], *"Performance of the DELPHI detector,"* Nucl. Instrum. Meth. A **378**, 57 (1996).

[77] P. A. Aarnio *et al.* [DELPHI Collaboration], *"The Delphi Detector At Lep,"* Nucl. Instrum. Meth. A **303**, 233 (1991).

[78] A. Augustinus *et al.* [DELPHI Trigger Group Collaboration], *"The DELPHI trigger system at LEP2 energies,"* Nucl. Instrum. Meth. A **515**, 782 (2003).

[79] DELANA team: DELHI NOTE 9-44 PROG 137

[80] DELPHI Collaboration, *"DELSIM, Delphi Event Generation and Detector Simulation User's guide"* (DELPHI NOTE: 89-67 PROG 142)

[81] V. Avati *et al.*, *"Cosmic multi-muon events observed in the underground CERN-LEP tunnel with the ALEPH experiment,"* Astropart. Phys. **19**, 513 (2003).

[82] D. Heck, *et al.*, Proceedings of ICRC 2001, p. 522

[83] CORSIKA reference manual, page 35.
`http://ik1au1.fzk.de/~heck/corsika/usersguide/corsika_tech.html`

[84] M.A.Lawrence, J. Phys. G.: Nucl Part. Phys. **17**, 733-757, (1991)

[85] discussions with Dr. Ralph Engel, and Dr. Jörg Hörandel

[86] J. R. Hörandel, *"On total inelastic cross-sections and the average depth of the maximum of extensive air showers,"* J. Phys. G **29**, 2439 (2003) [arXiv:astro-ph/0309010].

[87] J. R. Hörandel, *"On the knee in the energy spectrum of cosmic rays,"* Astropart. Phys. **19**, 193 (2003) [arXiv:astro-ph/0210453].

[88] F. Abe *et al*, Phys. Rev. D **50**, 5518, (1994)

[89] N.A. Amos *et al*, Phys. Rev. Lett. B **68**, 2433, (1992)

[90] C. Avilla *et al*, Phys. Lett. B **445**, 419, (1999)

[91] F. Abe *et al*, Phys. Rev. D **50**, 5550, (1994)

[92] N. A. Amos *et al*, Phys. Lett. B **243**, 158, (1990)

[93] M. Unger: *"Measurement of the atmospheric muon spectrum from 20 to 2000 GeV,"* XXVIII International Cosmic Ray Conference (ICRC), Tsukuba, Japan, 2003 (proceed ings) (295)

[94] H. G. S. Wilkens [L3 Collaboration], *"Electron And Muon Densities In Cosmic Rays Measured At L3+C,"* Nucl. Phys. Proc. Suppl. **122**, 297, (2003)

[95] H. G. S. Wilkens, *"Experimental study of high energy muons from extensive air showers in the energy range 100 TeV to 10 PeV"*, University of Nijmegen, 2003, PhD. thesis

[96] Q. Zhu, *"Nature of 100 TeV Hadronic Interactions in the Forward Region Seen from Muon Data of the L3+C Experiment"* XXVIII International Cosmic Ray Conference (ICRC), Tsukuba, Japan, 2003 (proceedings) p. 295

[97] Q. Zhu *et al*, J. Phys. G **20**, 1383, (1994)

[98] H. J. Drescher *et al.*, Phys. Rep. 350, 93, (2001).

[99] R. Engel, *"Extensive air showers and accelerator data: The NEEDS workshop,"* Nucl. Phys. Proc. Suppl. **122**, 437 (2003) [arXiv:hep-ph/0212340].

[100] T. Enqvist *et al.*, XXVIII International Cosmic Ray Conference (ICRC), Tsukuba, Japan, 2003 (proceedings) (997-1000)